UC Berkeley

UC Berkeley Electronic Theses and Dissertations

Title
ZnO Nanostructure Synthesis & Laser Direct Writing Process for Optoelectronic Devices

Permalink
https://escholarship.org/uc/item/5hr8c1jm

Author
LEE, DAEHO

Publication Date
2012

Peer reviewed|Thesis/dissertation

eScholarship.org Powered by the California Digital Library
University of California

ZnO Nanostructure Synthesis & Laser Direct Writing Process for Optoelectronic Devices

by

Daeho Lee

A dissertation submitted in partial satisfaction of the
requirements for the degree of
Doctor of Philosophy
in
Engineering – Mechanical Engineering
in the
Graduate Division
of the
University of California, Berkeley

Committee in charge:

Professor Costas P. Grigoropoulos, Chair
Professor Van P. Carey
Professor Nathan W. Cheung

Fall 2012

ZnO Nanostructure Synthesis & Laser Direct Writing Process for Optoelectronic Devices

Copyright © 2012

By

Daeho Lee

Abstract

ZnO Nanostructure Synthesis & Laser Direct Writing Process for Optoelectronic Devices

by

Daeho Lee

Doctor of Philosophy in Engineering - Mechanical Engineering

University of California, Berkeley

Professor Costas P. Grigoropoulos, Chair

Zinc oxide (ZnO) has a long history of usage in electronics. Recently, ZnO has been gathering great interest of researchers in nanoscience due to its diverse and versatile morphologies such as nanoparticles (NP), nanowires (NW), nanorods, nanotubes, nanohelixes, etc. This dissertation deals with studies covering from the synthesis of ZnO nanostructures to deposition & patterning methods and their applications for optoelectronic devices such as transparent electrodes, active layers for thin film transistor and photovoltaics.

A very well-dispersed, transparent and concentration-tunable ZnO NP solution was successfully synthesized with a new process. Highly transparent ZnO thin films were fabricated by spin coating and subsequent ultra short-pulsed UV laser annealing was performed to change the film properties. While as-deposited NP thin films were not electrically conductive, laser annealing imparted a substantial conductivity increase. Thus, selective annealing for conductive patterns directly on the NP thin film without a photolithographic process was achieved. The conductivity is by a factor of 10^5 higher than that of the previously reported furnace-annealed ZnO NP films and even comparable to that of vacuum-deposited, impurity-doped ZnO films within a factor of 10. The ZnO film obtained from the process developed in this work has been applied to the fabrication of a thin film transistor (TFT) showing enhanced performance compared with the TFT fabricated on furnace annealed ZnO film. The ZnO TFT performance test reveals that by just changing the laser annealing parameters the solution-deposited ZnO thin film properties can be tuned suitable for both transparent conductors and semiconductor active layers.

Two kinds of nanomaterial patterning methods *via* direct writing have been demonstrated. First, laser-assisted nanoimprinting of metal and semiconductor nanoparticles has been presented as a large area one step patterning method. With the method, submicron structures including mesh, line, nanopillar and nanowire arrays were fabricated on various kinds of wafer scale substrates. Using the rapid laser-based nanolithography, the prohibitive constraints of e-beam patterning could be overcome. Therefore, this method opens a way to the fabrication of electronic and energy devices

with high throughput and ultra low-cost. Second, a drop on demand (DOD) inkjet printing of ZnO seed layers integrated with a CAD (computer aided design) system for a fully digital selective ZnO NW array growth has been discussed. Through proper natural convection suppression during the hydrothermal growth, successful ZnO nanowire local growth could be achieved. Without any need for the photolithographic process or stamp preparation, the NW growth location can be easily modified with high degree of freedom. These two methods are compatible with flexible plastic substrates.

As an application of ZnO nanostructures for high efficiency solar cells, ZnO dye-sensitized solar cells (DSSCs) with greatly enhanced surface area for higher dye loading and light harvesting were demonstrated. The selective growth of "*nanoforests*" composed of high density, long branched tree-like multi generation hierarchical ZnO nanowire photoanodes by utilizing seed particles and a capping polymer increased the energy conversion efficiency significantly. The overall light-conversion efficiency of the branched ZnO nanowire DSSCs was almost 5 times higher than the efficiency of DSSCs constructed by upstanding ZnO nanowires. A parametric study to determine the optimum hierarchical ZnO nanowire photoanode was performed through the combination of both length-wise and branched growth processes.

To Keun-Ah, Chaewon and my parents

ACKNOWLEDGEMENT

I am deeply indebted to many people without whom I would never have finished the arduous four-year marathon race. First of all, I should express my sincere gratitude to my research advisor, Professor Costas P. Grigoropoulos in the Department of Mechanical Engineering at UC Berkeley, for his stimulating and encouraging advice, guidance and financial supports. His perpetual enthusiasm for the research was, is and will be a guiding star for me. I also would like to express my gratitude to Professor Nathan Cheung in the Department of Electrical Engineering & Computer Sciences at UC Berkeley, Professor Van P Carey, Professor Liwei Lin and Samuel S. Mao in the Department of Mechanical Engineering at UC Berkeley for valuable advice and being my qualifying exam committee in their busy schedule. I would also like to thank to Professor Alberto Salleo in the Department of Materials Science and Engineering at Stanford University and Dr. Biwu Ma in the Molecular Foundry at the Lawrence Berkeley National Laboratory for the co-work and valuable discussion.

No one runs alone on the journey of a long marathon race. I would like to acknowledge the help of my colleagues and former students in laser thermal lab. Professor Seung Hwan Ko at KAIST, Daejeon Korea deserves my best gratitude for being my first teacher and a coworker at Berkeley. We were the last men left in the Etcheverry Hall for an uncountable number of days. I also express my special thanks to Dr. Heng Pan at Applied Materials and Professor Ming-Tsang Lee at NCHU, Taichung Taiwan for being my second teachers and coworkers. The lights of the room 5144 and 5115 in the Etcheverry Hall were never turned off. I also would like to thank to Dr. Moosung Kim, Dr. Nipun Misra, Professor David J. Hwang at SUNY at Stony Brook, Dr. Hojeong Jeon, Dr. Sang-gil Ryu, Dr. Jungbin In, Dr. Travis Owens, Professor Nico Hotz at Duke University, Kyunghoon Kim, Sanghoon Ahn, Eunpa Kim, Jae Hyuck Yoo, Alex Sherry, Hyuk-Jun Kwon, Sangmo Koo, Andy Cheng Zheng, Yoonsoo Rho, Dr. Jongbok Park, Dr. Ioanna Sakellari , Carmen Kullmann, Thomas Plattner for the useful discussion, co-work and assistance. Their hard work was always stimulating, encouraging me and kept me awake. I would also extend my gratitude to Dr. Waqas Mustafeez, a member of Professor Salleo's group.

My family has been always with me when I was out of breath facing the humps during the race. I should be extremely grateful to my lovely wife, Keun-Ah Jeon, and adorable daughter, Chaewon Lee for her understanding and patience. I would also like to apologize to them for lonely days in UC Village. My parents always give me unconditional supports, love and understanding. Without my family, nothing would have been possible.

TABLE OF CONTENTS

DEDICATION i

ACKNOWLEDGEMENT ii

TABLE OF CONTENTS iii

LIST OF FIGURES vi

LIST OF TABLES x

NOMENCLATURE xi

Chapter 1 Introduction 1

1.1 ZnO – a versatile material for various optoelectronic device applications in the field of nanoscience 1

1.2 Direct writing technologies 3

1.3 Scope of the dissertation 4

Chapter 2 Synthesis of ZnO nanostructures 6

2.1 Synthesis of ZnO NPs 6
2.1.1 Ethanol-based method 7
2.1.2 Methanol-based method 7

2.2 Synthesis of transparent ZnO NP solution 8

2.3 Characterization of the ZnO NP solution and thin film 10

2.4 Synthesis of ZnO NWs 14

Chapter 3 Conductive transparent ZnO patterning by ultra-short pulsed laser annealing of solution-deposited NPs 19

3.1 Introduction 19

3.2 ZnO thin films prepared by NP solution spin coating 21

3.3 Experimental setup 21

3.4 Laser annealing ... 22

3.5 Device fabrication and testing ... 31

3.6 Conclusion ... 35

Chapter 4 Large area nanoimprinting of NPs enabled by high speed laser direct writing ... 37

4.1 Introduction ... 37

4.2 Experimental setup ... 39
4.2.1 Fine alignment procedures for large area LDW ... 42
4.2.2 Laser beam characterization ... 43

4.3 LDW of SU-8 photoresist to generate positive line patterns ... 45

4.4 LDW of OiR 700-10 phororesist to generate positive dot patterns ... 52

4.5 Characteristics of UV ps laser as a photolithography light source ... 56

4.6 Limitations and solutions ... 57

4.7 Conclusion ... 61

Chapter 5 Digital selective growth of ZnO NW arrays from NP seeds patterned by drop-on-demand inkjet printing on a flexible substrate ... 62

5.1 Introduction ... 62

5.2 Experimental setup ... 63
5.2.1 ZnO NP seed synthesis ... 64
5.2.2 ZnO NP seed inkjet printing ... 64
5.2.3 ZnO NW selective growth with natural convection suppression ... 67

5.3 Characterizations ... 68

5.4 Conclusion ... 74

Chapter 6 Nanoforest composed of hydrothermally grown hierarchical ZnO NWs for a high efficiency dye-sensitized solar cell ... 75

6.1 Introduction ... 75

6.2 Synthesis of ZnO nanoforest ... 77

6.3 DSSC performance ... 82

6.4 Conclusion 85

Chapter 7 Conclusions of the present work 86

Chapter 8 Recommendation for future study 88

References 90

LIST OF FIGURES

Figure 2.1 (a) Milky ZnO solution after reaction; (b) precipitation of the ZnO NPs 8
Figure 2.2 Spin-coated ZnO NP film on a glass substrate with the ZnO-methanol solution 8
Figure 2.3 (a) ZnO NP solutions (solvent: 1-pentanol) with two different concentrations; (b) images of a spin-coated ZnO thin film (thickness: 170 nm) with the solution (a) on a glass substrate; (c) fluorescence of the ZnO solution under UV illumination (365 nm)........ 10
Figure 2.4 ZnO NPs dissolved in various solvents 10
Figure 2.5 (a) TEM image shows the ZnO NP is 6 nm in diameter; (b) XRD pattern of the ZnO NPs shows crystallized wurtzite structure 11
Figure 2.6 Optical transmission measurement of the ZnO solution shows very strong absorption at around 355 nm wavelength; 12
Figure 2.7 XPS spectra of the as-spin-coated ZnO NP thin film. Only XPS and Auger peaks of Zn and O were detected. 13
Figure 2.8 SEM image of the as-spin-coated ZnO NP thin film on a quartz substrate.... 13
Figure 2.9 ZnO NWs grown on FTO glass substrates (a) without a NP seed layer; (b) with a NP seed layer 16
Figure 2.10 ZnO NWs grown on silicon substrates coated with (a) a ZnO NP seed layer (inset: side view); (b) a thin film by DEA-based sol-gel method; (c) a thin film by MEA-based sol-gel method 17
Figure 2.11 ZnO NWs grown on silicon substrates in the precursor solution (a) with PEI (3 mM); (b) without PEI 18
Figure 3.1 Schematic illustration of the picosecond laser annealing setup 22
Figure 3.2 Photoimage of the ZnO thin film on a quartz substrate after laser annealing. Huge reduction of sheet resistance at annealed part is observed. Surface morphology change of the ZnO thin film after laser annealing is also observed. 23
Figure 3.3 SEM image at the boundary of the laser-annealed surface on a quartz substrate 24
Figure 3.4 Comparison of AFM images of (a) as-coated and (b) laser-annealed surfaces. RMS roughness of 1.7 nm after laser annealing 26
Figure 3.5 (a) Sheet resistance (R_s) of the laser annealed ZnO thin film corresponding to laser power; (b) SEM image of the degraded ZnO film on a quartz substrate due to excessive laser power 27
Figure 3.6 (a) Quartz enclosure for argon-air mixture flow; (b) R_s corresponding to the background gas 28
Figure 3.7 (a) Optical transmittance of the ZnO thin films annealed in various background gas compositions; (b) restored transparency of the re-annealed area in the air (A) from an annealed film on a quartz substrate in the argon environment (B). 29
Figure 3.8 LDW of the ZnO thin film on a soda-lime glass. (a) Photograph of arbitrary patterns on the 3 cm by 3 cm area; (b) optical microscope image of 1.5 μm line-width patterns. 30
Figure 3.9 (a) The schematic cross-sectional view of the ZnO thin-film field-effect transistor (ZnO TFT). Cr-Au electrodes were defined by a standard lift-off process

on a highly doped n-type silicon wafer with oxide as gate dielectric. ZnO NPs were spin coated on top; (b), (c) top-view SEM images of the ZnO TFT electrodes without and with a ZnO active layer respectively. ‘S’ and ‘D’ indicates source and drain electrodes respectively. Channel width (*W*) / channel length (*L*) is 160 μm / 12 μm. 32
Figure 3.10 (a) Plot of drain source-current (I_{ds}) versus source-drain voltage (V_{ds}) as a function of gate voltage (V_g); (b) Log-linear (with the left y-axis) and linear-linear (with the right y-axis) plot of I_{ds} versus V_g. * The blue cross-marked line indicates I_d-V_g plot of a thermally annealed TFT at 300 °C for 1.5 h........ 34
Figure 4.1 (a) Schematic illustration of the laser assisted nanoparticle nanoimprinting lithography process; (b) schematic diagram of the experiment setup........ 41
Figure 4.2 Fine alignment procedures for the laser direct writing setup. (a) The beam path, before installing the objective lens, should be vertical to the x-y stage; (b) the objective lens is installed in order that the beam path is not interrupted; (c) a z-axis stage and a tilt stage is installed; (d) the z-axis stage and the tilt stage maintain the focal plane on various thickness substrates. 43
Figure 4.3 Measured intensity at the focal plane 44
Figure 4.4 Fitted Gaussian beam profile at the focal plane 44
Figure 4.5 Gaussian beam width as a function of the axial distance 45
Figure 4.6 (a) Line width of a SU-8 photoresist after developing according to the laser power change. Insets shows bent (left) and stripped (right) SU-8 photoresists when exposure energy is not sufficient; (b) mesh-patterned SU-8 2000.5 master mold on a Si substrate. Line width, pitch and thickness are 840 nm, 3.5 μm and 500 nm, respectively. Left inset is the microscopic image of PDMS stamp surface detached from the master mold. Right upper inset shows a SU-8 2002 master mold on a Si substrate. Line width, pitch and thickness are 950 nm, 4 μm and 1.7 μm respectively. 47
Figure 4.7 NP patterns imprinted with PDMS stamp from a SU-8 2002 master mold. (a) Silver NP mesh patterns on a glass substrate. The line width is 790 nm; (b) Si NP mesh patterns imprinted on a Si/SiO_2 substrate. Line width is 580 nm; (c) ZnO NP line patterns imprinted on a glass substrate. The line width is 300 nm. 49
Figure 4.8 (a) SEM image of ZnO NP mesh patterns imprinted on a glass substrate using a PDMS stamp replicated from a SU-8 2000.5 master mold. The line width is 350 nm. The left inset represents an AFM image with a 200 nm feature height; (b) SEM image of ZnO NP line patterns imprinted on a Si wafer; (c) EDX analysis of point 1 and point 2 in (b); (d) ZnO NWs selevtively grown on the nanoimprinted ZnO NP seed patterns shown in (b)........ 50
Figure 4.9 (a) 4-inch master mold fabricated with SU-8 2000.5 on a Si wafer; (b) PDMS stamp from the master mold; (c) diffraction patterns from imprinted ZnO mesh patterns on a Si wafer; (d) diffraction patterns from imprinted ZnO mesh patterns on a quartz wafer; (E), (F) ZnO patterns on a flexible polycarbonate sheet........ 51
Figure 4.10 Line width of an OiR 700-10 photoresist after developing according to the laser power change. 610 nm groove width with residuals after developing when exposed to insufficient laser power (left inset). 870 nm Groove width with no residual when exposed to sufficient laser power (right inset)........ 53

Figure 4.11 (a), (c) SEM images of OiR 700-10 master molds on a Si wafer. Distances between grooves are (a) 2 μm and (c) 1.6 μm respectively; (b) SEM images of 1 μm diameter size ZnO dot arrays and (d) 500 nm size dot arrays imprinted on a Si/SiO_2 wafer with a PDMS stamp the from the master mold (a) and (c) respectively; (e) ZnO NP lines with 200 nm width imprinted on a Si/SiO_2 wafer; (f) photoimage of diffraction patterns from the ZnO dot arrays imprinted on a glass under fluorescent light illumination. 55
Figure 4.12 Rectangular laser pulse train with constant energy in every pulse. P_{peak}, E, Δt *and* T represents peak power, pulse energy, pulse duration and period respectively. (Source: a refined diagram from Spectra-Physics) 57
Figure 4.13 (a) By precisely adjusting the laser power or pulse energy close to the cross-linking threshold, a single structure smaller than the beam spot can be created; (b) as the direct writing pitch between two lines becomes smaller in the photolithographic process, the cross-linking threshold exceeds in the interstice, so that each line is unable to be developed separately. 58
Figure 4.14 Mesh structures generated by twice imprinting of TiO_2 NPs on a FTO glass substrate; secondly imprinted features (A) fill the interstices of the structures from the preceded imprinting process (B) resulting in a reduced pitch. 59
Figure 4.15 Multiple imprinting processes generate multilayer structures. (a) two layers; (b) three layers on FTO glass substrates 60
Figure 5.1 Process schematics of the direct patterned ZnO NW growth from the inkjet-printed ZnO NPs. 64
Figure 5.2 (a) Schematic diagram of the inkjet printing system setup; (b) time resolved image of the ZnO seed NP inkjet printing by piezo-electrically driven drop-on-demand inkjet printing system 66
Figure 5.3 Selective ZnO NW growth (a-d) without natural convection suppression and (e-h) with natural convection control. Note the secondary growth in (a-d) and the absence of the secondary growth in (e-h). 68
Figure 5.4 (a), (b) SEM pictures of selective ZnO NW growth on the inkjet-printed ZnO NP seeds; (c), (d) cross sectional SEM pictures of ZnO NWs. 69
Figure 5.5 SEM pictures of the ZnO NW grown on a single drop of inkjet printed ZnO seed NPs. (a) Tilted view; (b), (c) magnified cross sectional view at the center and at the edge; (d) cross sectional view of the ZnO NW array on one inkjet droplet. 70
Figure 5.6 (a) SEM pictures of ZnO NW arrays with various diameters from few microns to several hundreds microns; (b) SEM pictures of the inkjet-printed ZnO seed NPs (right) and actual ZnO NW growth (left) on the seed NPs; (c) magnified SEM picture of small diameter ZnO NW arrays in blue box in Figure 5(a). Red and blue dotted circles represent original inkjet-printed seed diameter and total diameter of ZnO NW patterned growth respectively. 71
Figure 5.7 (a) Twice grown and (b) original initially grown ZnO NWs at the edge of the inkjet-printed NP seed. 72
Figure 5.8 (a) SEM pictures of the ZnO NW growth at various droplet spacing; (b), (c) ZnO NW bridges between two circular ZnO NP seed droplets; (d) check shape ZnO NW growth; (e) 3 times grown check shape ZnO NW growth 73
Figure 5.9 Line and dot patterned ZnO NW arrays on a plastic substrate (PI) 74

Figure 6.1 Two routes for hierarchical ZnO NW hydrothermal growth. Length growth (LG) (a-b-c), branched growth (BG) (a-b-d), and hybrid (a-b-c-d-e). Notice polymer removal and seed NPs for branched growth. 78

Figure 6.2 SEM pictures of ZnO NWs on FTO glass substrates. (a) Length growth (1,2,3 times growth). Seed effect: first generation branched growth (b) without seeds and (c) with seeds after polymer removal. Polymer removal effect: first generation branched growth (d) without polymer removal and (e) with polymer removal after seed NP deposition. Polymers on ZnO NW are removed after 350°C heating for 10 min. 80

Figure 6.3 SEM pictures of ZnO NW nano-forest on a FTO glass substrate. (a) tilted view; (b) cross section view; (c) magnified view of backbone (red dotted line) and first generation branches (blue dotted line); (d) magnified view of a branch........... 81

Figure 6.4 (a) Schematic structure; (b) J-V curve of dye-sensitized solar cell with "*nanoforest*" ZnO NW 83

LIST OF TABLES

Table 1.1. ZnO properties [1].. 2

Table 3.1. Thermal properties of quartz and silicon substrates....................................... 35

Table 4.1 Imprinted feature sizes of various NPs from a SU-8 photoresist master mold 52

Table 4.2 Imprinted ZnO NP feature sizes with groove pitch variation on the OiR 700-10 photoresist master mold 54

Table 6.1 Characteristics of "*nanoforest*" ZnO DSSCs in **Figure 6.4b**. 84

NOMENCLATURE

AFM: atomic force microscopy
AZO: aluminum doped zinc oxide
BG: branched growth
C_{ox}: capacitance of the silicon oxide
CAD: computer aided design
CNT: carbon nanotube
CW: continuous wave
DOD: drop on demand
DSSC: dye sensitized solar cell
E: pulse energy
EBL: electron beam lithography
EDX: Energy dispersive x-ray
EUV-IL: Extreme Ultra-Violet Interference Lithography
f: repetition rate
FIB: focused ion beam
FTO: F-doped SnO_2
FWHM: full width at half maximum
g_m: , transconductance
GZO: gallium dope zinc oxide
HMTA: hexamethylenetetramine
I_{ds}: source-drain current
IPA: isopropyl alcohol
ITO: indium tin oxide
J_{SC}: current density
k: thermal conductivity
L: channel length
LED: light emitting diode
LG: length-wise growth
LIFT: laser-induced forward transfer
N.A.: numerical aperture
NIL: nanoimprinting lithography
NP: nanoparticle
NW: nanowire
P_{avg}: average power
P_{peak}: peak power
PC: polycarbonate
PDMS: polydimethylsiloxane
PEB: post exposure bake
PEI: polyethylenimine
PEN: polyethylene naphthalate
PES: polyethersulfone
PET: polyethylene terephthalate
PI: polyimide
PLD: pulsed laser deposition

ps: picosecond
PVP: poly(N-vinyl-2-pyrrolidone)
R_s: sheet resistance
RIE: reactive ion etching
RMS: root-mean-square
SAW: surface acoustic wave
SEM: scanning electron microscope
SIMS: secondary ion mass spectrometry
SPL: Scanning Probe Lithography
STED: stimulated-emission-depletion
t: film thickness
Δt: pulse duration
T: period
TEM: transmission electron microscopy
TFT: thin-film field-effect transistors
UV: ultra-violet
V: volatage
V_{ds}: source-drain voltage
V_{gs}: gate voltage
V_O: oxygen vacancy
V_t: threshold voltage
W: channel width
XPS: X-ray photoelectron spectroscopy
XRD: X-ray diffractometer
Z_{in}: zinc interstitial
ZnO: zinc oxide
α: thermal diffusivity
λ: wave length
μ: electron mobility
ρ: resistivity

Chapter 1

Introduction

1.1 ZnO – a versatile material for various optoelectronic device applications in the field of nanoscience

Zinc oxide (ZnO) has a long history of usage in electronics. The number of papers including several extensive reviews and books [1-3] which report on optical and electrical properties of ZnO is too large to be listed here. The main impetus of research on ZnO as a semiconductor material is the potential use of its wide direct band gap (3.37 eV) and a large exciton binding energy (60 meV). A large band gap means the material will not absorb photons with less energy than the band gap and leads to transparency for wavelength > ~370 nm, which makes ZnO one of the most important materials for transparent electrodes as an alternative to tin-doped indium oxide (ITO). Currently ITO, is the industry standard for transparent conducting applications. Unfortunately, however, the abundance of indium (In) is low and the cost is high, which hinders curtailing production cost. Due to the large exciton binding energy of ZnO, compared with GaN which has a similar bandgap (~3.4 eV) with a low exciton binding energy (~28 meV) [4], excitonic gain mechanism could be expected at room temperature for ZnO-based light emitting devices [1]. Moreover, ZnO itself is environmentally benign and non-toxic, so that it is used for cosmetics, ointment and even for food additive. ZnO also has interesting characteristics such as ferromagnetism and piezoelectricity. Its ferromagnetic characteristic when alloyed with magnetic atoms such as manganese (Mn), cobalt (Co) and nickel (Ni) makes ZnO as a material for spintronics applications [5]. Due to its excellent piezoelectric properties resulting from the polarity of ZnO, there are several applications of ZnO in piezoelectric devices such as surface-acoustic wave (SAW) devices and sensors [6-9]. **Table 1.1** shows primary properties of ZnO.

Table 1.1. ZnO properties [1]

Mineral	Zincite
Band gap [eV]	3.37
Exciton binding energy (meV)	60
Lattice structure	Hexagonal wurtzite
Lattice constant (nm)	a = 0.325, c = 0.5207
Density ($g \cdot cm^{-3}$)	5.67
Molar mass ($g \cdot mol^{-1}$)	81.408
Thermal conductivity ($W \cdot m^{-1} \cdot K^{-1}$)	$69_{\parallel}, 60_{\perp}$
Thermal diffusivity (10^{-6} K^{-1})	$2.92_{\parallel}$ $4.75_{\perp}$
Melting Temperature (°C)	1975
Boiling Temperature (°C)	2360

Recently, ZnO has been gathering great interest of researchers in nanoscience due to its diverse and versatile morphologies such as nanoparticles (NP) [10, 11], nanowires (NW) [12], nanorods [11, 13], nanotubes [14, 15], nanosprings [16], nanohelixes [17] and nanobelts [18]. One-dimensional (1-D) ZnO nanostructures are considered to be one of the most important semiconducting nanomaterials along with carbon nanotuces (CNTs) and silicon NWs for fabricating nanodevices for applications in optics, electronics, mechanics, and biomedical sciences such as solar cells [12, 19], UV lasers [20, 21], field-emission devices [22-24] , light-emitting diodes (LED) [25-27] and bio-sensors [28, 29]. Among their various applications, functional 1-D nanostructured photoelectrodes have been extensively studied and could significantly improve the electron diffusion length in the photoelectrode films by providing a direct conduction pathway for the rapid collection of photogenerated electrons. The direct pathway along 1-D crystalline nanostructures would diminish the possibility of charge recombination during interparticle percolation. On the other hand, nanosized ZnO particles are important for their potential conversion into a colloidal phase which is an attractive candidate for a low-temperature and solution-processible semiconductor. It is challenging to disperse micrometer-long NWs in a solution for simple printing-based or solution-coating deposition. Smaller colloidal nanocrystals [11] make it easier to solve this problem enabling them to be drop casted or spin coated on a substrate for thin film applications such as transparent electrodes and thin-film field-effect transistors (TFTs) [11, 30].

1.2 Direct writing technologies

Direct writing also known as direct printing and digital writing refers to fabrication method that employs a computer-controlled translation stage, which moves either a substrate or a pattern-generating device such as laser writing optics or ink deposition nozzle to create material patterns with controlled architecture and composition. [31]. Direct writing technologies are of increasing importance in materials processing and micro-nano fabrications since structures are built directly without the use of masks, allowing rapid patterning at reduced costs. Moreover, many direct writing technologies are compatible with flexible polymer substrates such as polycarbonate (PC), polyimide (PI), polyethylene terephthalate (PET), polyethylene naphthalate (PEN) and polyethersulfone (PES). Flexible polymer substrates are easily damaged by aggressive chemicals such as the developer and etchant in conventional photolithographic process. So far, various kinds of direct writing techniques have been developed, including inkjet printing [32-34], laser direct annealing [30, 35-39], screen printing [40-42], solid state embossing [43-45], dip-pen nanolithography [46-48], laser-induced forward transfer (LIFT) [36, 49, 50] and focused ion beam (FIB) direct writing [51, 52]. Extensive review papers for various direct writing technique can be found elsewhere [31, 53]

Among those direct writing techniques, laser direct writing (LDW) for nanomaterial annealing offers several advantages. Compared with furnace annealing which is high energy consuming, slow and limited by the peak processing temperature, heating/cooling rate, and the forming gas composition, laser direct annealing provides higher processing temperature while minimizing thermal impact on the substrate due to optimized energy delivery in spatial and temporal domain. Besides, the high temperature up to the melting point that can be easily produced by laser processing increases the sintering between NPs [35] and increases the concentration of defects [54] and doping, while the fast accessible cooling rate which is more than orders of magnitude higher than those obtainable in furnace heating will retain defects/doping profiles and influence crystalline structures [39]. The laser wavelength can be chosen according to the absorption peak of the respective nanomaterials to induce selective absorption, i.e. only the nanomaterial layer directly absorbs the laser energy diminishing the thermal impact to the substrate [38]. Thus, integrated with CAD system, laser direct annealing enables selective patterning without mask, which provides an effective way for low temperature, high resolution and high throughput patterning of a variety of materials on various substrates including flexible polymers.

Applying LDW to the photolithographic process presents a very effective way in prototype fabrication process. Since the feature size and shapes are easily tunable by choosing appropriate optical components and scanning parameters, various kinds of pattern design can be tested without making pricey masks repeatedly. Submicron size features, usually generated by the e-beam lithography, also can be obtained by tightly focusing a laser beam. For example, employing a femtosecond laser enables to fabricate three-dimensional structures with up to 100 ~ 200 nm resolution through multi-photon polymerization. On the other hand, laser interference lithography [55, 56] can overcome the slow throughput speed of the "serial" process with the resolution comparable to that

of the e-beam lithography, even though the setup becomes more complicated and is restricted to producing periodic patterns only. LDW combined with direct imprinting of nanomaterials [57, 58], albeit still a “serial” process, presents an alternative way to produce submicron size features with much faster than the e-beam process, much easier and simpler than the laser interference lithography. Other types of LDW processes and the discussion of the advantages and disadvantages of them can be found elsewhere [53] and will not be repeated here.

There has been a great progress in inkjet printing technology since the first ink jet printer was invented in 1976. The application of inkjet printing encompasses from small desk-top printers to in-line coding and marking tools for vast manufacturing process. Recently, along with the development of solution-type nanomaterials, inkjet printing technology is expanding its applications in nanomaterial deposition and patterning. Inkjet-based direct writing involves the formation and deposition of ink, or a sequence of droplets of liquid phase material. The evaporation of the solvent or chemical changes follows to transform the ink into a solid phase [53]. Subsequent processing steps, such as annealing, may also be involved [53]. In the drop on demand (DOD) ink jet processing [32, 59], drops of ink are on demand ejected from the system in response to a trigger signal through the generation of a pressure pulse by an actuator when they are required to be printed. Integrated with computer aided design (CAD) system, the fully data driven and maskless nature of DOD method allows more versatility than other direct printing methods with high degree of freedom [32, 34]. The method is especially efficient when precious materials are used, since waste of the materials can be considerably diminished. Also inkjet printing process is compatible with flexible substrates and can be scaled up for larger substrates for mass production or roll-to-roll process.

1.3 Scope of the dissertation

This dissertation presents methodical studies covering from the synthesis of ZnO nanomaterials to deposition & patterning methods and their applications for optoelectronic components and devices such as transparent electrodes, active layers for thin film transistor (TFT) and photovoltaics.

In chapter 2, several methods for synthesis of ZnO NPs and NWs are explained and characterizations of those materials are presented. These materials are used for the researches in the following chapters.

In chapter 3, annealing process of solution-deposited ZnO thin film by UV-picosecond (ps) laser for conductive transparent ZnO patterning is presented. Parametric studies including the sheet resistance and optical transmittance of the annealed ZnO NP thin film were conducted with various laser powers and background gas conditions for process optimization. A ZnO TFT performance test is also discussed which shows that by just changing the laser parameters, the solution-deposited ZnO thin film can also perform as an active layer for TFT. The results demonstrate that laser annealing offers tunability of solution-deposited ZnO thin film properties for both transparent conductors and semiconductor active layers.

In chapter 4, large area nanoimprinting of NPs on various substrates by LDW-assisted mold fabrication process is presented. This work presents laser assisted high speed one-step direct nanoimprinting of metal and semiconductor NPs to fabricate submicron structures such as mesh, line, nanopillar and NW arrays. Moving away from the traditional electron-beam lithography method for master mold fabrication, LDW process was applied. A 200 $mm \cdot s^{-1}$ writing speed was achieved *via* UV ps laser process which enables rapid fabrication of wafer scale master molds.

In chapter 5, a fully digital selective ZnO NW array growth on the inkjet-printed seed patterns are presented. Not only inkjet printing process integrated with CAD system, but also proper natural convection suppression during the hydrothermal growth for successful ZnO NW local growth is introduced.

In chapter 6, a selective growth of *"nanoforests"* composed of high density, long branched tree-like multi generation hierarchical ZnO NW photoanodes for enhanced efficiency of ZnO dye sensitized solar cells (DSSCs) is presented. A parametric study to determine optimum hierarchical ZnO NW photoanodes through the combination of both length-wise and branched growth processes is performed as well.

Chapter 2

Synthesis of ZnO nanostructures

The ZnO nanostructures – NPs and NWs – are the core materials for the research in the following chapters.

Various methods for the preparation of ZnO NPs such as the sol-gel method [60, 61], laser ablation in liquid [62], flame spray pyrolysis [63], vapor phase oxidation [64], wet chemistry method [10, 11] have been reported through many research papers. Among various methods, wet-chemistry-based procedures were used since it presents a reliable, safe and economical way while producing very fine NPs.

The synthesis of nano/micro size ZnO NWs has been carried out using various methods, including evaporation and condensation [65], physical vapor deposition [66], chemical vapor deposition [67], solvothermal [68] and hydrothermal method [12, 19, 69]. Among them, the hydrothermal method is one of the most attractive due to rapid, low-cost, low temperature, environmentally friendly process nature [70]. Thus, the ZnO NWs for the following research were synthesized by the hydrothermal method.

The synthesis methods for both ZnO NPs and NWs are solution-based processes, hence do not require any vacuum system or gas phase chemicals. Also all procedures are performed under low temperature.

2.1 Synthesis of ZnO NPs

Here, a method producing solution processible, variable concentration transparent ZnO NP solution is presented. Two wet-chemistry-based methods using different solvents were adopted for the following researches. One is ethanol [C_2H_6O]-based method and the other is methanol [CH_4O]-based. Ethanol-based method produces low concentration NP solution which was used for the seed layer for ZnO NW growth.

Methanol-based method produces higher concentration NP solution facilitated to produce ZnO thin film after post-processing. It is noted that much diluted NP solution synthesized by methanol-based method also can be used for ZnO NW growth.

2.1.1 Ethanol-based method

ZnO NPs from this method were used as seeds for the subsequent selective ZnO NW growth. ZnO NP ink was prepared by modifying the original method by Pacholski [10, 11, 71]. A NaOH solution in 32.5 mL of ethanol (0.03 M) was added slowly to a solution of zinc acetate dihydrate (0.01 M) in 62.5 mL of ethanol at 60°C and stirred for two hours. The resulting ZnO NP solution in ethanol is approximately 30 nM and stable for at least two weeks in solution. The ZnO NPs were 5~10 nm in diameter with spherical shape.

2.1.2 Methanol-based method

ZnO NPs were synthesized from zinc acetate [$Zn(O_2CCH_3)_2$] precursor solution. The synthesis details can be found elsewhere [11]. 4.46 mM of zinc acetate [$Zn(O_2CCH_3)_2$] and 0.25 mL of DI water were added into a flask containing 42 mL of methanol. The solution was heated to 60 °C with vigorous stirring until the zinc acetate was fully dissolved. 7.22 mM of potassium hydroxide [KOH] was dissolved in another flask containing 23 mL of methanol. Then, the potassium hydroxide solution was dropped into the zinc acetate solution flask within 10~15 min minimizing the temperature fluctuation of the mixture solution from 60 °C. After 2 h and 15 min at 60 °C with vigorous stirring produces the milky ZnO NPs solution. This method could be easily scaled up. It is noted that without adding the small amount of the water ZnO NPs were not produced after 2 h and 15 min. As seen on **Figure 2.1**, after the reaction, the ZnO NP solution looks milky (a) and the NPs precipitate after several hours (b). When as-synthesized methanol-based solution is spin coated on a glass substrate, the film surface is not uniform and white powder remains on it since the NPs agglomerate each other (**Figure 2.2**). Therefore, as-synthesized ZnO NP solution is not suitable for transparent thin film coating.

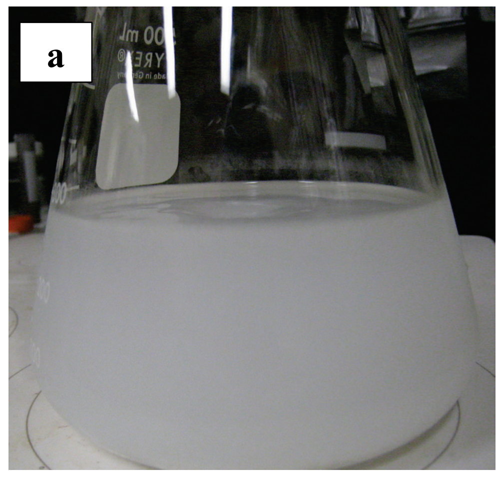

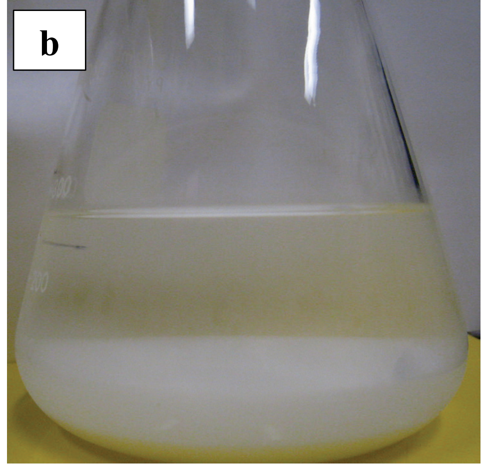

Figure 2.1 (a) Milky ZnO solution after reaction; (b) precipitation of the ZnO NPs

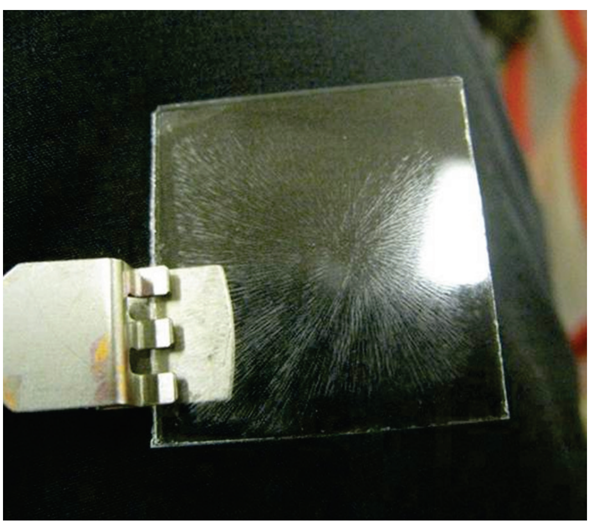

Figure 2.2 Spin-coated ZnO NP film on a glass substrate with the ZnO-methanol solution

2.2 Synthesis of transparent ZnO NP solution

Since as-synthesized ZnO NP solution is not transparent and has low concentration, post processing is required for transparent high-concentration solution to be applied for high quality transparent thin film coating. As a post processing, 14* mL of as-synthesized ZnO NP solution was centrifuged for 5 ~ 15 min to separate the NPs from the solvent. After discarding supernatant liquid, without drying up, 1** mL of 1-pentanol [$CH_3(CH_2)_4OH$] was added and sonicated until the solution becomes transparent.

Technically, small amount of methanol remains in the 1-pentanol solution. Theoretical, or, maximum ZnO concentration obtainable through this whole process is 9.563 wt%. Measured ZnO concentration after the post processing was 7.5 wt%, where post processing showed at least 78 % ZnO NP recovery. By adjusting either volume of * or **, the concentration of resultant ZnO solution can be easily modified. **Figure 2.3a** shows ZnO NP well-dispersed in 1-pentanol solution. No precipitation in the solution was observed for more than 3 weeks. As the concentration of ZnO NPs in solution increases, the solution becomes cloudy. However, when spin-coated, as displayed in **Figure 2.3b**, the thin film appears transparent. The solution fluoresces under UV light (**Figure 2.3c**). Various solvents such as alpha-terpineol, diethylamine, 1-propanol, 2-propanol which are usually used as solvents for NP dispersion were tested to make transparent ZnO solution. As seen on **Figure 2.4**, however, ZnO NPs agglomerate in those solvents and precipitate resulting in milky solution. Hexane, toluene, ethanol and ethylene glycol were also tested and yielded the same result.

The described results carry significant potential, in that they demonstrate an simple and efficient method producing highly transparent and very well dispersed ZnO NP solution by just changing a solvent without additional chemicals for a capping layer. NPs, in general, need a capping layer during synthesis process to prevent agglomeration with each other in the solution, such as poly(N-vinyl-2-pyrrolidone) (PVP) for Ag [72, 73] and Cu [74] NPs or hexanethiol [$CH_3(CH_2)_5SH$] for Au. The method described here, on the other hand, does not require additional capping layer chemicals and presents how to disperse the NPs after finishing synthesis in a very simple way. Furthermore, the method has following additional advantages. First, the size of NPs in the solution is very small (6 nm) and uniform. Second, the synthesis process is energy-saving and safe since all the procedures are performed under 60 °C. Third, no expensive equipment is needed. Fourth, the method is readily scalable. Fifth, it is easy to adjust final solution concentration for various applications such as thin film spin coating and printable ink. Sixth, the solution has very good wettability to glass, plastic, Si wafer, etc. so that surface treatment such as a corona discharging and a UV-ozone are not required. Lastly, the solution is stable up to several months. These attributes make the transparent ZnO NP solution far superior than the commercially available ones.

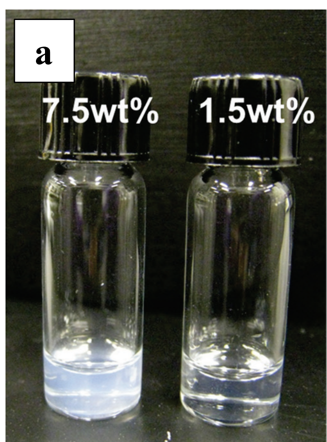

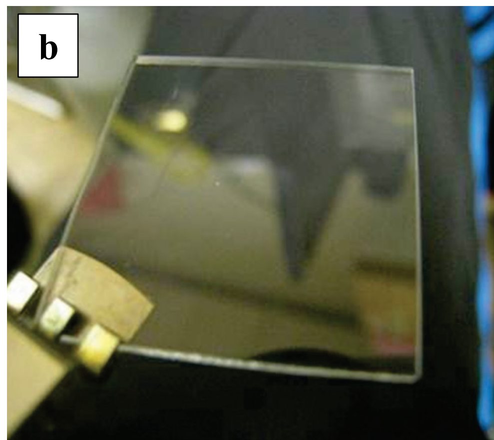

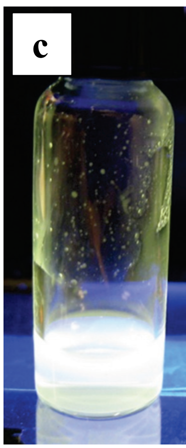

Figure 2.3 (a) ZnO NP solutions (solvent: 1-pentanol) with two different concentrations; (b) images of a spin-coated ZnO thin film (thickness: 170 nm) with the solution (a) on a glass substrate; (c) fluorescence of the ZnO solution under UV illumination (365 nm)

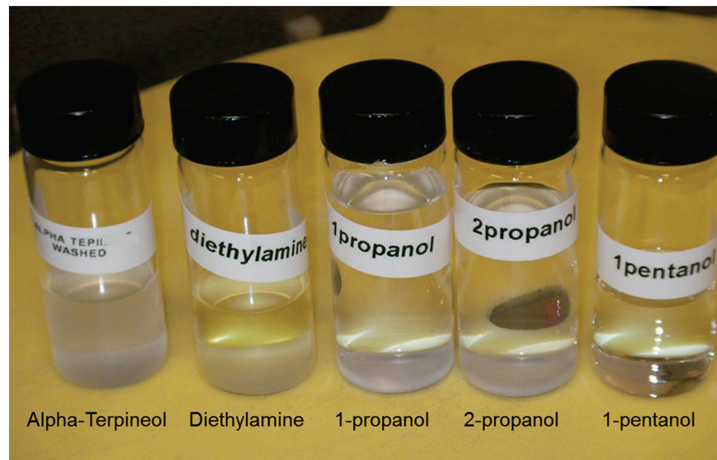

Figure 2.4 ZnO NPs dissolved in various solvents

2.3 Characterization of the ZnO NP solution and thin film

Ejected particles collected on a copper [Cu] grid were analyzed by transmission electron microscopy (TEM, FEI Tecnai 12, Philips). ZnO thin films spin-coated with the NP solution on quartz and silicon substrates were further analyzed by X-ray diffractometer (XRD, D500, Siemens) using Cu Kα radiation (λ = 0.154 nm) and X-ray photoelectron spectroscopy (XPS, PHI5400, Perkin-Elmer) equipped with a 350W Al

anode X-ray source for the crystallographic structure and elemental composition respectively. A scanning electron microscope (SEM, LEO 1550, Zeiss) was utilized to examine surface morphology. Transmittance data of the 1-pentanol ZnO NP solution was obtained by a spectroscopic ellipsometer (GESP5, SOPRA).

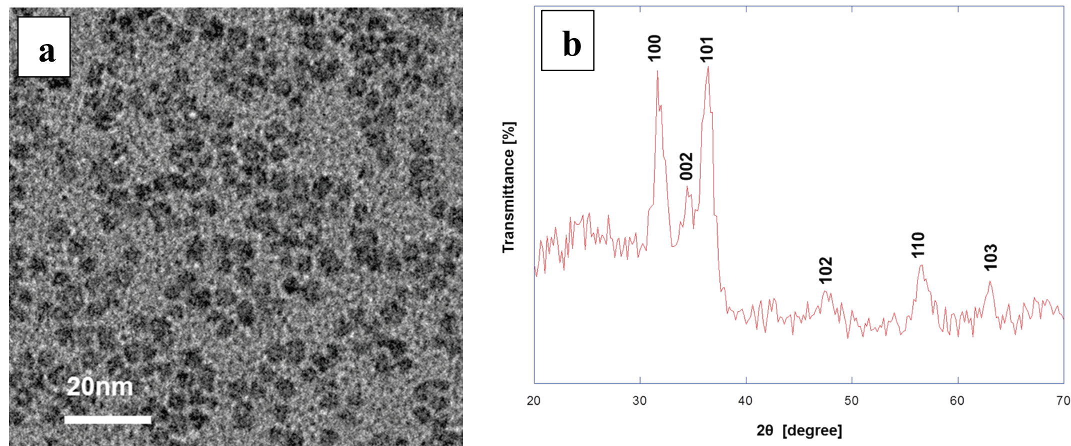

Figure 2.5 (a) TEM image shows the ZnO NP is 6 nm in diameter; (b) XRD pattern of the ZnO NPs shows crystallized wurtzite structure

TEM image and XRD pattern in **Figure 2.5a** and **2.5b** reveal that ZnO NPs are around 6 nm in diameter with crystallized wurtzite structure. As shown in the transmission measurement of pure solvent (1-pentanol) and ZnO solution (**Figure 2.6**), the ZnO NP solution has very strong absorption (blue line) near 355 nm which is attributed to ZnO bandgap (~3.37 eV). The XPS spectra (**Figure 2.7**) with only detectable XPS and Auger peaks of zinc and oxygen confirm that the ZnO thin film is undoped at the parts per thousand (1000 ppm) doping concentration level, which is the typical detection limit of XPS [75]. Very long collection time (8 ~ 16 h) of XPS data would improve the detection limit to ~100 ppm. More clear assurance of the doping concentration level would be possible by employing secondary ion mass spectrometry (SIMS) which enhances the detection limit up to ~ ppm [75]. Those characterizations will be left as future studies. The SEM image in **Figure 2.8** shows a film surface of spin-coated thin film on a quartz substrate.

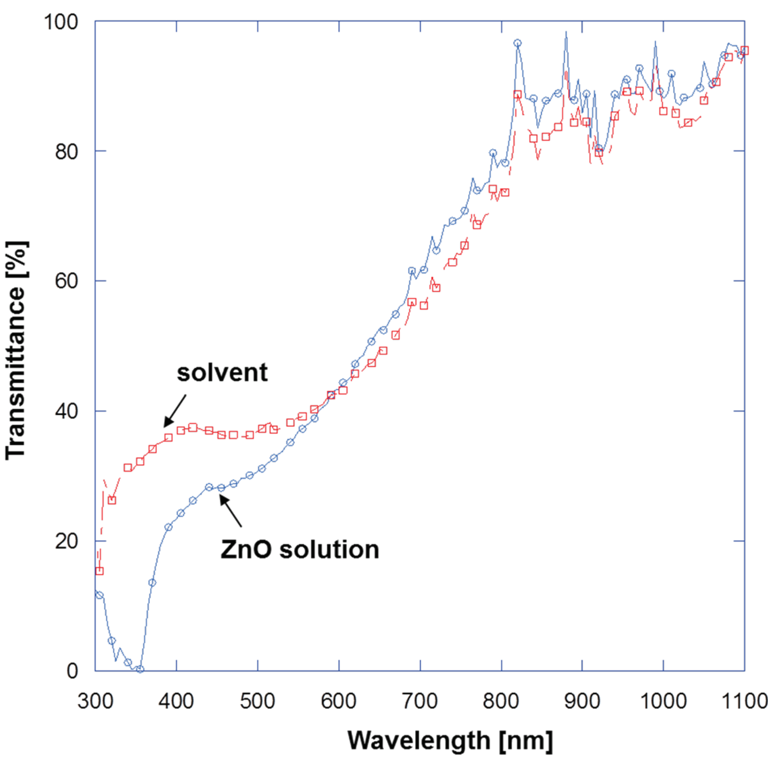

Figure 2.6 Optical transmission measurement of the ZnO solution shows very strong absorption at around 355 nm wavelength;

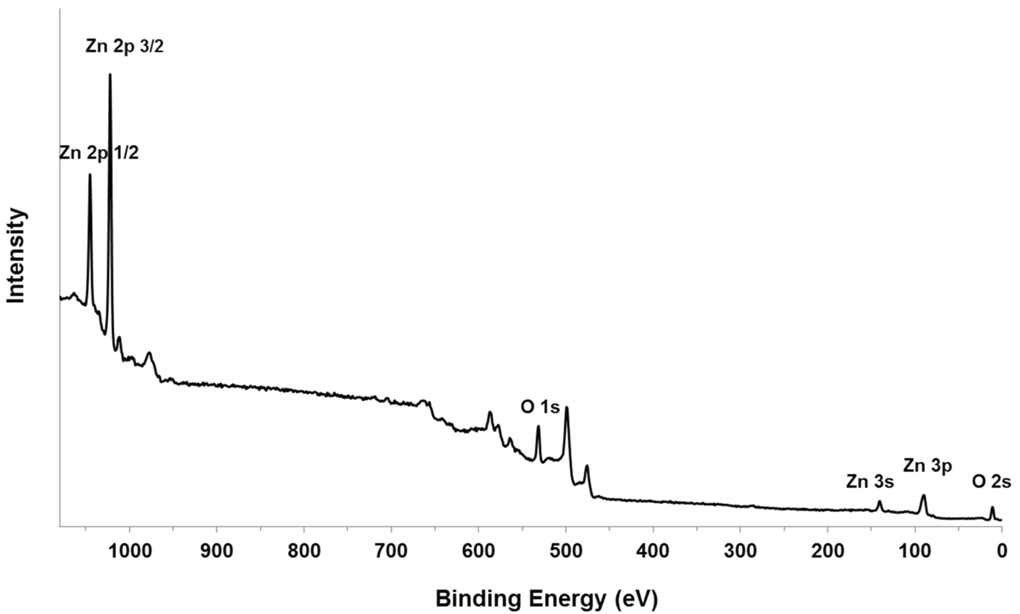

Figure 2.7 XPS spectra of the as-spin-coated ZnO NP thin film. Only XPS and Auger peaks of Zn and O were detected.

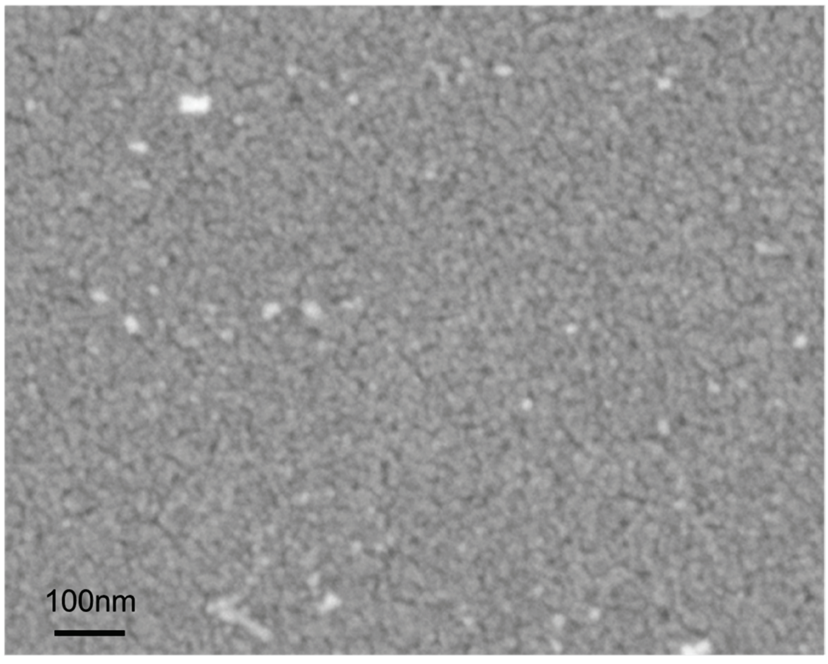

Figure 2.8 SEM image of the as-spin-coated ZnO NP thin film on a quartz substrate.

2.4 Synthesis of ZnO NWs

The ZnO NWs were synthesized by the hydrothermal method [12, 69]. For the ZnO NW growth a seed layer is required on a substrate to compensate lattice mismatch. There are several methods reported to deposit a seed layer for the ZnO NW growth which can be classified under two primary methods, one is NP seeds deposition [12] and the other is creating a thin film by sol-gel method [76]. For NP seeds layer, NPs solution synthesized by the method described in section 2.1 were deposited by drop casting. For sol-gel thin film seed layer, either diethanolamine [$C_4H_{11}NO_2$, DEA]-based precursor solution or monoethanolamine [C_2H_7NO, MEA]-based one was used. Details of the methods can be found in research papers [77, 78]. DEA-based solution was prepared by dissolving 0.75 M of zinc acetate dihydrate [$Zn(CH_3COO)_2 . 2H_2O$] and 0.75 M of DEA in ethanol. After spin coating of the solution on a substrate with 3000 rpm for 1min, the film was heated at 250°C for 10 min and 500°C for 1 h for hydrolysis. MEA-based solution was produced by dissolving 0.3 M of zinc acetate dihydrate and 0.3M of MEA with 1 M of deionized water. Spin-coated film with 3000rpm for 1min was heated at 250°C, 300°C and 500°C for 10 min, 10min and 5 min respectively. It is noted the heating temperature, time, concentration and solvent of sol-gel method vary in different research papers [77-79]. Since sol-gel method required high temperature post heating, it is not suitable to be used on substrates with low melting temperature. Thin film seed layers by the sol-gel method were used for the comparison purpose only in this section and NPs seed layer were adopted in the following chapters.

ZnO NWs were grown on a seeded substrate in aqueous precursor solutions containing 25 mM zinc nitrate hydrate [$Zn(NO_3)_2 \cdot 6H_2O$], 25 mM hexamethylenetetramine [$C_6H_{12}N_4$] (HMTA) and 0 ~ 7 mM polyethylenimine (PEI, branched, Average M_w~800) at 92 °C for over 2.5 hours [12]. Solution-grown ZnO NW arrays without PEI addition have been limited to aspect ratios of less than 20 [80]. PEI, a cationic polyelectrolyte, could boost the aspect ratio of ZnO NW above 125 by hindering only the lateral growth of the NWs in solution, while maintaining a relatively high NW density [12, 81]. The substrate was suspended upside-down in an open crystallizing dish filled with solutions to remove the unexpected precipitation of homogeneously grown ZnO NW on the substrate. When the substrate is placed face up, an impurity layer is formed on the surface, hence ZnO NW growth is prohibited.

Figures 2.9(a,b) show the grown ZnO NWs on F-doped SnO_2 (FTO) glass substrates without and with a ZnO seed layer. Only very thick nanorods were sparsely created on the substrate without a seed layer while thin NWs were densely 'grown' from the substrate with a seed layer. **Figures 2.10(a~c)** show ZnO NWs grown in PEI-contained (3 mM) precursor solutions on the silicon substrates with the NP seed layer, the DEA-based and MEA-based sol-gel thin film layers respectively. The overall shape of those NWs was similar while the density of and thickness of the NWs were slightly different. Intense investigation of those differences is beyond the scope of this research and left as a future study. The length of ZnO NWs grown overnight in the precursor solution is around 10 μm (**Figure 2.10a** inset). To grow longer NWs the precursor solution need to be replaced with a fresh one. As seen on **Figures 2.11(a,b)**, PEI in

aqueous precursor solution plays an important role in the shape and the thickness of the synthesized NWs. PEI makes the NW thinner and needle-like shape terminating the tip end very sharp, whereas NWs grown without PEI are thicker and have broken-rod shape tip ends. It is noted that choosing the molar mass of PEI and concentration is very important. Using high molar mass PEI such $M_w \sim 25000$ or high concentration of PEI in precursor solution would fail in growing NWs. More details of the effect of PEI concentration and/or pH of aqueous precursor solution on ZnO NW synthesis can be found elsewhere [69, 79, 82].

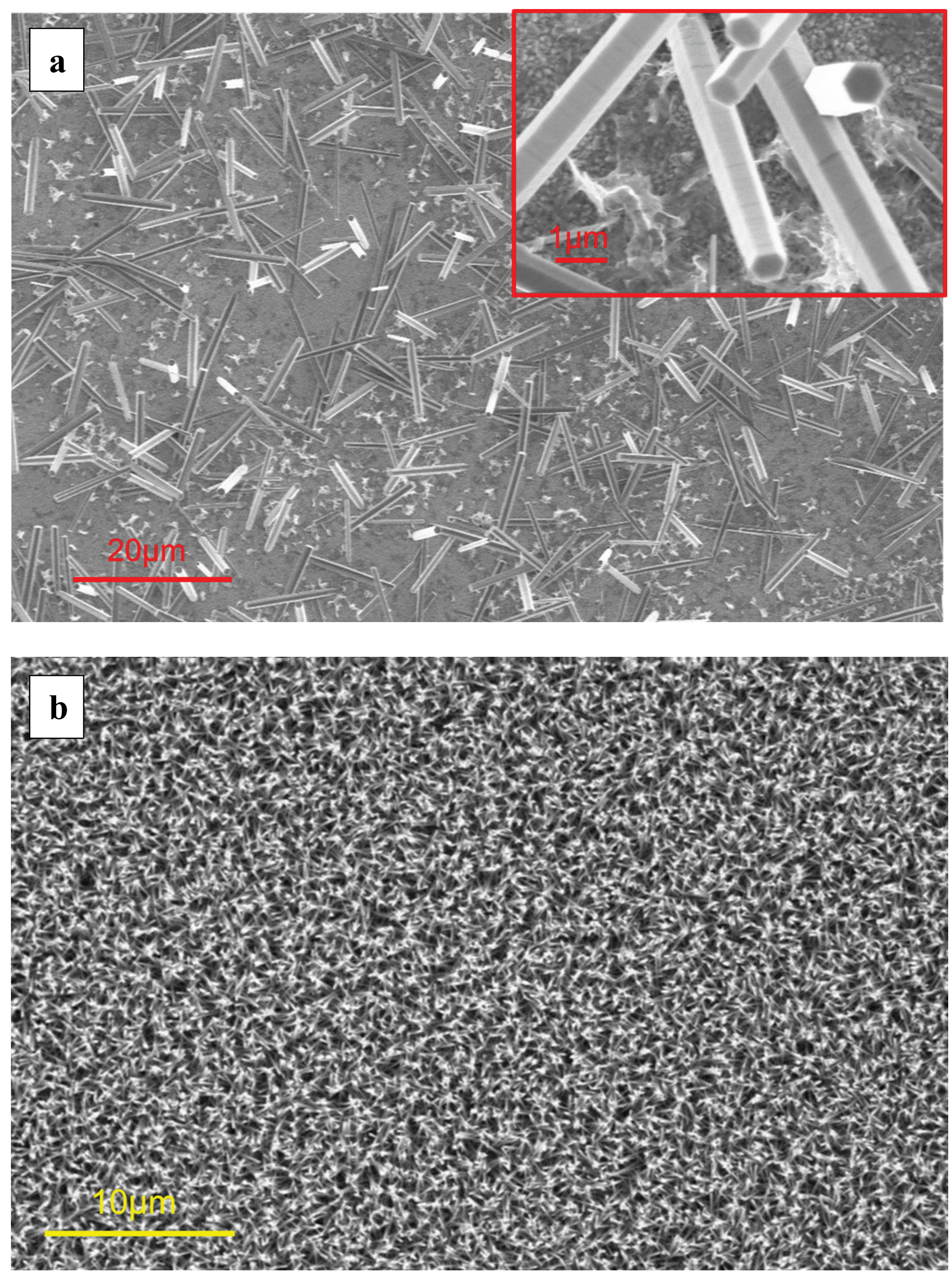

Figure 2.9 ZnO NWs grown on FTO glass substrates (a) without a NP seed layer; (b) with a NP seed layer

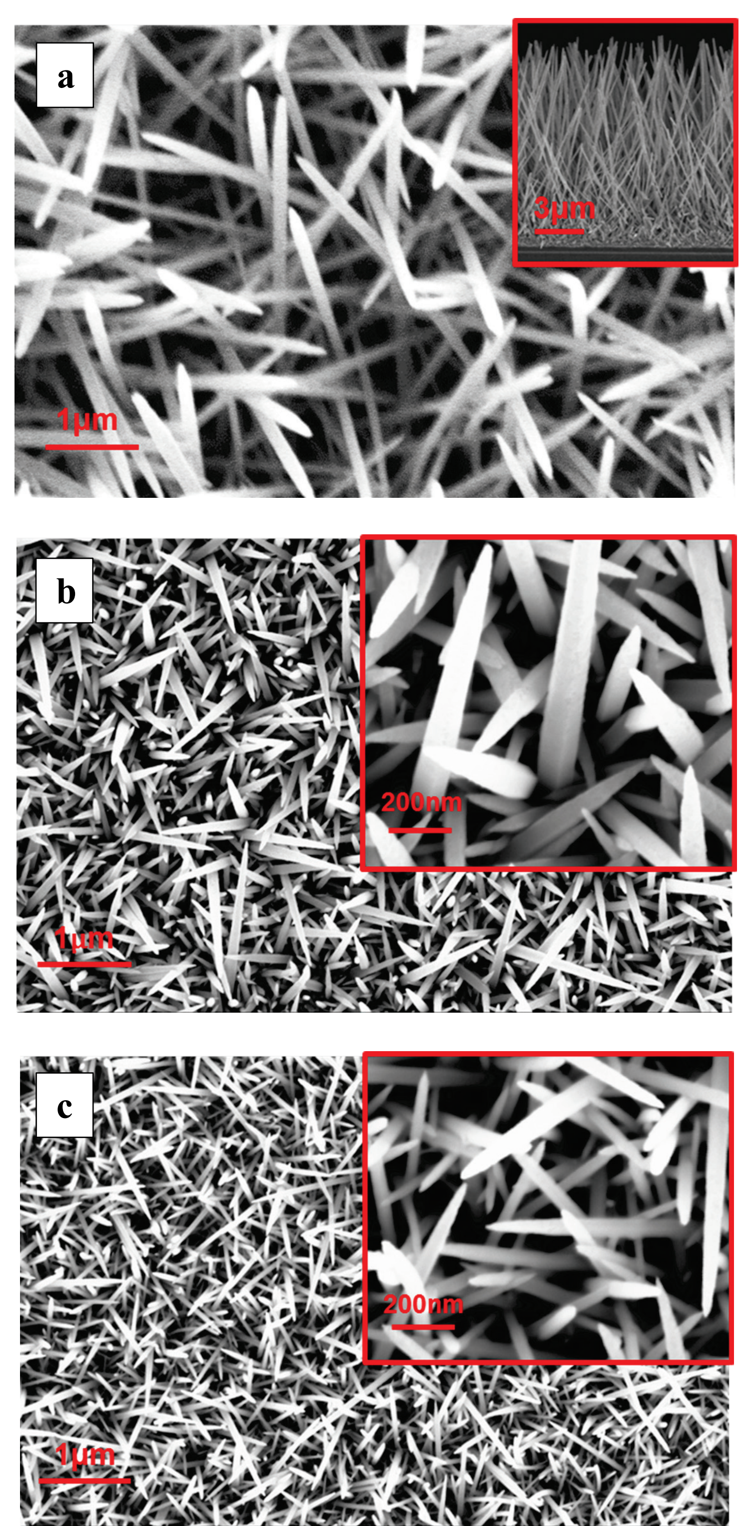

Figure 2.10 ZnO NWs grown on silicon substrates coated with (a) a ZnO NP seed layer (inset: side view); (b) a thin film by DEA-based sol-gel method; (c) a thin film by MEA-based sol-gel method

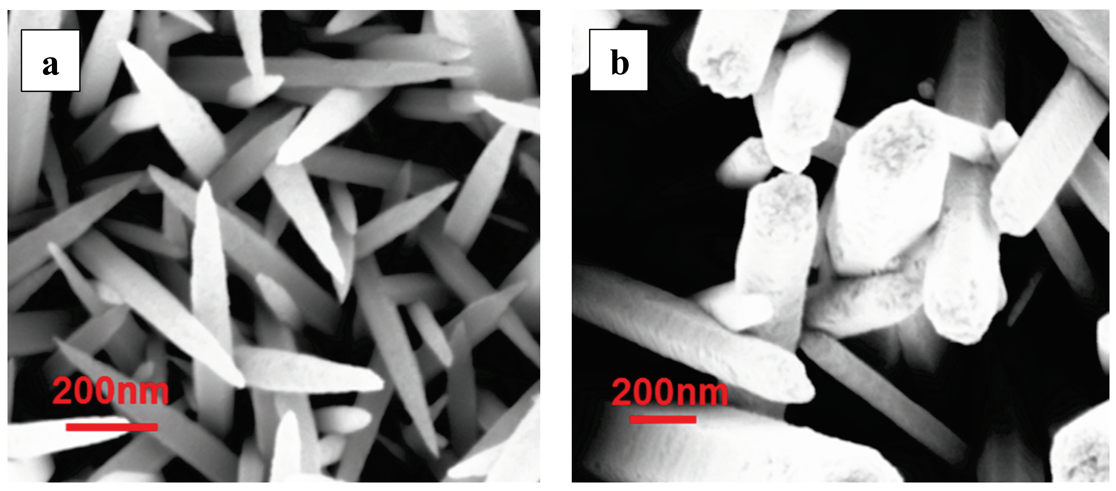

Figure 2.11 ZnO NWs grown on silicon substrates in the precursor solution (a) with PEI (3 mM); (b) without PEI

Chapter 3

Conductive transparent ZnO patterning by ultra-short pulsed laser annealing of solution-deposited NPs

LDW for solution-processed ZnO thin film annealing with ultra-short-pulsed laser was performed to change the film properties without using a blanket high temperature heating process. Although the as-deposited NP thin film was not electrically conductive, laser annealing imparted a substantial conductivity increase and furthermore enabled selective annealing to write conductive patterns directly on the NP thin film without a photolithographic process. Parametric studies including the sheet resistance and optical transmittance of the annealed ZnO NP thin film were conducted to find the optimized laser power and background gas conditions. The laser annealing developed in this work was also applied to the fabrication of a TFT that showed enhanced performance compared with furnace-annealed devices.

3.1 Introduction

Transparent conductors are being utilized in important material applications where precise control of optical and electrical properties is required. The role of the transparent conductor in optoelectronic devices is to deliver or collect electrons from the active layer of a device while at the same time allowing visible photons to pass through relatively unimpeded. The most popular materials for the transparent electrodes are tin-doped indium oxide (ITO) [39, 83-85], impurity-doped ZnO, e.g. In-, Al- and Ga-doped ZnO (IZO, AZO and GZO) [86-89] and impurity-doped SnO2, e.g. F-doped SnO_2 (FTO) [90, 91]. Arguably, metal oxides remain the most dominant materials for transparent

conductors, although newer materials such as carbon nanotubes (CNTs), metal NWs and graphene are actively being developed [92-95]. Among metal oxides, ITO is most widely used as a transparent conducting material due to its high electrical conductivity and transparency. However, ITO is less economical because of its high production cost and a recent indium shortage and unstable supply. ZnO is one of the most promising candidates for ITO substitutes due to its non-toxicity, low cost and relatively easy synthesis. ZnO thin films are usually deposited by a vacuum process such as DC or RF magnetron sputtering, or pulsed laser deposition (PLD) [86, 96-102] since those methods facilitate easier doping procedures yielding ITO-comparable high conductivity. Vacuum processes, however, need additional expensive equipment and hence complicate the fabrication sequence. An alternative approach to make ZnO thin films is *via* solution processing, including spin coating [103] or drop coating [104]. This approach enables attractive low-cost fabrication of printed electronics. A wide variety of stable solution-processible, vacuum-free routes to synthesize ZnO nanomaterials by the hydrothermal method have been developed, allowing cost-effective nanomaterial mass production [11, 105-109]. Solution-processing routes are broadly based on printing or coating of functional 'inks' that can be made of precursors for sol-gel processing [76, 110] or NPs dispersed in carrier solvents [11, 111, 112].

Whether the ink is made of precursors, colloidal solutions or NPs, a coated/printed film must be thermally annealed to improve the electrical and optical properties. Usually this annealing process, if done in a high-temperature oven or furnace, takes a long time (several hours) and needs high power consumption [101, 103, 111]. In order to overcome this problem, a novel laser post-processing (annealing) technique is proposed to modify the ZnO nanomaterial structure and thus control electrical and physical properties to achieve desired functional transparent conductor films. Utilizing an ultra-short-pulsed laser is advantageous in nanomaterial annealing because laser heating with high peak irradiance is very localized and rapid, and therefore easily controls thermal effects. The thermal effect control is not only important for minimizing the thermal damage to the substrate, but also to modify and fine tune desired material properties. In addition, laser process parameters can be digitized and therefore the process can be easily integrated with computer-aided design and a manufacturing system that can be changed on demand. Laser annealing also allows maskless direct-write patterning and thus avoids complex photolithographic processes and etching steps. Furthermore, laser processing is an ambient, room-temperature process and compatible with roll-to-roll manufacturing. In summary, laser post-processing of nanomaterials can enable a manufacturing paradigm shift with drastic productivity enhancement. Previous reports mostly focused on ZnO thin films either as a transparent oxide thin film [96, 97, 99, 111, 113] or as an active channel layer for field-effect transistors without demonstrating the tunability of ZnO thin film properties for both applications [103, 105, 106]. This research presents a simple method for synthesizing a transparent, high-concentration undoped ZnO NP solution and demonstrates that a spin-coated undoped ZnO thin film can be transformed to a highly conductive transparent thin film by laser annealing, as well as to an active channel layer of a thin-film transistor simply by changing the laser process parameters. Previously, a ZnO NP laser annealing experiment was performed with a nanosecond excimer laser [54], but it focused on the thin film as an active layer of a

transistor since the film resistance was too high and the transparency is not enough to be used as a transparent conducting layer replacing ITO or doped ZnO.

Here, with the newly synthesized NP solution and laser processing, this chapter demonstrates a highly transparent ZnO film conductor even without impurity doping that shows by a factor of 10^5 higher conductivity than the previously reported furnace-annealed ZnO NP films [111] and is also comparable to furnace-annealed ITO NP films [114]. Evidently, undoped ZnO NPs are stable and easy to synthesize and exclude the possibility of film property non-uniformity induced by uneven doping distribution [115, 116]. Such highly conductive transparent ZnO films, to the best of my knowledge, have never been achieved with undoped ZnO film before. As an example of another application, the current technology was also utilized to demonstrate a ZnO TFT that showed good performance with larger on/off ratio and high mobility.

3.2 ZnO thin films prepared by NP solution spin coating

ZnO thin films used for the research in this chapter were prepared by spin coating of ZnO NP solution. Full details of the ZnO NP solution and thin film characterization have been elucidated in chapter 2. ZnO thin films were spin coated on a pre-cleaned quartz or glass substrate from the NP solution for 1min at 2000 rpm. Once the solution is dispensed on the substrate, it should be spun within 1 min due to the evaporation of the solvent. As the time delay between solution dispensing and spinning increases, the film becomes thicker, but the film thickness becomes less uniform, or thicker at the substrate edge. The films used for this characterization were spun 30s after solution dispensing. The spin-coating process was then repeated to obtain the films with the desired film thickness. Twice spin coating results in film thickness of 175 nm which will be shown later in the following section. Post heating around 100 ~ 150 ºC per spin coating is helpful for the fast solvent drying and adhesion promotion of the ZnO NPs to the substrate but not necessarily required. The spin-coated ZnO NP thin film behaves almost as an electrical insulator due to the poor connectivity between the ZnO NPs as shown in **Figure 2.8**. This non-conductive as-spin-coated ZnO NP thin film essentially acts as a drawing paper or canvas for forming conductive patterns *via* the subsequent selective laser annealing.

3.3 Experimental setup

The schematic view of the laser annealing experimental setup to tune the electrical and physical properties of the ZnO thin film is shown in **Figure 3.1**. A yttrium vanadate ($Nd:YVO_4$) ps UV laser (Newport, wavelength: 355 nm, pulse width (full width at half maximum): 12 ps, pulse repetition rate: 80 MHz) was applied normal to the substrate to induce local heating of ZnO thin films. With a single convex lens (40 mm focal length), a Gaussian beam profile of 25 μm ($1/e^2$) diameter was obtained at the focus.

The applied laser power was varied from 32.6 kW·cm^{-2} to 98.9 kW·cm^{-2} The ZnO thin film on the quartz substrate was mounted on an *X-Y* motorized stage. The stage was operated with a scanning speed of 0.1 - 10 mm·s^{-1}. To measure thin film sheet resistance, a 15 mm × 15 mm area on the quartz substrate was scanned using 10 μm overlap between lines. In order to create arbitrary micron-size patterns on a soda-lime glass slide, the single convex lens was replaced by an objective lens. Scanning electron microscopy (SEM, LEO1550, Zeiss) and atomic force microscopy (AFM, XE-NSOM, Park Systems), were utilized to characterize the morphology of the film surface. Micron-size patterns were taken with an optical microscope (BX60, Olympus). The sheet resistance (R_s) was measured using a four-point probe. Assuming a uniform film thickness, the film resistivity (ρ) was determined by $\rho = R_s \times t$, where t is the film thickness. All sheet resistance measurements were performed with five or six different samples per each annealing condition. The normal-incidence transmission was measured with spectroscopic ellipsometry (J.A. Woolam Inc).

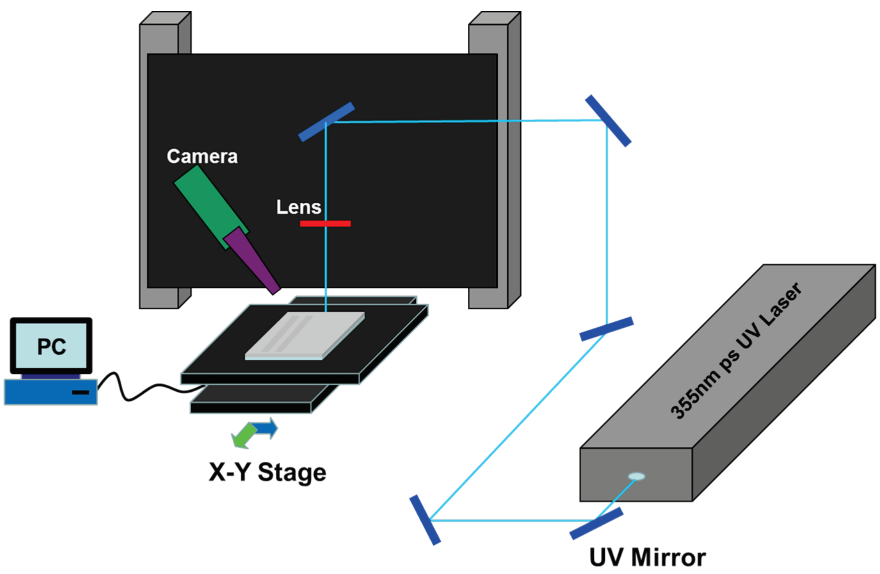

Figure 3.1 Schematic illustration of the picosecond laser annealing setup

3.4 Laser annealing

Laser annealing could change the structural and electronic characteristics of the ZnO thin film. Furthermore, the degree of change was tunable by varying the laser annealing parameters such as laser power and scanning speed. **Figure 3.2** presents ZnO transparent conductor thin film patterns after laser annealing on a quartz substrate. Annealed parts have greatly reduced sheet resistance, as will be discussed in detail later. The SEM image in **Figure 3.3** shows the ZnO thin film surface and cross-section. Before laser annealing, a granular and nano-porous structure with 175 nm film thickness was

observed. Upon laser annealing, the grains fused, reducing voids and the film thickness decreased to 95 nm, revealing that laser annealing densifies the film. AFM images of a randomly selected 20 μm × 20 μm surface area in **Figure 3.4** show the change of root-mean-square (RMS) roughness of the thin film from 17 nm to only 1.7 nm after annealing, which demonstrates excellent film smoothness. Variation of the scan speed in the range from 0.1 $mm \cdot s^{-1}$ to 10 $mm \cdot s^{-1}$ does not affect the sheet resistance of the ZnO thin film. This finding is attributed to the very high repetition rate of the laser pulse (80 MHz) that provides a sufficient number of pulses to change the film properties even at 10 $mm \cdot s^{-1}$ scan speed. However, implementation of much higher scan speeds could affect the sheet resistance. The sheet resistance variation of the ZnO thin film annealed with different laser powers is shown in **Figure 3.5a**. The scan speed was fixed at 10 $mm \cdot s^{-1}$. An optimum laser power window could be identified with respect to the film conductivity, as annealing with excessively high or low power produces the film with high resistivity. Excessively high laser power degrades the film quality yielding high roughness and cracks, as shown in **Figure 3.5b**, while in contrast too low laser power cannot fully anneal the ZnO NP film.

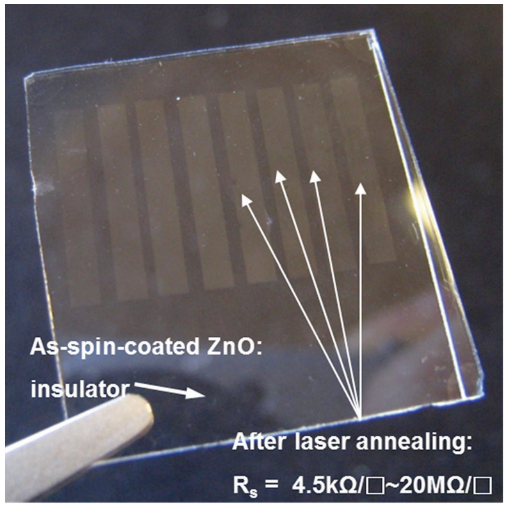

Figure 3.2 Photoimage of the ZnO thin film on a quartz substrate after laser annealing. Huge reduction of sheet resistance at annealed part is observed. Surface morphology change of the ZnO thin film after laser annealing is also observed.

Many research reports attributed the residual conductivity of undoped ZnO film to intrinsic defects such as oxygen vacancies and interstitial zinc atoms, [100, 117, 118] although the exact mechanism still remains as a matter of discussion. To investigate the effect of oxygen in ambient air condition, additional experiments were conducted in different background gases. Argon or argon-air mixture was introduced to a quartz enclosure during laser annealing as illustrated in **Figure 3.6a**. The argon flow rate was

maintained at about 8000 mL·min^{-1} while the air flow rate was varied from 0 to 200 mL·min^{-1} to optimize the resistivity and transparency of the annealed films. Laser power and scan speed were fixed at 63.8 kW·cm^{-2} and 10 mm·s^{-1} respectively. **Figure 3.6b** shows the effect of background gas composition on sheet resistance. The sheet resistance was lowest when the background gas was only argon and increased at air flow rates over 100 mL· min^{-1}. When the air flow rate was 50 mL· min^{-1} or less, resistance increase was minimal, compared with annealing in only argon gas. The drawback of laser annealing in the argon gas is the film transparency reduction. As shown in **Figure 3.7a**, when the film was annealed only in the argon gas, the transmittance of the film was 63 % ~ 74 % at the 500 nm ~ 700 nm wavelength range and about 17 % ~ 21 % lower compared with the 84 % ~ 91 % transmittance of the thin film annealed at ambient air condition over the same spectral range. As air was mixed with argon gas, the film transmittance became higher. When the air flow exceeded 50 mL· min^{-1}, the transmittance became comparable to the thin film annealed without argon flow. Therefore, the combined 50 mL· min^{-1} air and 8000 mL· min^{-1} argon background gas flows can assist the formation of a highly conductive thin film while maintaining high transparency.

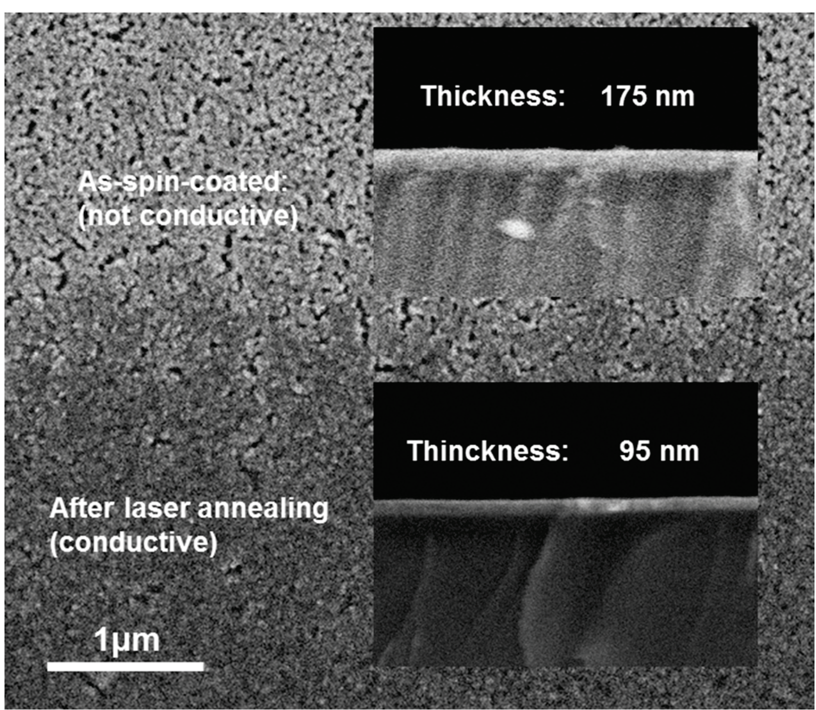

Figure 3.3 SEM image at the boundary of the laser-annealed surface on a quartz substrate

The effect of laser annealing and background gas on the conductivity and transparency of the thin film can be explained as follows. The conductivity of the undoped ZnO thin film is attributed to the intrinsic defects such as oxygen vacancies (V_O) and interstitial zinc

atoms (Z_{in}). It is apparent that as the oxygen vacancies increase in the ZnO film, the film becomes less transparent since it becomes more metallic. During laser annealing at ambient conditions, oxygen vacancies increase since very short (picosecond) laser pulses heat up the thin film surface to a temperature high enough to break Zn-O bonds and form oxygen vacancies [100, 117]. Besides thermal stimulation, photon energy (~3.5 eV for 355 nm wavelength) exceeding the bandgap of ZnO (~3.3 eV) may directly excite adsorbed oxygen and thus promote its dissociation. Since the pulse repetition rate is high (80 MHz), heat is accumulated establishing a quasi-static temperature distribution, bearing the superposed short-lived transients induced by the individual pulses. The ZnO film cooling rate strongly depends on the thermal properties of the underlying substrate. Conductive heat transfer calculations showed that the amplitude of the picosecond temperature spikes matched the quasi-static temperature level in the case of the thermally insulating glass substrate. The argument that high surface temperature is the main contributor to the formation of oxygen vacancies was confirmed *via* another experimental result. When the film was deposited on a silicon wafer that has much higher thermal conductivity and thermal diffusivity, substantially higher power was needed to make the deposited ZnO film conductive. Along with the oxygen vacancy increase, if the laser annealing is done at ambient condition, oxygen supply from the surrounding air oxidizes ZnO [119]. Since the vacancy increase rate is faster than the oxidation rate, one may expect a net increase of oxygen vacancies, raising the conductivity of the ZnO film. On the other hand, when the surrounding gas is argon, there is no oxidization process due to the lack of oxygen and the net increase of oxygen vacancies is much higher, hence producing more conductive ZnO. To support this, a ZnO thin film once annealed under argon gas flow was re-annealed at ambient condition. **Figure 3.7b** presents a cross-shaped re-annealed part (A) of the ZnO film annealed in the argon environment (B). The re-annealed part became more transparent and less conductive because of re-oxidation. This finding is consistent with the previous explanation.

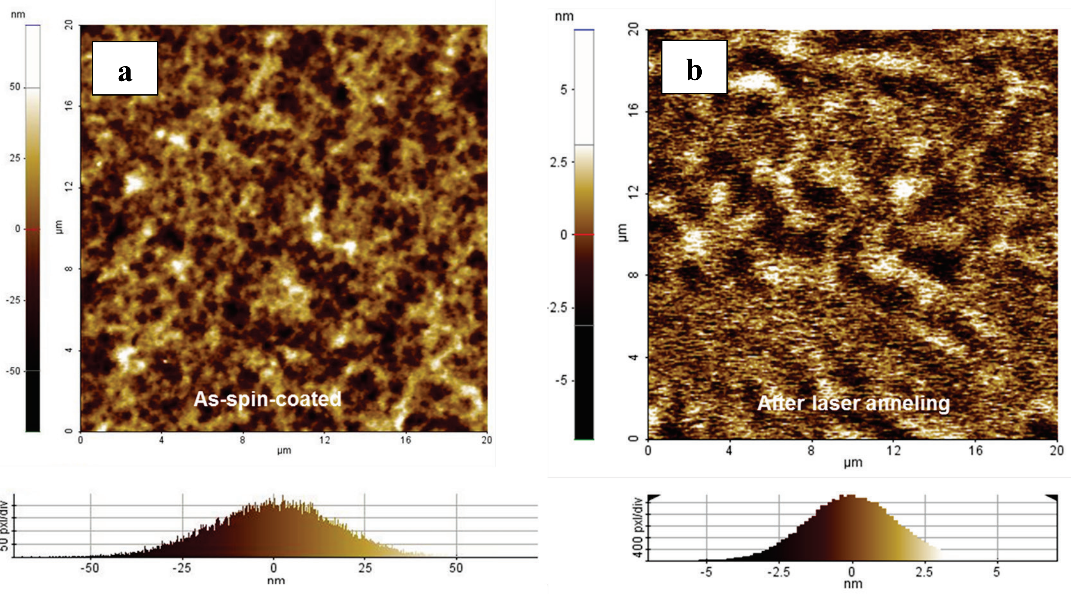

Figure 3.4 Comparison of AFM images of (a) as-coated and (b) laser-annealed surfaces. RMS roughness of 1.7 nm after laser annealing

The best sheet resistance of the ZnO thin film with optical transmittance greater than 84 % ~ 88 % in the 500 nm ~ 700 nm wavelength range was around 5 kΩ/□ after annealing in the argon and air background gas mixture. Considering the film thickness of 95 nm, the film resistivity is 4.75×10^{-2} Ω·cm. Annealing at ambient condition yielded sheet resistance and film resistivity of 30 kΩ/□ and 2.85×10^{-1} Ω·cm, respectively, with the transmittance staying the same. The resistivity of 4.75×10^{-2} Ω·cm is even comparable to that of vacuum-deposited, impurity-doped ZnO films, [102] within a factor of 10.

It is worth emphasizing that laser annealing enables selective patterning directly on the thin film without any photolithographic process since the properties of only laser annealed parts are altered. Furthermore, since laser annealing does not require a vacuum environment, it can be configured in conjunction with a high-throughput roll-to-roll process. **Figure 3.8a** illustrates LDW patterns through an objective lens on the ZnO thin film on 3 cm × 3 cm soda-lime glass. Arbitrary patterns of 1.5 µm line width were printed from a tightly focused laser beam (**Figure 3.8b**).

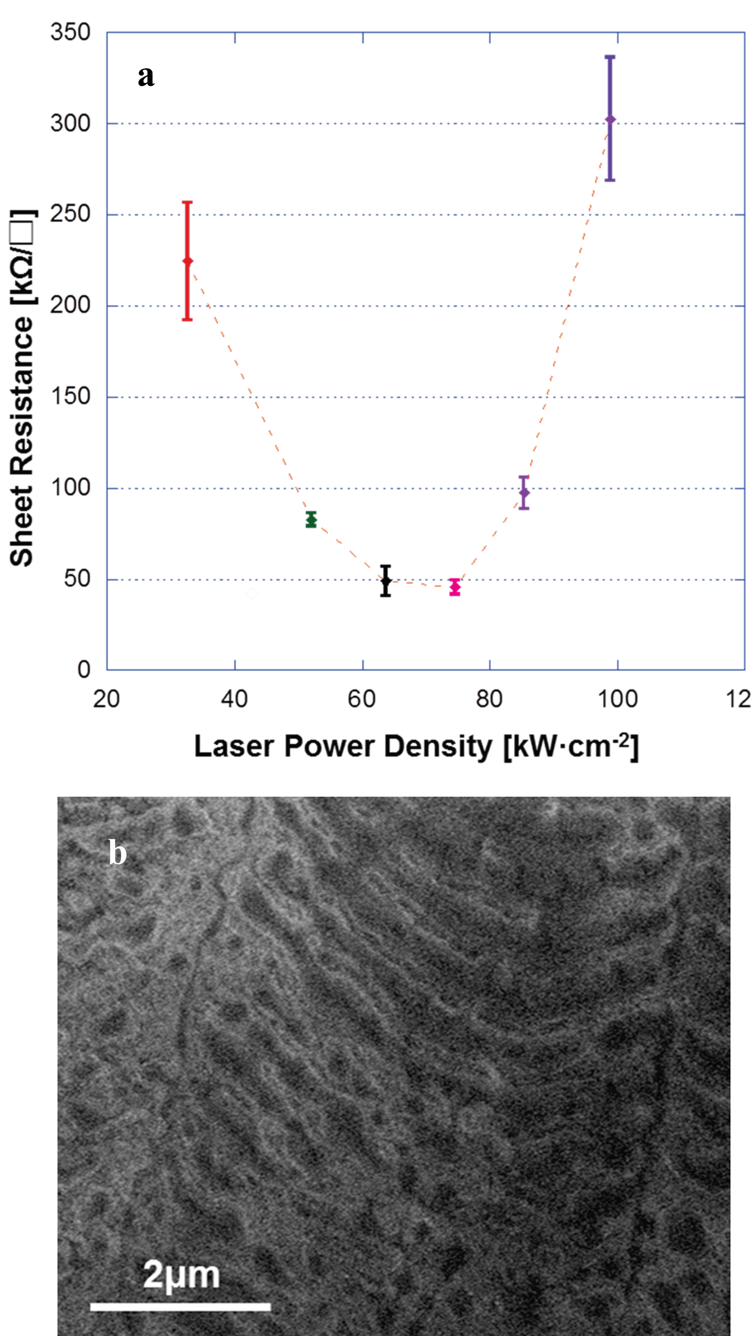

Figure 3.5 (a) Sheet resistance (R_s) of the laser annealed ZnO thin film corresponding to laser power; (b) SEM image of the degraded ZnO film on a quartz substrate due to excessive laser power

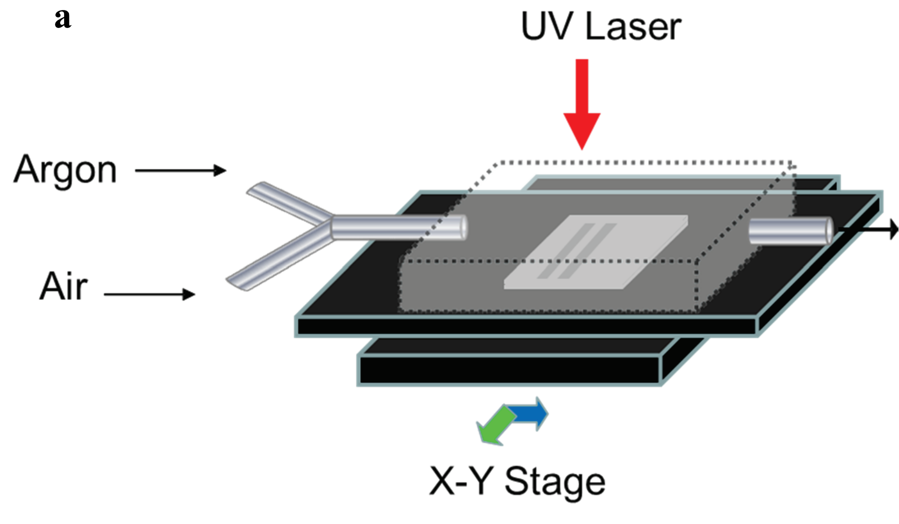

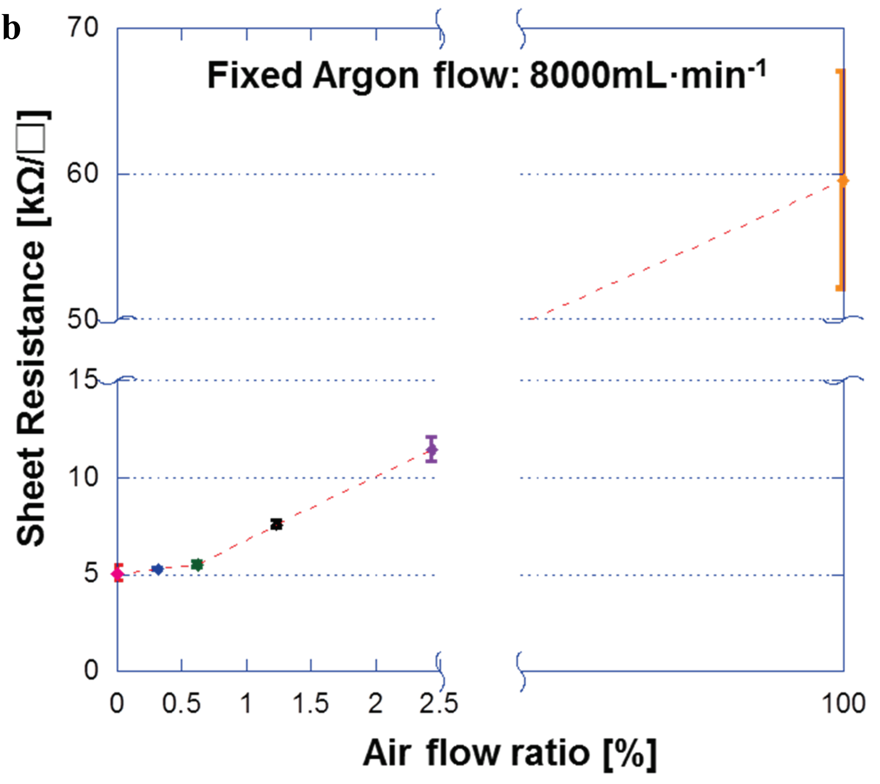

Figure 3.6 (a) Quartz enclosure for argon-air mixture flow; (b) R_s corresponding to the background gas

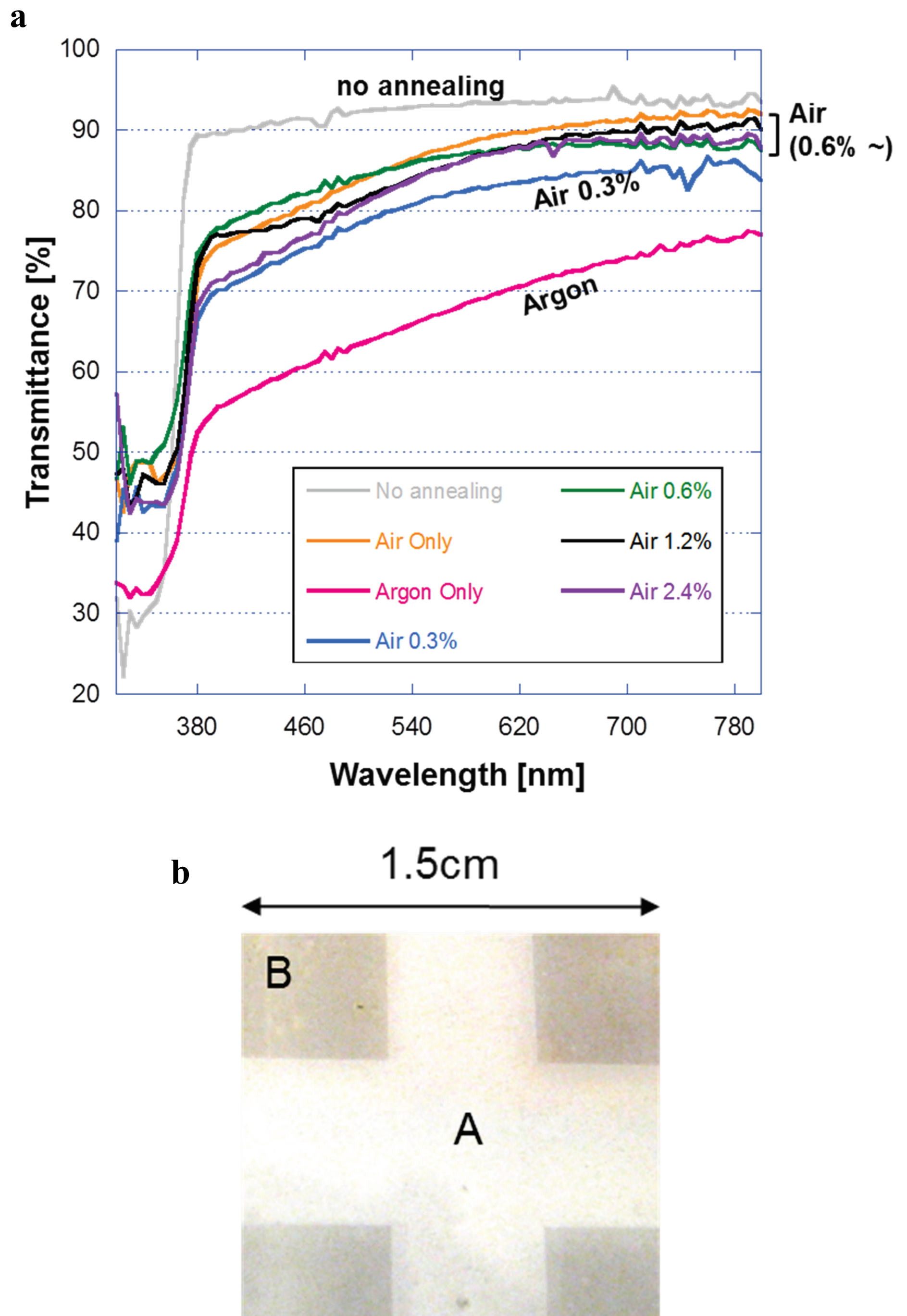

Figure 3.7 (a) Optical transmittance of the ZnO thin films annealed in various background gas compositions; (b) restored transparency of the re-annealed area in the air (A) from an annealed film on a quartz substrate in the argon environment (B).

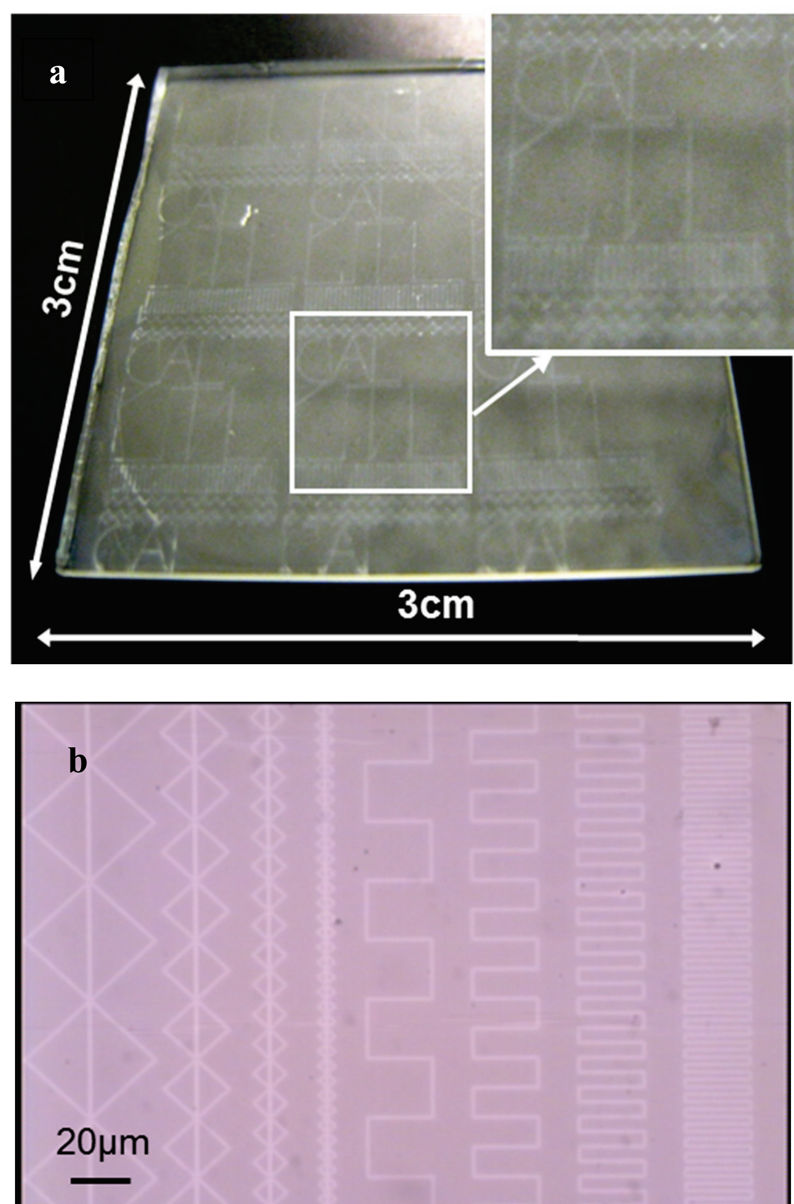

Figure 3.8 LDW of the ZnO thin film on a soda-lime glass. (a) Photograph of arbitrary patterns on the 3 cm by 3 cm area; (b) optical microscope image of 1.5 μm line-width patterns.

3.5 Device fabrication and testing

The process developed in this work to deposit a highly conductive ZnO film has been applied to the fabrication of a TFT device. To make a ZnO TFT, ZnO NP solution was spin coated on pre-patterned metal electrodes on a SiO_2 (250 nm thickness) /Si (n+, 0.005 Ω·cm, 525 μm thickness) substrate followed by laser annealing. The ZnO TFT has a typical bottom gate / bottom contact transistor configuration with a highly doped n-type (arsenic) silicon wafer as the back gate and a SiO_2 layer as the gate dielectric. For metal electrodes, a 30 nm chromium layer was created followed by a 100 nm gold layer by thermal evaporation to provide the gold adhesion to the SiO_2 layer. Source and drain electrodes were defined by a standard lift-off technique. The channel length (L) was 2 μm and the channel width (W) was 160 μm. The laser annealing setup and condition were the same as described in **Figure 3.1**, except for the laser power. With a 25 μm Gaussian beam through a single convex lens (50 mm focal length), the ZnO layer was annealed with overlapping lines at 10 μm pitch at ambient conditions. The applied laser power was 344 $kW \cdot cm^{-2}$. To compare the performance of the laser annealed ZnO TFT with the thermally annealed one, identical ZnO TFT was thermally annealed in air at 300 °C for 1.5 h.

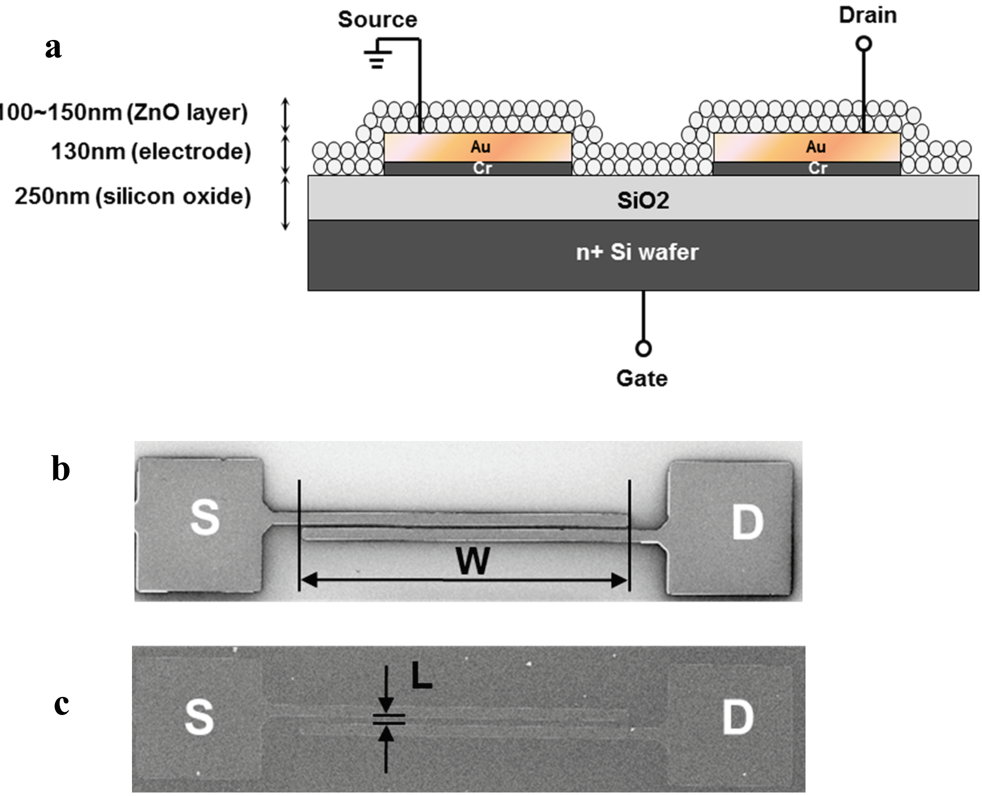

Figure 3.9 (a) The schematic cross-sectional view of the ZnO thin-film field-effect transistor (ZnO TFT). Cr-Au electrodes were defined by a standard lift-off process on a highly doped n-type silicon wafer with oxide as gate dielectric. ZnO NPs were spin coated on top; (b), (c) top-view SEM images of the ZnO TFT electrodes without and with a ZnO active layer respectively. 'S' and 'D' indicates source and drain electrodes respectively. Channel width (W) / channel length (L) is 160 μm / 12 μm.

Figure 3.9a displays the schematic side view of the ZnO TFT architecture for this demonstration, which has a typical bottom gate/bottom contact transistor configuration. The SEM image in **Figures 3.9(b,c)** depict top views of transistor electrodes without and with a spin-coated ZnO NP active layer, respectively. The laser-annealed ZnO TFT characteristics were measured utilizing an HP 4155A semiconductor parameter analyzer in a dark Faraday cage at room temperature. **Figures 3.10(a,b)** show output and transfer characteristics indicating n-channel behavior in accumulation mode on a positive gate bias. The channel width and length were 160 μm and 2 μm, respectively. For a source-drain current (I_{ds}) versus source-drain voltage (V_{ds}) plot, V_{ds} was swept from 0 V to 1.2 V while the gate voltage (V_{gs}) was fixed at -15 V, 0 V, 15 V and 30 V. As detected in the previous research [54], increase of V_{ds} resulted in the decrease of threshold voltage (V_t) and punch-through was observed at higher V_{ds}. Likewise, device operation shown here is only in the linear regime. For the I_{ds}-V_{gs} plot,

V_{gs} was scanned from -15 V to 30 V while I_{ds} was varied from 0 V to 1.2 V with 0.3 V step respectively.

The effective electron mobility (μ) was calculated according to the relationship for the continuous thin film [54]:

$$\mu = \frac{L g_m}{W C_{ox} V_{ds}} \quad (3.1)$$

$$g_m = \left. \frac{dI_{ds}}{dV_g} \right|_{V_{ds}} \quad (3.2)$$

where L, g_m, W, C_{ox}, and V_{ds} indicate the channel length, transconductance, channel width, capacitance of the silicon oxide and source-drain voltage, respectively. The transconductance, 4.9795 μS, was extracted by linear fitting of the I_d-V_g plot from 10 V to 30 V. The calculated effective electron mobility (μ) is 3.01 $cm^{2}V^{-1}s^{-1}$ at V_{ds}=1.2 V. This mobility value is over an order of magnitude higher than previously reported values (0.1~0.2 $cm^2V^{-1}s^{-1}$) for solution-deposited followed by thermally annealed at higher temperature (~700 °C) ZnO TFT [103] or an excimer laser annealed ZnO TFT of previous work [54]. The fitted threshold voltage is 7.46 V. From a semilog I_{ds}-V_{gs} plot at V_{ds}=1.2 V, an on/off current ratio is as large as 10^5 and a sub-threshold slope is 1.8 V/decade. A TFT of the same structure and with a thermally annealed (300 °C, 1.5 h) ZnO active layer has low mobility (0.0130 $cm^2V^{-1}s^{-1}$) and low on/off ratio (10^2), as included in **Figure 3.10b.** These performance graphs enable comparison between two different annealing methods revealing the superiority of laser annealing to thermal annealing.

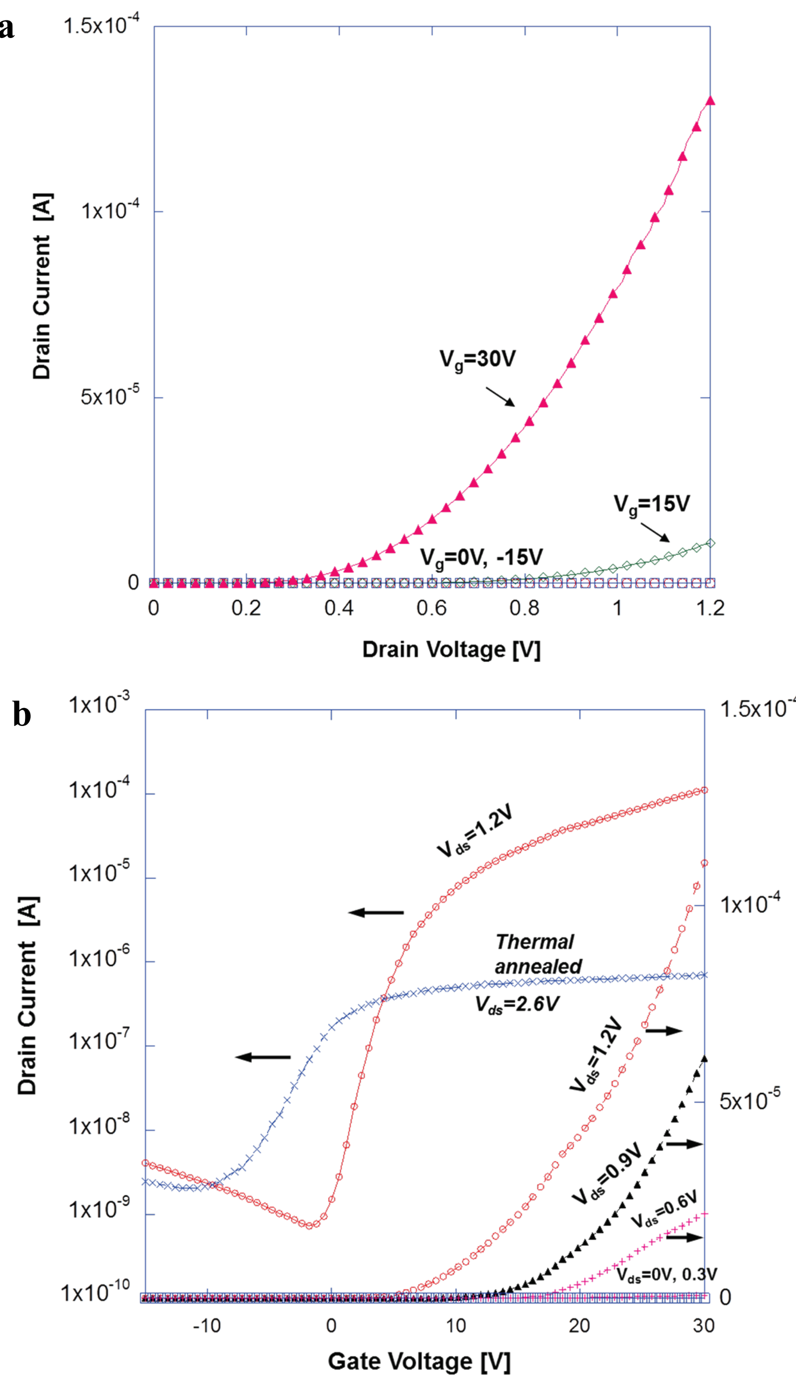

Figure 3.10 (a) Plot of drain source-current (I_{ds}) versus source-drain voltage (V_{ds}) as a function of gate voltage (V_g); (b) Log-linear (with the left y-axis) and linear-linear (with the right y-axis) plot of I_{ds} versus V_g. * The blue cross-marked line indicates I_d-V_g plot of a thermally annealed TFT at 300 °C for 1.5 h.

Replacing the quartz substrate by a silicon (or silicon bearing a thin oxide layer) wafer requires much higher (about 10 times) laser power to reach the same resistivity as achieved on the quartz substrate. Recalling fundamental diffusive heat transfer trends upon transient heat flux input, the induced temperature scales approximately with the parameter $\alpha^{0.5}k^{-1}$, where α and k are the thermal diffusivity and conductivity, respectively [120]. As shown in **Table 3.1**, the thermal diffusivity and conductivity of the silicon wafer are both about 100 times higher than those of quartz [120]. Neglecting the thin oxide layer, 10 times higher heat input would be needed to reach the same temperature for a film on a silicon wafer than on quartz. This estimate is in fact in good agreement with the experimental results. A laser power of 410 $kW \cdot cm^{-2}$ was needed to achieve a resistance of 80 kΩ on the silicon substrate, indeed almost 10 times higher than the required laser power input on quartz to obtain the same resistance. Since the laser power for fabricating the TFT was 344 $kW \cdot cm^{-2}$, as described in section 3.4, it is inferred that semiconducting behavior was retrieved with relatively higher resistivity.

Table 3.1. Thermal properties of quartz and silicon substrates

	Thermal conductivity, k [$Wm^{-1}K^{-1}$] (at 300K)	Thermal diffusivity, α [m^2s^{-1}] (at 300~1000K)
Quartz	1.3	$7\sim8\times10^{-7}$
Silicon	149	$2\sim6\times10^{-5}$

3.6 Conclusion

In summary, a solution-processible, high-concentration transparent ZnO NP solution was successfully made in a new process. A highly transparent ZnO thin film was made using this suspension by spin coating without involving either vacuum deposition or a high-temperature process. The laser annealing process combined with solution-based ZnO NPs offers functional versatility and tunability of electrical and physical properties over a wide range. Laser radiation enables selective annealing directly on the thin film. Since only the annealed area showed high conductivity, conductive patterns could be constructed without relying on a photolithographic process. ZnO thin film conductivity and transmittance variations were examined by altering the annealing parameters such as laser power, scanning speed and background gas. The lowest resistivity of the undoped spin-coated ZnO film after laser annealing was about 4.75×10^{-2} $\Omega \cdot cm$, which is comparable to furnace-annealed ITO films and lower by a factor of 10^5 than that of furnace-annealed ZnO films. A ZnO TFT performance test reveals that by just changing the laser parameters, the ZnO thin film can also perform as an n-type semiconductor

active layer with the mobility of 3.01 $cm^{2} \cdot V^{-1}s^{-1}$ and the on/off ration of 10^5. The latter finding suggests that laser annealed ZnO films can be used as transparent electronic devices.

Chapter 4

Large area nanoimprinting of NPs enabled by high speed laser direct writing

As a method for the deposition and patterning of nanomaterials, laser-assisted, one-step direct nanoimprinting of metal and semiconductor NPs was investigated. LDW was adapted for high-speed (200 $mm \cdot s^{-1}$) mold fabrication process with negative and positive photoresists. Polydimethylsiloxane (PDMS) stamps fabricated from master molds replicated nanoscale nanomaterial structures such as mesh, line, nanopillar and NW arrays with no or negligible residual layers on various substrates. The process was completely free of lift-off or RIE processes. The low temperature and pressure used for nanoimprinting enables direct nanofabrication on flexible substrates. Wafer scale 4-inch direct nanoimprinting was demonstrated.

4.1 Introduction

Nanoimprinting lithography (NIL), a method through which stamp patterns are replicated into a material on a substrate by mechanical contact and 3D material displacement [121], is a potential candidate for next generation lithography because of its low cost, high throughput and high resolution. NIL allows the fabrication of different structures at submicron resolutions as well as patterning of functional materials. Printing metal or semiconductor films at the submicron level is critical for the fabrication of optoelectronics, organic electronics, and biophotonic/nanophotonic devices.

Conventional NIL methods have been documented in great detail so far, including comprehensive review papers [121-124]. A hard mold containing nanostructures is pressed into a liquid or heated polymer material that had previously been dispensed or spun on a hard substrate, possibly a silicon wafer with a thin silicon

oxide layer. Such mold pressing is typically done under controlled high temperature and high pressure. After the mold is released, polymer nanostructures remain on the surface of the substrate. A residual layer is then removed, typically by reactive ion etching (RIE), to complete pattern definition on the underlying substrate. Master mold fabrication is a critical issue in the development of a high throughput and low cost NIL system. The conventional master mold fabrication processing steps are as follows: 1) a resist material spin-coated on the mold surface, mostly Si or Si/SiO_2 substrate, is patterned by photolithography steps; 2) a metal is vacuum deposited over the patterned resist followed by a lift-off process producing a patterned mask layer on the substrate; 3) RIE process selectively etches away the uncovered mold surface to leave patterned structure for NIL; 4) the metal layer is removed. The most common lithography method involved in the mold fabrication step for nanoscale patterns is electron beam lithography (EBL) [70, 71, 125, 126]. EBL, while being able to produce nanoscale feature sizes, is a technique that is hard to scale up, has a low throughput, and requires fairly expensive vacuum environment equipment. Furthermore, large area format and roll-to-roll manufacturing applications for large area photovoltaics and displays are not conducive to EBL because of the obvious economic and physical geometric limitations.

Fabrication of low cost nanoscale molds has been achieved using nanosphere lithography [127-129]. Well-ordered two dimensional structures have been obtained on silicon wafers. Although these molds were produced relatively inexpensively, lift-off and RIE complicate the fabrication and prove incompatible with mass production and large-scale applications. Also patterned structures are mainly constricted to dot arrays. Extreme Ultra-Violet Interference Lithography (EUV-IL) [130-132] is another mold fabrication technique used with NIL, although it is also hampered by lift-off and multiple etching steps. The specialized EUV-IL light source and optics components present additional obstacles to further cost reduction and the method is limited to array patterns without extra lithography techniques. Another potential mold fabrication technique to replace EBL is Scanning Probe Lithography (SPL) [83, 84, 133, 134]. This method, while providing small features requires the use of an atomic force microscope (AFM) and could be difficult to handle large area systems where high throughput operation is required. Direct imprinting of gold structures has been successfully accomplished using NPs in organic solution, and therefore excluding RIE and lift-off steps [57, 85, 86, 135]. However, the master mold fabrication for submicron features was done by EBL which is subject to the above mentioned limitations.

Here a novel master mold fabrication method is reported. The method is used in conjunction with nanoimprinting of various NPs, such as ZnO, Ag and Si NPs that can be used in mass production. Nanoimprinting master molds have been fabricated using a LDW process, which in turn can be used to replicate polydimethylsiloxane (PDMS) stamps. Using these stamps, a simple and versatile direct nanoimprinting method has been realized that can produce NP patterns with line width down to ~200 nm, whereby 4 inch wafer scale nanopatterning was achieved. In short, this method combines advantages of LDW and nanoimprinting as well as large area and submicron patterning.

4.2 Experimental setup

Figure 4.1a depicts a schematic illustration of the procedure implemented for one-step direct nanoimprinting of metal and semiconductor NPs, including the fabrication of the master molds and stamps. Negative photoresists, SU-8 2000.5 and SU-8 2002 and a positive photoresist, OiR 700-10 was spun on a silicon substrate in preparation for two-dimensional laser lithography. A silicon wafer (525 μm thickness) was cleaned with piranha solution followed by dehydrating the wafer in an oven for 20 min at 120°C. HMDS surface treatment was applied for OiR 700-10 photoresists (Fuji Film) to promote adhesion between the photoresist and the substrate. SU-8 2002 and SU-8 2000.5 (Microchem) photoresist were spun at 5000 rpm and 3000 rpm to yield thicknesses of 1.7 μm and 500 nm respectively. OiR 700-10 photoresist was spun at 6000 rpm to obtain 900 nm thickness. By using the setup shown in **Figure 4.1b**, a LDW method was applied to create the master molds. For LDW process, an Yttrium Vanadate ($Nd:YVO_4$) ps UV laser (Newport, wavelength: 355 nm, pulse width (FWHM(full width at half maximum)): 12 ps, repetition rate: 80 MHz) was used to expose the photoresist through a 39X objective lens (N.A.=0.5) and a high resolution mechanical stage was utilized for xyz control. A Gaussian beam profile of 1.56 μm ($1/e^2$) diameter was obtained through the focus of the objective lens. The details of the beam profile are shown in the following section. To adjust exposure energy, scan speed was fixed at 200 $mm \cdot s^{-1}$ and laser power density was varied from 3.9 $kW \cdot cm^{-2}$ to 23 $kW \cdot cm^{-2}$. For SU-8 photoresist, after the photoresist was exposed to UV laser irradiation, a 2 min post exposure bake (PEB) at 95 °C was performed followed by a 1 min stripping of the non-exposed portion of the wafer with SU-8 developer (Microchem) and a 30 sec cleaning with isopropyl alcohol (IPA). A 30 min hard bake step at 200 °C was subsequently added to enhance the mechanical properties. For OiR 700-10 photoresists, UV exposed photoresist was developed in a OPD 4262 (Fuji Film) developer for 1 min, subsequently a 30 min hard bake at 120 °C was applied. This novel method eliminates the need for intermediate steps such as reactive ion etching (RIE) or lift-off processes. It also allows for scale-up and large area processes that are needed for mass production, finally providing an inexpensive and large scale solution compared with EBL, while offering submicron resolution.

PDMS was poured on the master mold and degased, followed by curing for 1 hour at 70 ˚C. Careful detachment of the PDMS from the master mold resulted in about a 5 mm thick soft stamp bearing submicron patterns. The master mold could be used repeatedly without any deformation. These PDMS stamps were utilized in a nanoimprinting process to pattern metal and semiconductor NP solutions.

Three kinds of NP solutions were used for imprinting materials, Ag NPs in ethanol (~25 nm, 14 wt%), Si NPs in water based solution (~5 nm, 0.16 wt%) and ZnO NPs in 1-pentanol (~6 nm, 2 wt% ~ 15 wt%). Ag and ZnO NP solutions were in-house made and silicon NP (Meliorum Technologies, Inc.) solutions are commercially available.

The details of ZnO NP synthesis has been described in section 2.1. Ag NPs were synthesized from the polyol process [73]. Silver nitrite (AgNO3) was dissolved in de-ionized water to make a 67 wt% solution as a precursor of Ag. As a reduction agent, 1 wt% polyvinlpyrrolidone (PVP, Mw=10K) was dissolved in ethylene glycol ($C_2H_6O_2$). In

a typical process, 100 mL of the reduction agent was heated and kept at 100 °C followed by injection of a 5ml silver nitrate solution into the solution with vigorous stirring. The color of the mixture quickly turned into yellow, amber, ruby and finally green, suggesting the growth of silver particles. For silver NPs with a mean size of around 25 nm, the reaction was maintained for 30 min. After completing the reaction, the mixture was washed with acetone and then the silver NPs were recovered by centrifuging at 3000 rpm for 30 min.

After depositing the NP solution on the substrate (silicon, silicon/silica, glass, polycarbonate film), the PDMS stamp was pressed into the NP solution under low pressure conditions (7.5 kPa ~ 18 kPa) while heated by a hot plate. The temperature during this step is kept lower than the solvent boiling point, which is 60 °C, 90 °C, 120 °C for ethanol, water and 1-pentanol respectively. Temperatures exceeding the solvent boiling temperature induce bubbles at the interface of PDMS and NP solution, resulting in irregular imprinted patterns while too low temperature prolongs the imprinting time. With selected optimized temperature for each NP solution, imprinting time was usually between several tens of second and several minutes. Once the solvent was evaporated thoroughly through the PDMS stamp, the stamp was detached. No special surface treatment was needed for these procedures since the NP solution does not stick to the PDMS stamp that in turn is moderately adhering to the various substrates utilized.

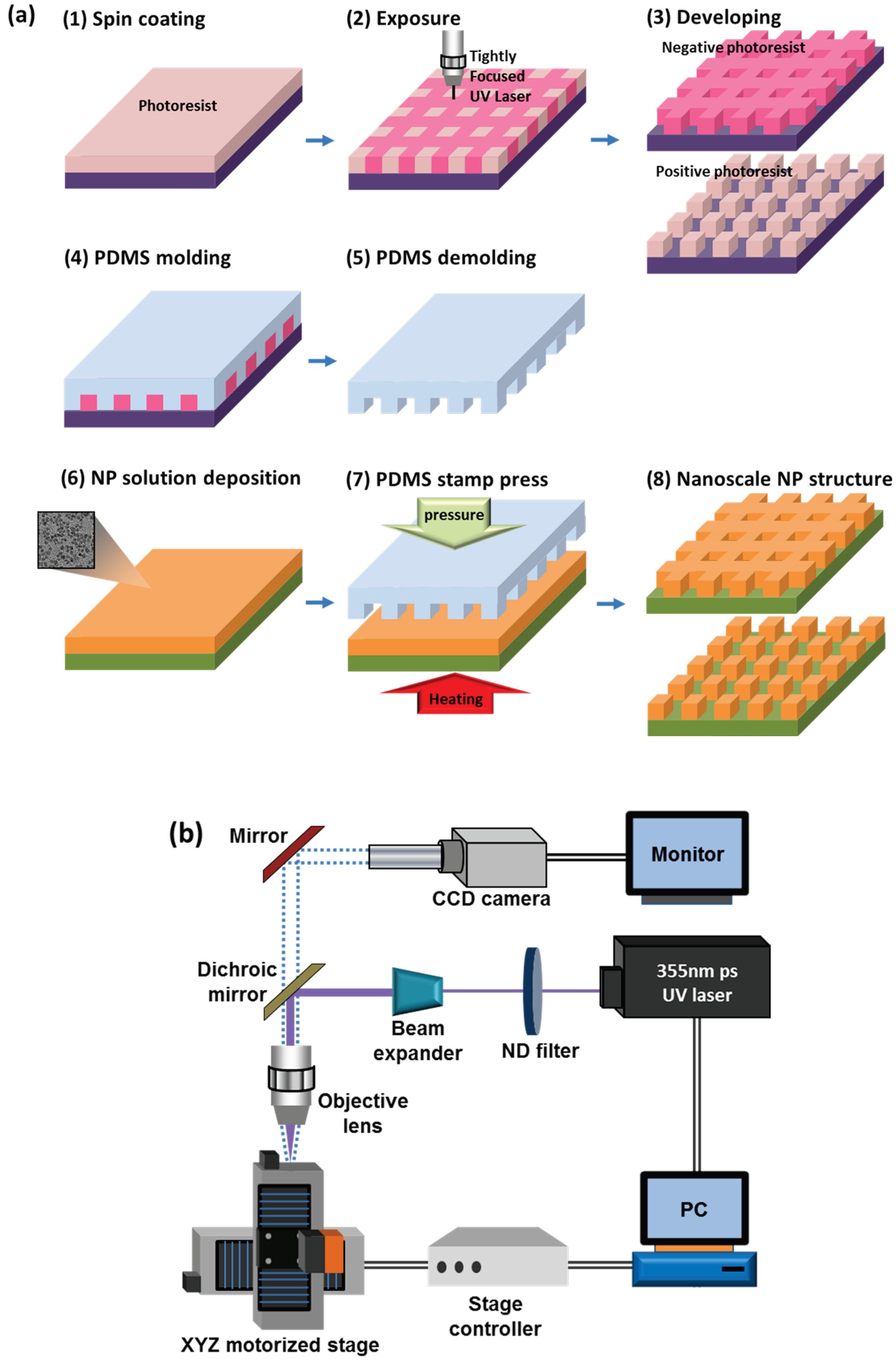

Figure 4.1 (a) Schematic illustration of the laser assisted nanoparticle nanoimprinting lithography process; (b) schematic diagram of the experiment setup

4.2.1 Fine alignment procedures for large area LDW

For the large area, tightly-focused LDW process, fine alignment of the laser system is required. The alignment procedure is as follows. First, the beam path, before installing the objective lens, should be vertical to the x-y stage (**Figure 4.2a**). Even if the x-y stage is not perfectly parallel with the optical table, since a target or substrate moves with the x-y stage, the reference surface should be on the x-y stage rather than the optical table. The verticality can be checked from the coincidence between the incident and reflected beam path after placing a reflecting material with high degree of flatness such as a Si wafer on the stage. An iris diaphragm or pinhole on a flat paper is useful for checking the coincidence. Both the incident and the reflected beam should pass through the center of the iris diaphragm or pinhole. Second, the objective lens is installed so that the beam path is not interrupted by the lens (**Figure 4.2b**). This confirms that the incident laser beam passes through the center of objective which is crucial for delivering the best performance of the objective lens. A temporary plane needs to be placed between the x-y stage and the objective lens to check the beam path through the objective lens since the beam diverges quickly downstream of the focal point defined by the objective lens. Once the objective lens is installed, the components arranged from the laser to the objective lens should be kept intact. Third, a z-axis stage and a tilt stage is installed (**Figure 4.2c**). The z-axis stage is installed to adjust the working distance between objective lens and substrates whose thickness may vary. The tilt stage enables the working distance to be maintained over the entire substrate (**Figure 4.2d**). The tilt stage is indispensable for large area processing since a sample or substrate with an uneven surface easily loses the focal point even assuming that the top surface of the tilt stage and the focal plane of the objective lens are perfectly parallel each other.

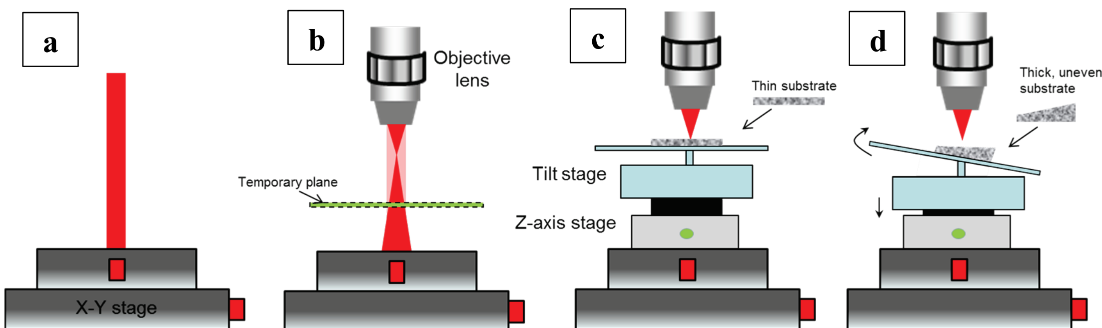

Figure 4.2 Fine alignment procedures for the laser direct writing setup. (a) The beam path, before installing the objective lens, should be vertical to the x-y stage; (b) the objective lens is installed in order that the beam path is not interrupted; (c) a z-axis stage and a tilt stage is installed; (d) the z-axis stage and the tilt stage maintain the focal plane on various thickness substrates.

4.2.2 Laser beam characterization

The intensity profile of the picosecond laser beam was obtained by knife-edge measurement method [136, 137]. The intensity profile measured as a knife-edge passes through the beam by a motorized stage is fitted assuming the intensity follows the Gaussian distribution. **Figures 4.3** and **4.4** show the measured laser power at the focal plane and the fitted Gaussian beam profile, respectively. Fitted Gaussian distribution equation is as follows.

$$I = Ae^{-\frac{(x-B)^2}{2C^2}} = 41.19e^{-\frac{(x-1.2)^2}{2\times 0.3889^2}} \tag{4.1}$$

Thus, $1/e^2$ beam diameter is calculated from above equation as $4 \times C = 1.56$ µm. **Figure 4.5** depicts beam diameter ($1/e^2$) divergence as a function of the axial distance.

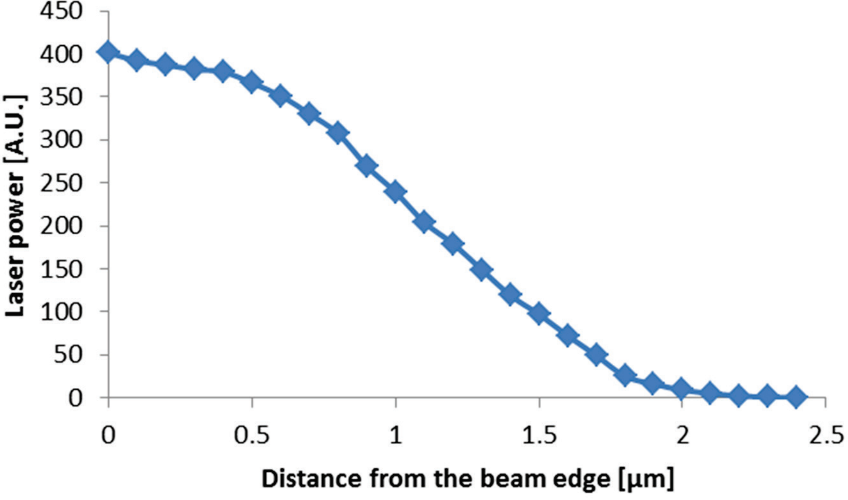

Figure 4.3 Measured intensity at the focal plane

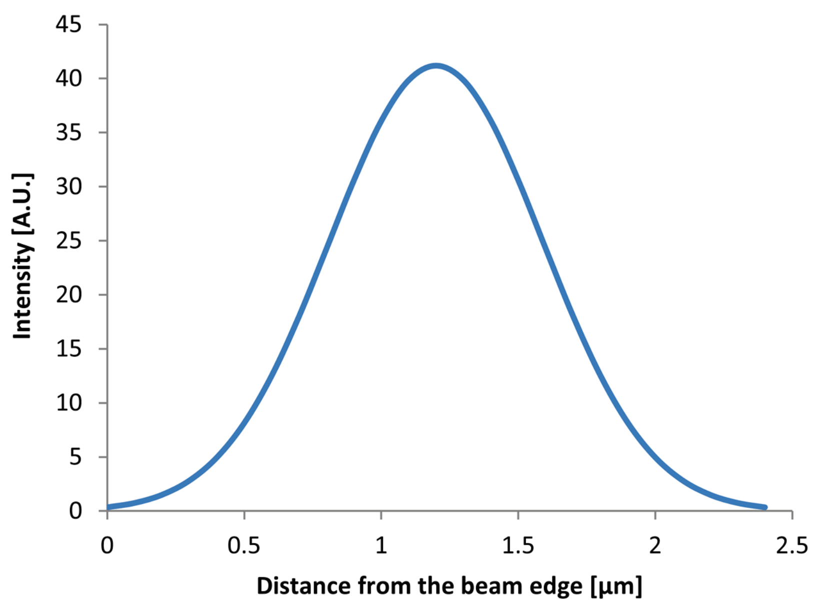

Figure 4.4 Fitted Gaussian beam profile at the focal plane

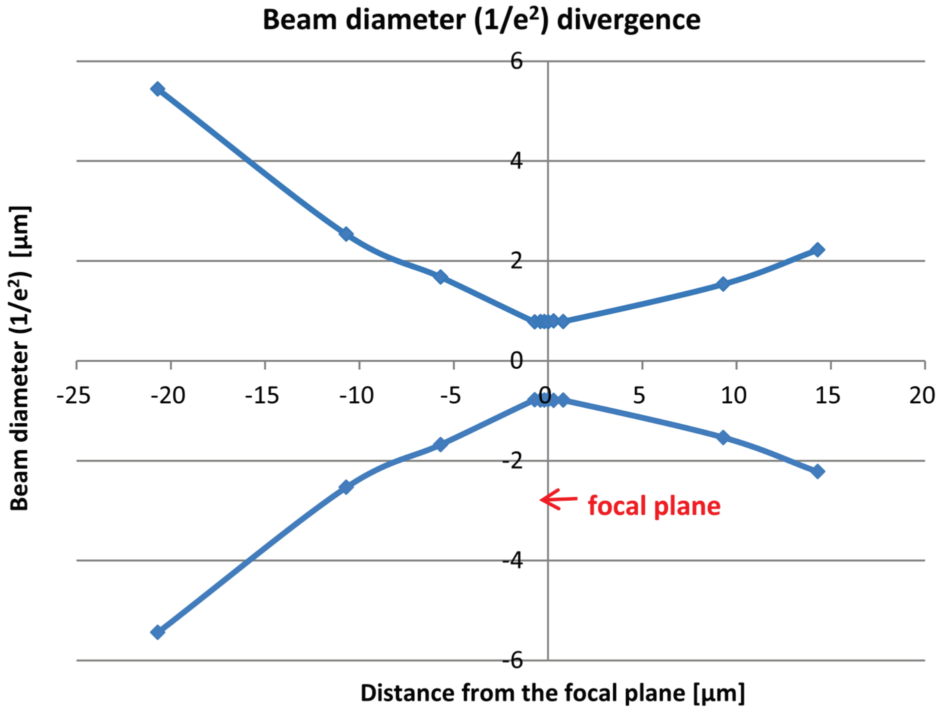

Figure 4.5 Gaussian beam width as a function of the axial distance

4.3 LDW of SU-8 photoresist to generate positive line patterns

The line width of the SU-8 photoresist, which is highly sensitive to laser light exposure is a function of both laser power and scan speed. Increase of the laser power or decrease of the scan speed induce line width increase. To identify the condition of fastest writing and smallest features, the scan speed was fixed at near the maximum speed of the mechanical stage and laser power was varied. **Figure 4.6a** shows the line width change with the laser power at a 200 $mm \cdot s^{-1}$ scan speed. Not fully cross-linked SU-8 that was exposed to insufficient laser energy resulted in meandering patterns or detachment of photoresist after developing (**Figure 4.6a** insets). No pattern was left when the photoresist was exposed below a certain threshold laser power. Under an optimized laser power for smallest line width and stable features, submicron patterns could be obtained. **Figure 4.6b** displays photoresist patterns on a silicon wafer that were used as master molds and a PDMS stamp fabricated from the master molds. SU-8 2000.5 nanogratings have an 840 nm line width, a 3.5 μm pitch and a 500 nm height while SU-8 2002 patterns have a 950 nm line width, a 4 μm pitch and a 1.7 μm height. Without any surface treatment, PDMS could be demolded, leaving no residuals behind. The remaining line patterns on the SU-8 master mold were transferred as line grooves on the PDMS stamp producing the final NP line patterns. It is noted that the PDMS stamp could be used repeatedly. **Figure 4.7** shows mesh or line patterns of Ag (**4.7a**), Si (**4.7b**) and ZnO (**4.7c**) NPs imprinted on glass or Si/SiO_2 substrates with a PDMS stamp from SU-8 2002 master mold. The line widths of imprinted NP patterns were 790 nm, 580 nm and 300 nm for Ag, Si and ZnO NPs respectively. These are smaller than the feature size of the master mold. This is attributed to the shrinkage of the NP solution volume when the solvent evaporates. The final line width, therefore, depends on different properties of NP solutions such as NP concentration, viscosity and evaporation temperature.

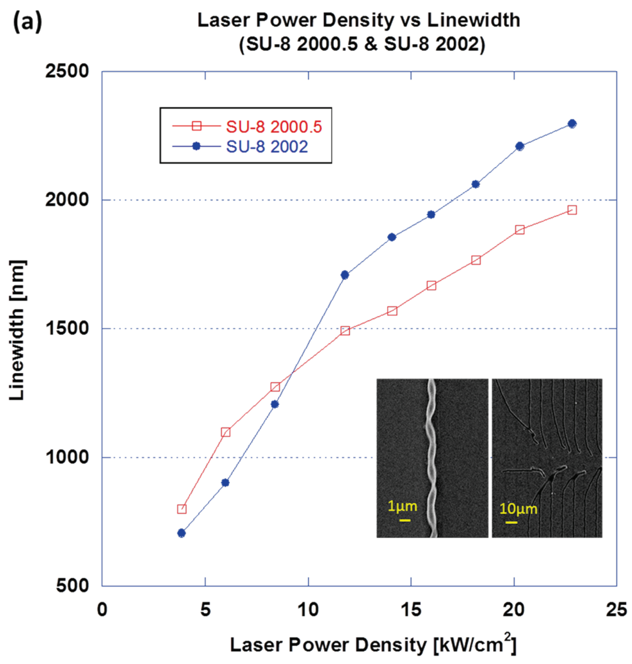

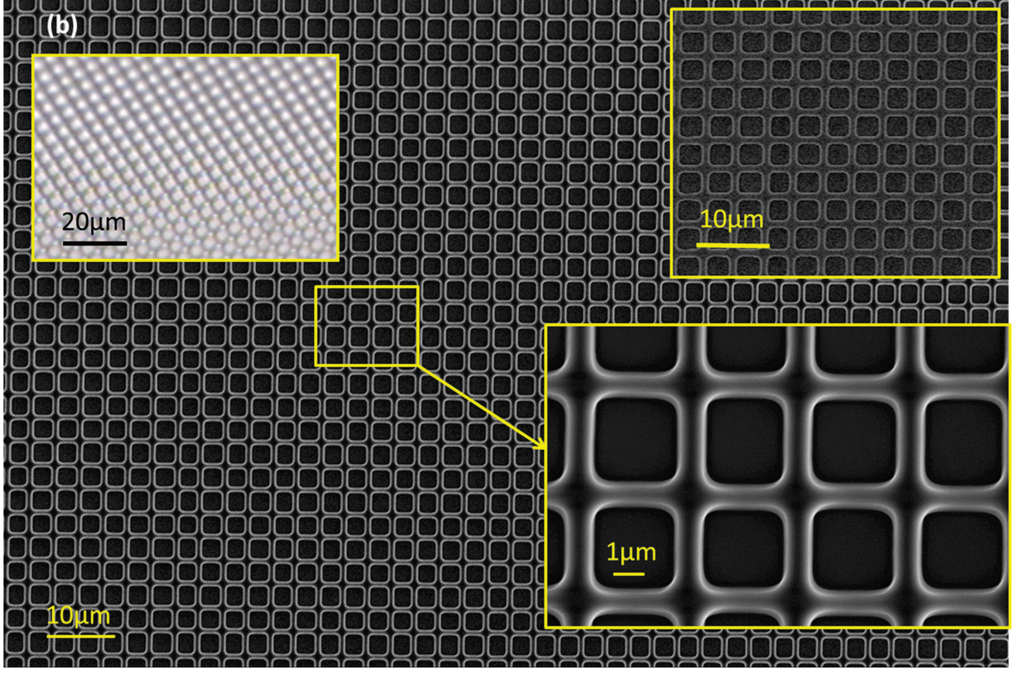

Figure 4.6 (a) Line width of a SU-8 photoresist after developing according to the laser power change. Insets shows bent (left) and stripped (right) SU-8 photoresists when exposure energy is not sufficient; (b) mesh-patterned SU-8 2000.5 master mold on a Si substrate. Line width, pitch and thickness are 840 nm, 3.5 µm and 500 nm, respectively. Left inset is the microscopic image of PDMS stamp surface detached from the master mold. Right upper inset shows a SU-8 2002 master mold on a Si substrate. Line width, pitch and thickness are 950 nm, 4 µm and 1.7 µm respectively.

An optimized imprinting condition for ZnO NP structure is a 7.5 wt% NP solution in 1-pentanol that generates uniform patterns over a large area by using a PDMS stamp fabricated from the SU-8 2000.5 master mold. **Figure 4.8a** shows a ZnO NP mesh and line patterns with about a 350 nm line width, and a 3.5 μm pitch. Neither a residual layer between patterns nor collapsed features were observed. An AFM image in **Figure 4.8a** left inset reveals the pattern height was around 200 nm. Energy dispersive X-ray (EDX) characterization performed on the ZnO line and substrate in **Figure 4.8b** verified the absence of residual layers between the fabricated lines as shown in **Figure 4.8c**. **Figure 4.8d** shows NWs selectively grown on the ZnO lines (**Figure 4.8b**) *via* a hydrothermal method [25, 69, 87, 138]. Elimination of ZnO remnants between the ZnO seed patterns is in fact a prerequisite for selective NW growth. Selective NW growth would be useful for many applications such as solar cells and optoelectric devices [139-142]. **Figure 4.9** demonstrates 4-inch wafer scale ZnO NP nanoimprinting. A SU-8 2000.5 master mold on a 4-inch silicon wafer was fabricated by LDW as shown in **Figure 4.9**a. The number density of the grid cell pattern on the wafer is approximately 10^7 per 1 cm^2. ZnO NP patterns were uniformly imprinted on a 4-inch silicon wafer (**Figure 4.9c**) and a quartz wafer (**Figure 4.9d**) by the PDMS stamp (**Figure 4.9b)**, which was accomplished within only several tens of seconds. Imprinted ZnO nanogratings produce diffraction patterns under solar light. The low temperature and pressure process characteristics enable high fidelity pattern transfer to flexible substrates (**Figures 4.9(e,f)**). Imprinted feature sizes of various NP from SU-8 photoresist master molds are recorded in **Table 4.1**.

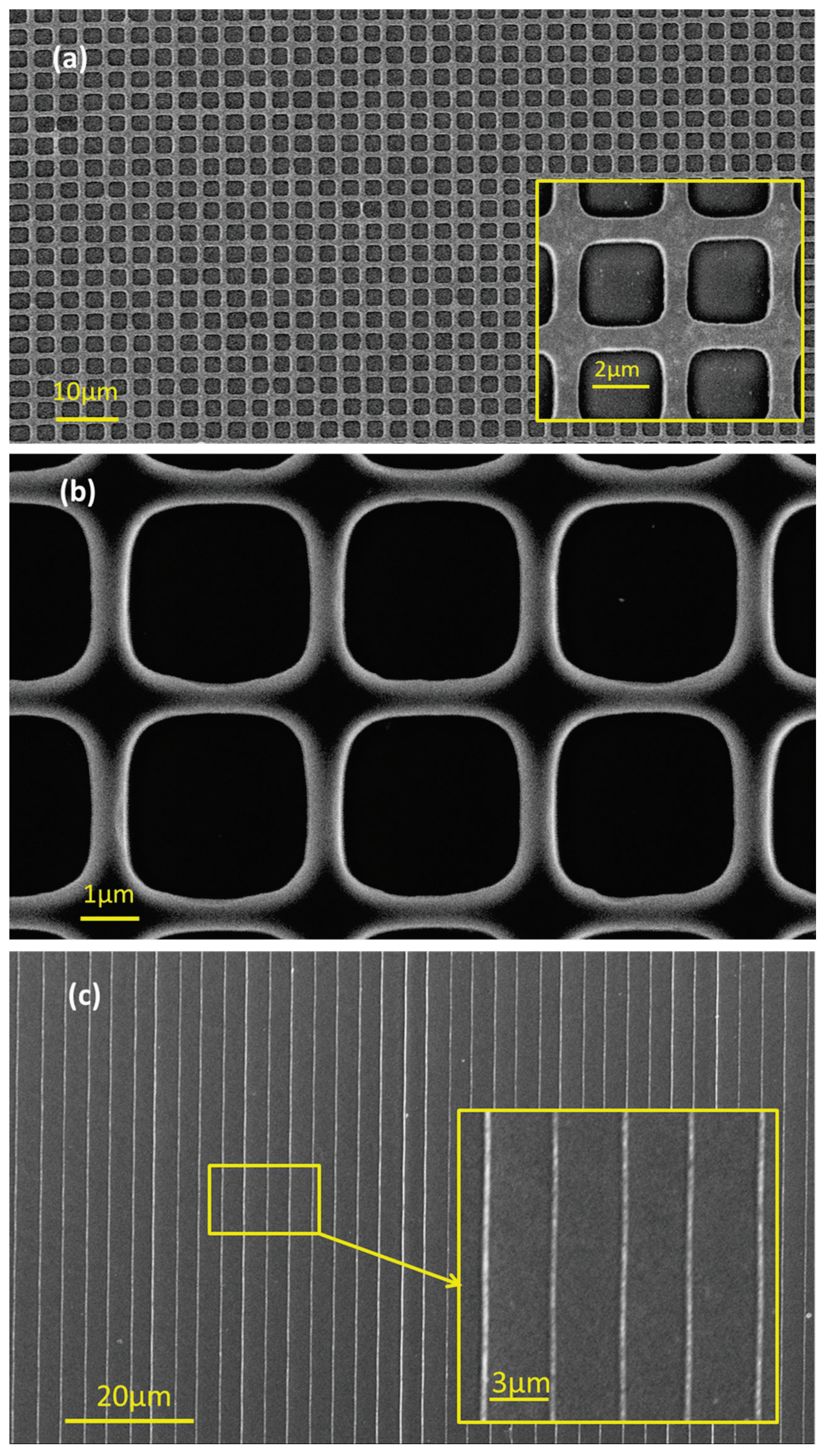

Figure 4.7 NP patterns imprinted with PDMS stamp from a SU-8 2002 master mold. (a) Silver NP mesh patterns on a glass substrate. The line width is 790 nm; (b) Si NP mesh patterns imprinted on a Si/SiO_2 substrate. Line width is 580 nm; (c) ZnO NP line patterns imprinted on a glass substrate. The line width is 300 nm.

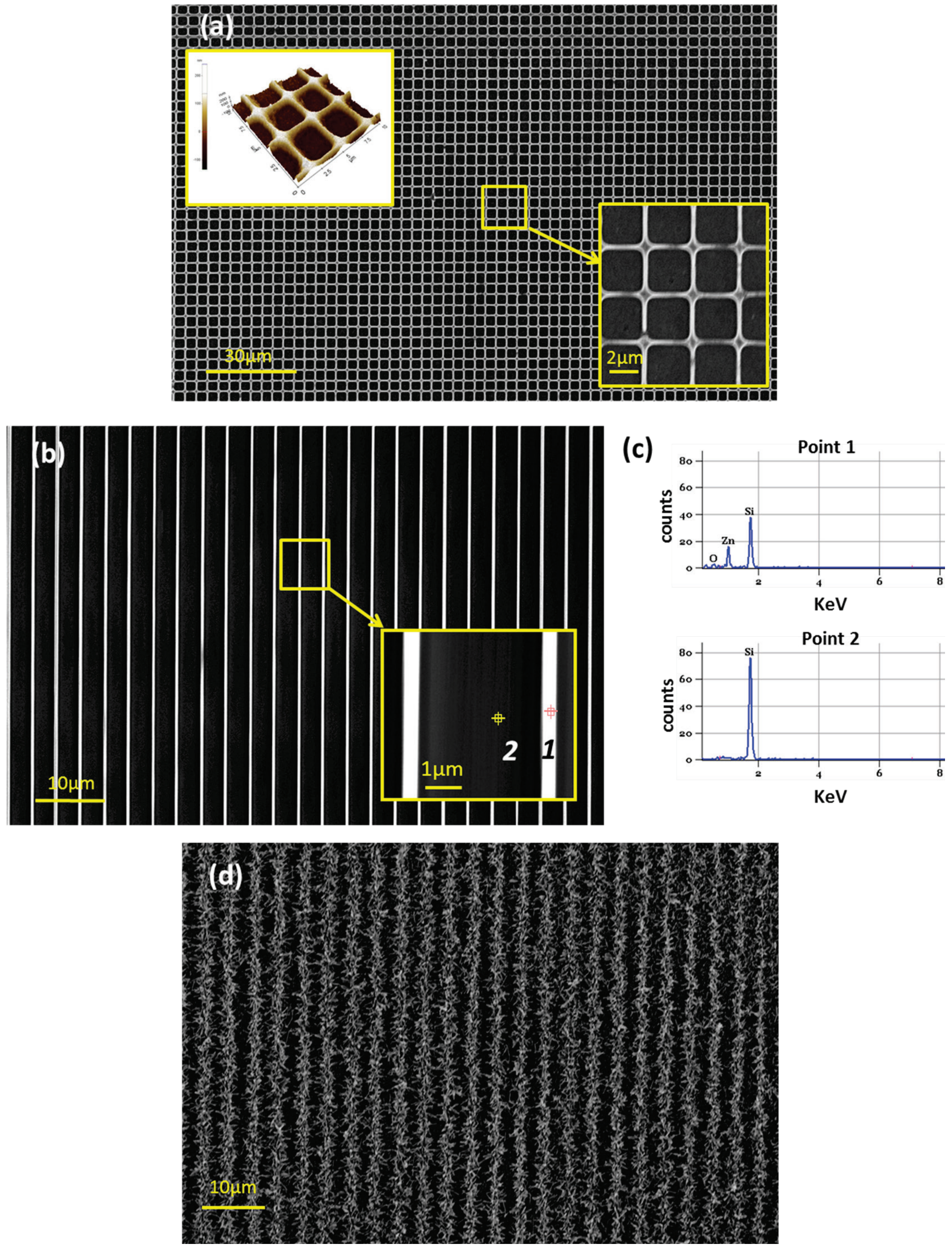

Figure 4.8 (a) SEM image of ZnO NP mesh patterns imprinted on a glass substrate using a PDMS stamp replicated from a SU-8 2000.5 master mold. The line width is 350 nm. The left inset represents an AFM image with a 200 nm feature height; (b) SEM image of ZnO NP line patterns imprinted on a Si wafer; (c) EDX analysis of point 1 and point 2 in (b); (d) ZnO NWs selevtively grown on the nanoimprinted ZnO NP seed patterns shown in (b)

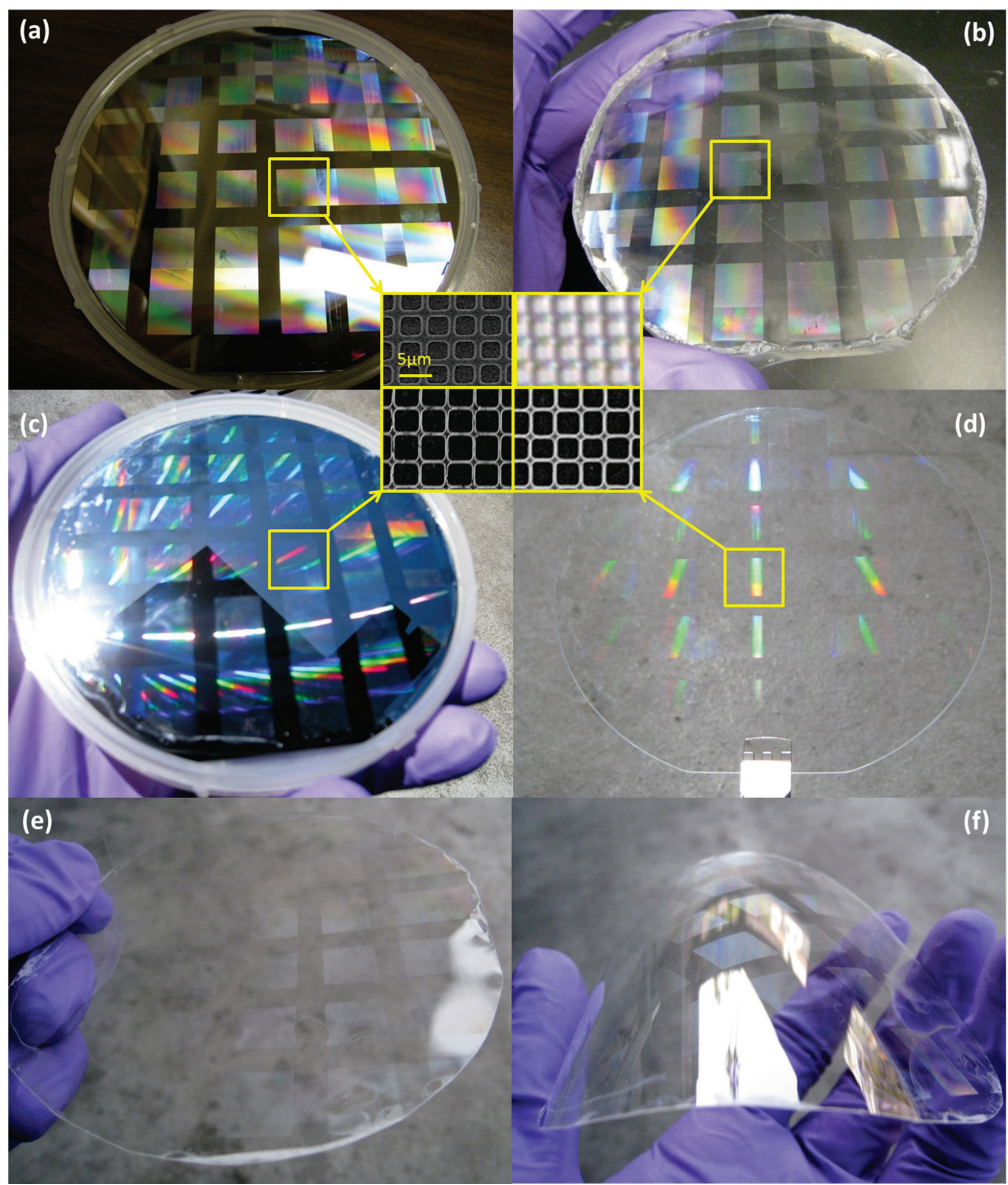

Figure 4.9 (a) 4-inch master mold fabricated with SU-8 2000.5 on a Si wafer; (b) PDMS stamp from the master mold; (c) diffraction patterns from imprinted ZnO mesh patterns on a Si wafer; (d) diffraction patterns from imprinted ZnO mesh patterns on a quartz wafer; (E), (F) ZnO patterns on a flexible polycarbonate sheet

Table 4.1 Imprinted feature sizes of various NPs from a SU-8 photoresist master mold

	NP concentration [wt%]	Master mold line width [nm]	Imprinted pattern line width [nm]
ZnO NP	7.5	840, 950	350
Si NP	0.16	950	580
Ag NP	14	950	790

4.4 LDW of OiR 700-10 phororesist to generate positive dot patterns

OiR 700-10, a positive photoresist that is removed after exposure to light, produced narrower patterns than SU-8 at the same laser power. However, insufficient laser power left residual photoresist under the grooves after developing (**Figure 4.10**). Line grooves from OiR 700-10 master molds produces line patterns on the PDMS stamp. To generate NP pillar patterns on the master mold, the pitch of laser exposure was reduced. Since the edges created by the crossing laser scans are rounded, as the groove pitch becomes smaller than 1µm, the remaining resist forms pillars (**Figures 4.11(a,c)**). The pillar size could be adjusted by controlling the distance between the laser scans. Imprinted feature sizes with groove pitch variation on the master molds are summarized in **Table 4.2**. No surface treatment was needed for PDMS stamp demolding from the master mold. About 1 µm and 500 nm diameter ZnO pillars were successfully imprinted on large areas (**Figures 4.11(b,d)**). As shown in **Figure 4.11e,** line patterns could also be generated from positive photoresists by line scans. ZnO line patterns with 200 nm line width were achieved over large areas. Furthermore, the line width could be tuned by the adjusting distance between laser scans. **Figure 4.11f** displays diffraction patterns from the ZnO pillars on the glass substrate.

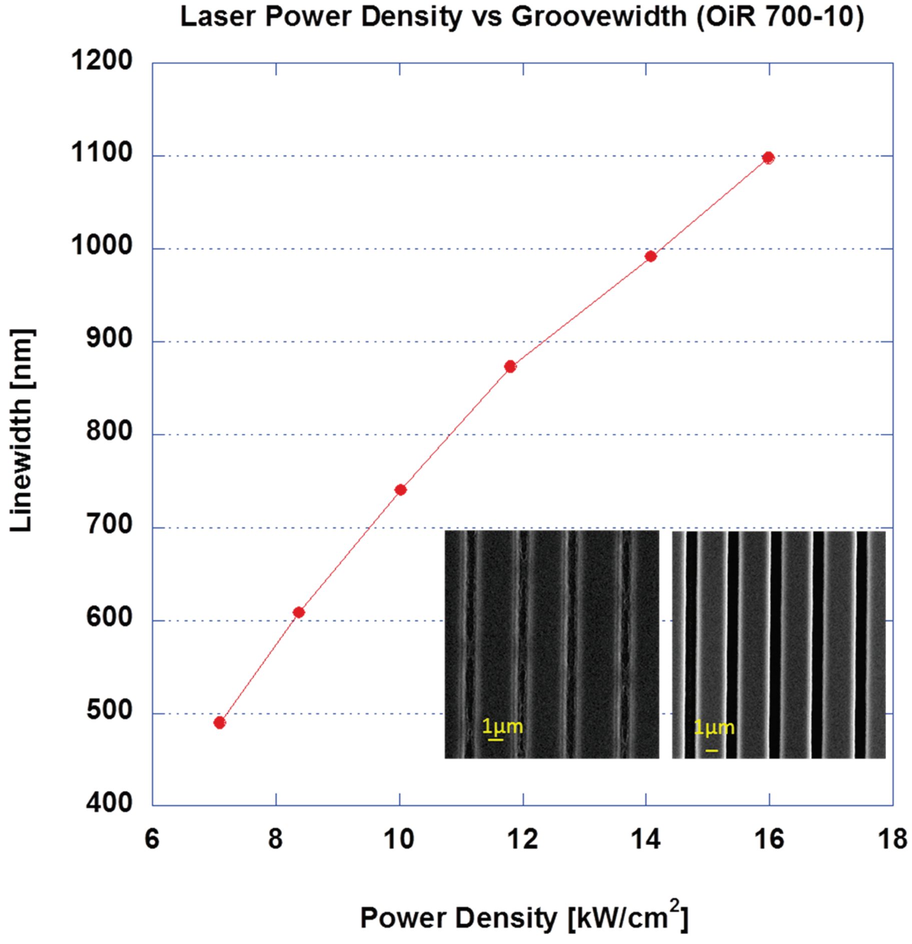

Figure 4.10 Line width of an OiR 700-10 photoresist after developing according to the laser power change. 610 nm groove width with residuals after developing when exposed to insufficient laser power (left inset). 870 nm Groove width with no residual when exposed to sufficient laser power (right inset).

Table 4.2 Imprinted ZnO NP feature sizes with groove pitch variation on the OiR 700-10 photoresist master mold

ZnO NP concentration [wt%]	Mold groove width and pitch [μm]	Imprinted feature size [nm]
7.5	0.87, 2	980 (pillar diameter)
7.5	0.87, 1.6	500 (pillar diameter)
7.5	0.87, 1.4	200 (line width)

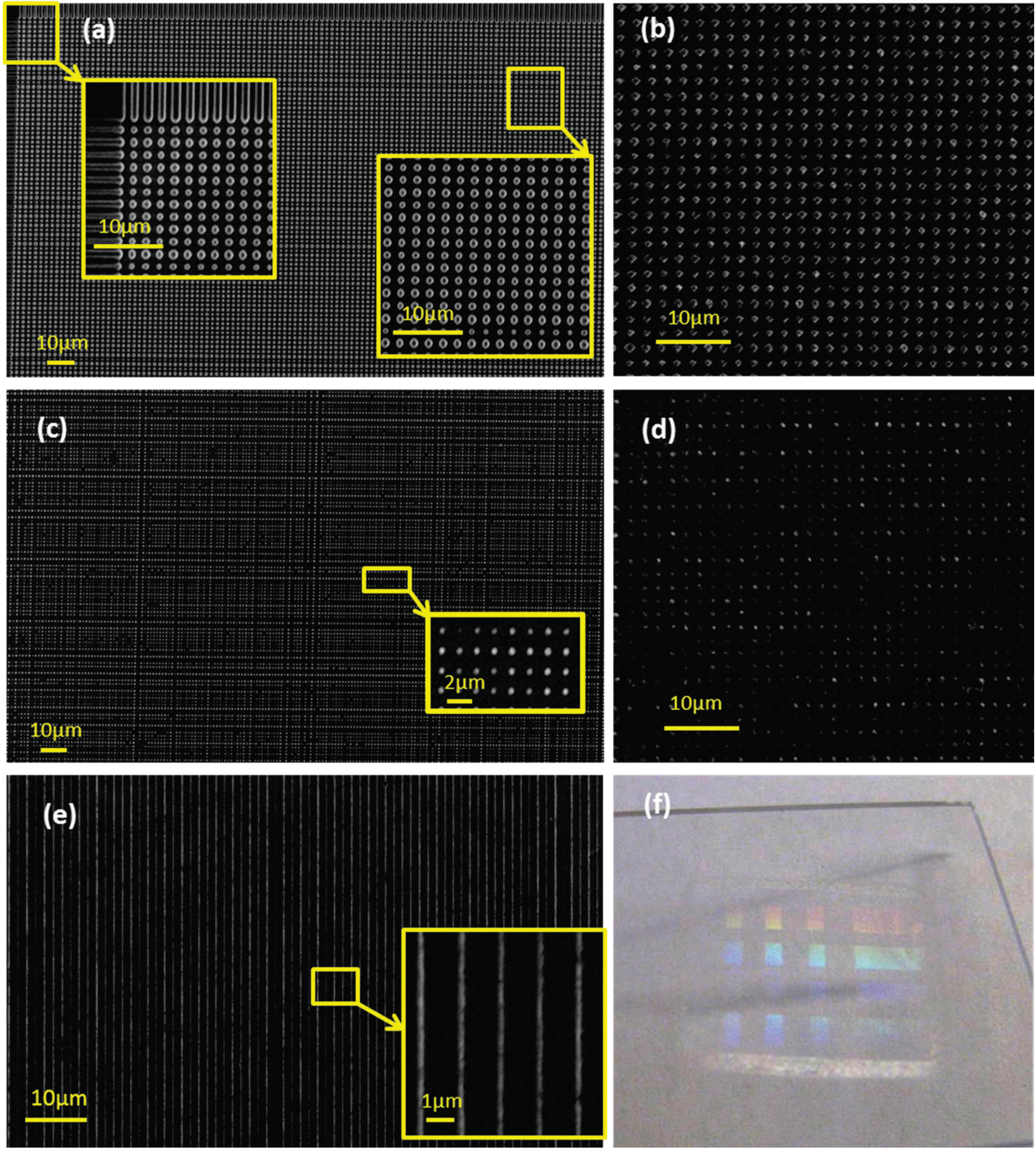

Figure 4.11 (a), (c) SEM images of OiR 700-10 master molds on a Si wafer. Distances between grooves are (a) 2 μm and (c) 1.6 μm respectively; (b) SEM images of 1 μm diameter size ZnO dot arrays and (d) 500 nm size dot arrays imprinted on a Si/SiO_2 wafer with a PDMS stamp the from the master mold (a) and (c) respectively; (e) ZnO NP lines with 200 nm width imprinted on a Si/SiO_2 wafer; (f) photoimage of diffraction patterns from the ZnO dot arrays imprinted on a glass under fluorescent light illumination.

4.5 Characteristics of UV ps laser as a photolithography light source

The UV ps laser has interesting characteristics when applied to the LDW photolithographic process. The required laser power, when the scan speed is 200 mm·s^{-1}, for SU-8 patterns of around 850 nm line width with the ps laser is around 73 μW. It has been verified that when the scan speed decreases to 100 μm·s^{-1}, or 1/2000, the laser power required for the same line width also decreases to around 44 nW, or 1/1659. This shows quite good proportionality between laser power and scan speed. The power range corresponding to the positive photoresist, OiR 700-10 is in the same order of magnitude. Since the peak power of ps laser used for the research in chapter 4 is around 0.5 W considering all the losses within the beam pass, it is predictable that the scan speed could increase by several orders of magnitude, via using a fast and mechanically stable scanning tool along with optical components resistant to optical breakdown.

A parallel comparison of the laser power range with other LDW photolithography systems is not easy, since the wavelength, pulse duration, repetition rate, absorbance and absorption mechanism of the photoresist, and beam spot size are all different. However, it is worth examining the laser power range of other systems presenting similar resolution with the LDW method. Thiel *et al*. [37] generated submicron feature using 532 nm CW laser for IP-L and IP-G (both from Nanoscribe GmbH, Germany), and SU-8 photoresist. The power level was approximately 20~80 mW and the scan speed was around 100 μm·s^{-1}. The difference of the power level between 44 nW in ps system and 10 mW in CW system at the same 100 μm·s^{-1} scan speed is as much as order of 10^6, highlighting a huge difference although it is recognized that the absorbance of those photoresist is lower for the 532 nm wavelength. Considering the small beam size of the LDW system of their CW laser setup, the difference of power density is even bigger. Additionally, a preliminary experiment of LDW photolithography of a g-line positive photoresist (Fujifilm, OCG 825 35CS) with 514 nm wavelength CW laser required a power level of around 0.2 mW at 100 μm·s^{-1} which is still by a factor of 10^4 higher compared with ps laser power. Unfortunately, there is no data available for the power range of UV CW or nanosecond (NS) laser which would enable straightforward comparison between CW, NS and ps laser. One possible reason for such a big difference of the laser power level in ps laser is the peak power that is much higher than the average power. The relationship between average power (P_{avg}) and peak power (P_{peak}) is as follows when assuming a rectangular pulse train and constant pulse energy in every pulse as shown in **Figure 4.12** (source: a refined diagram from Spectra-Physics).

$$P_{avg} = \frac{E}{T} = Ef \tag{4.2}$$

$$P_{peak} = \frac{E}{\Delta t}, \tag{4.3}$$

E denotes pulse energy and T, f and Δt is period, repetition rate and pulse duration respectively. The average power is the number that a power meter shows. For example, the peak power corresponding to the average power of 80MHz-12ps laser for 73 µW and 44 nW which is the power level for 200 mm·s^{-1} and 100 µm·s^{-1} scan speed as mentioned above is 76 mW and 46 µW respectively. The peak power, however, is still quite low compared with the laser power level of CW lasers. Therefore, a full understanding of the phenomena requires investigation of a different photon absorption mechanism of the photoresists in the ultra short-pulse laser, including possible multi-photon effects. Unfortunately, the multi-photon effects of 355 nm UV ps laser in those photoresists are not yet clear and their study would be the subject of future work.

The UV ps laser has very different characteristics in LDW photolithographic process from that of CW lasers. Clearly, using a high repetition UV ps laser is a very efficient way for extremely fast direct writing photolithographic process even though the mechanism is not fully revealed yet.

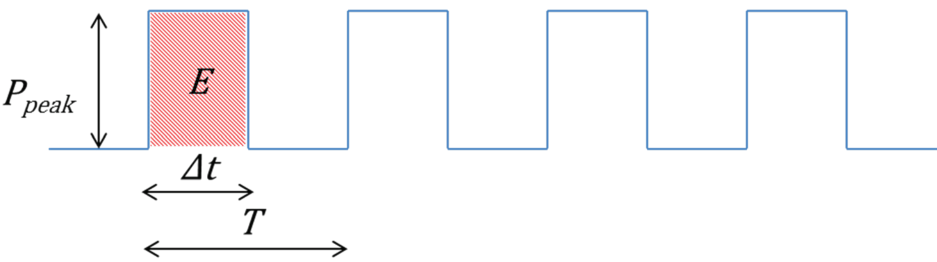

Figure 4.12 Rectangular laser pulse train with constant energy in every pulse. P_{peak}, E, Δt *and* T represents peak power, pulse energy, pulse duration and period respectively. (Source: a refined diagram from Spectra-Physics)

4.6 Limitations and solutions

The smallest line width of the SU-8 mold reachable through the proposed LDW process was around 800 nm which is far smaller than the laser beam spot size of 1.56 µm as shown in section 4.3 and 4.2.1. This is attributed to the Gaussian beam profile. As shown in **Figure 4.13a**, by precisely adjusting the laser power or pulse energy close to the cross-linking threshold, a single structure smaller than the beam spot can be created. While this characteristic is similar with that of ablation for single feature generation, there is a big difference in photolithographic process when the gap between lines becomes narrower. In an ablation process, intensity below threshold does not affect much the structural integrity of adjacent structures. However, when the direct writing pitch between two lines becomes smaller in a photolithographic process, the cumulative photon

dose in the interline space may exceed the cross-linking threshold, so that each line is not developed separately (**Figure 4.13b**) [143, 144]. This is in fact the biggest challenge in LDW application to photolithography that hinders reducing the gap between imprinted structures. The smallest pitch achievable through the setup with the beam profile shown section 4.2.2 was around 2 μm which becomes larger as the writing speed increases resulting from the vibration of the system. This limitation was also detected in fabrication of a mold with the OiR 700-10 photoresist.

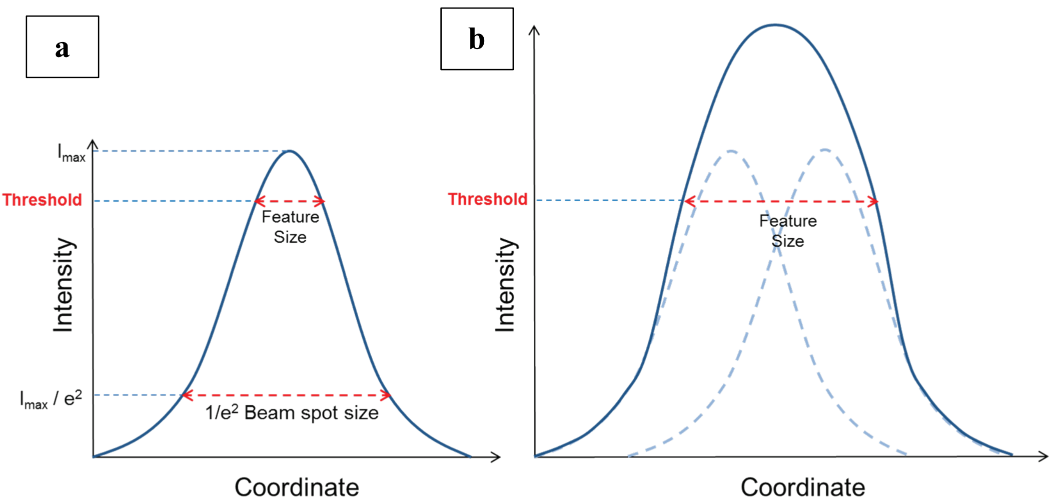

Figure 4.13 (a) By precisely adjusting the laser power or pulse energy close to the cross-linking threshold, a single structure smaller than the beam spot can be created; (b) as the direct writing pitch between two lines becomes smaller in the photolithographic process, the cross-linking threshold exceeds in the interstice, so that each line is unable to be developed separately.

One straightforward solution to reduce the pitch between lines is using a high numerical aperture (N.A.) objective lens to reduce the beam spot size. However high N.A. objective lens for UV laser is expensive and the very small working distance requires extreme caution to maintain the distance between the objective lens and wafer size substrates. Another method to overcome the limitation is the stimulated-emission-depletion laser direct writing (STED-LDW) process [143, 145-147] . There also has been an attempt by employing scheme based on quencher diffusion, in a chemical equivalent of STED [144]. Those methods, however, are not only complicated but also require specialized photoinitiators. Furthermore, it is not applicable for very fast large area LDW process. The simplest solution for these difficulties is to imprint multiple times. As shown in **Figure 4.14**, secondly generated features (A) fill the interstices of the structures from the preceded imprinting process (B) resulting in a reduced pitch. The precise control of the successive stamping steps possibly can be achieved by facilitating additional alignment tools. For multiple imprintings, the pre-generated patterns require sintering

process for hardening in order not to be collapsed by the successive imprinting. Laser sintering process is possibly useful for the flexible polymer substrate. Multiple imprinting actually generates interesting multilayer structures as shown in **Figure 4.15.** Although the multilayer structures are not fully 3-D such as for example the photonic crystals fabricated by multiphoton polymerization [138, 144], they suggest potential applications that would be also subject of future work.

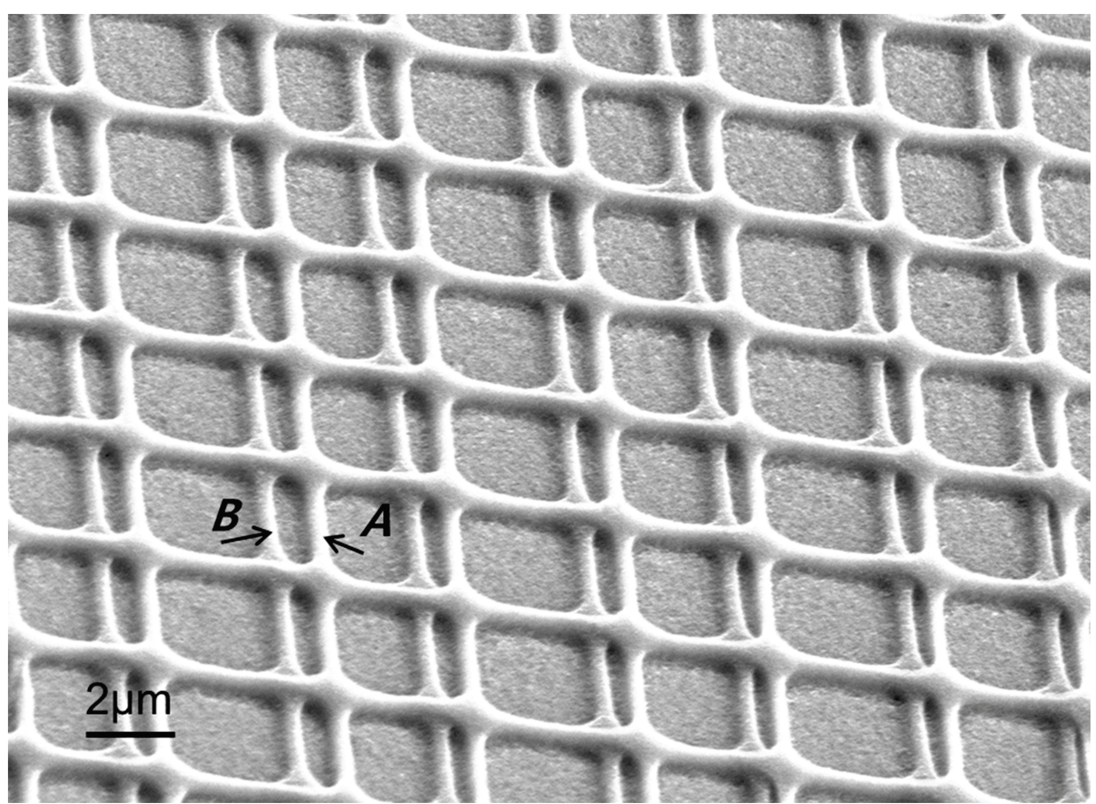

Figure 4.14 Mesh structures generated by twice imprinting of TiO_2 NPs on a FTO glass substrate; secondly imprinted features (A) fill the interstices of the structures from the preceded imprinting process (B) resulting in a reduced pitch.

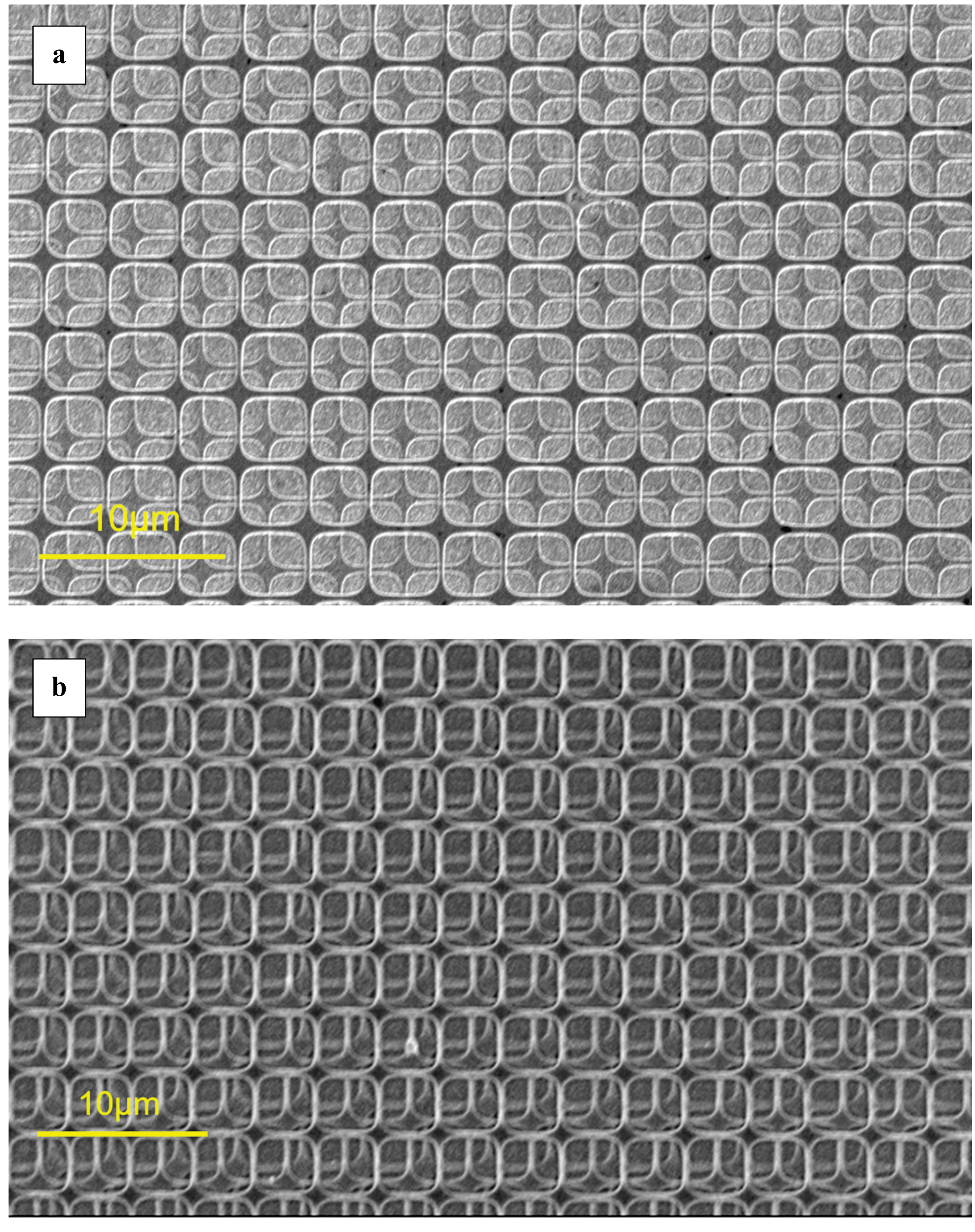

Figure 4.15 Multiple imprinting processes generate multilayer structures. (a) two layers; (b) three layers on FTO glass substrates

4.7 Conclusion

In summary, laser-assisted one-step direct nanoimprinting of metal and semiconductor NPs was investigated to fabricate submicron structures, including mesh, line, nanopillar and NW arrays. Various kinds and pattern types of NP submicron structures were generated using PDMS stamps fabricated from LDW process, demonstrating the versatility of this method. Compared with conventional nanoimprinting where EBL or low speed LDW to make submicron structures is incorporated, high speed LDW using a relatively low numerical aperture (N.A.= 0.5) lens enables larger area master mold imprinting through a much faster and cost effective fabrication process. Direct imprinting using NP solutions was shown to incur negligible residual layers and could eliminate etching and lift-off process, therefore greatly reducing the complexity of the fabrication sequence. Since long cooling steps after imprinting is not necessary, the imprinting process time can be remarkably diminished. Furthermore, the low temperature and pressure applied through the entire process enable imprinting on flexible substrates. This approach, therefore, has powerful potential to achieve large area nanoimprinting with high throughput and ultra-low cost, hence opening the way to applications, including realistic new photovoltaic configurations.

Chapter 5

Digital selective growth of ZnO NW arrays from NP seeds patterned by drop-on-demand inkjet printing on a flexible substrate

A drop on demand (DOD) ink jet process integrated with CAD system was demonstrated as another example of direct writing method for the ZnO nanomaterial patterning. ZnO NW arrays were selectively grown on the inkjet-printed seed patterns. Through proper natural convection suppression during the hydrothermal growth, successful ZnO NW local growth could be achieved. Without any need for photolithographic process or stamp preparation, the NW growth location can be easily modified with high degree of freedom when the design needs to be changed. Moreover, this process is compatible with flexible plastic substrates and can be scaled up for larger substrate for mass production or roll-to-roll process.

5.1 Introduction

Extended and oriented nanostructures are desirable for many applications, including microelectronic devices, chemical and biological sensing and diagnosis, light emitting displays, energy conversion and storage, catalyst, drug delivery, separation and optical storage [70, 148-151]. Among the nanorods, ZnO NWs have attracted much attention due to their direct band gap of 3.37eV and a large exciton binding energy of 60 meV, which render them a promising candidate material for applications in various optoelectronics. The ability to build functional nanostructured assemblies at predetermined locations requires both control of their growth structure and morphology as well as their placement at specific locations [150]. The usual approach entails a series

of multi-steps for growth, harvest and placement of NWs, which are very time consuming, expensive, and low yield. To overcome the difficulties encountered in multi-step serial processes, new fabrication routes implement direct growth at specific locations with desired NW morphology. For site selective patterned NW growth, photolithographic method is usually applied to pattern the catalyst layer for local growth [70, 151-154]. Other approaches used microcontact printing method for surface modification by patterned self-assembled monolayers with hydrophobic and hydrophilic end groups on silver or silicon substrate [149, 150, 155] or microcontact printing of seed NPs [156]. However, these approaches are subject to practical limitations because they need a photomask for photolithography or mold for contact printing, which cannot be modified once they are fabricated. Furthermore, photolithographic method cannot be applied for heat and corrosive chemical sensitive plastic substrates.

In this research, fully digital selective ZnO NW growth using inkjet-printed seed patterning and hydrothermal ZnO local growth is introduced. The proposed process is very fast, low cost, environmentally benign, and low temperature. Therefore it can be applied on flexible plastic substrates and scaled up for larger substrates for mass production or roll-to-roll process. Most of all, the NW growth location can be easily modified when the inkjet printing process is integrated with CAD system to allow huge degree of freedom at the development stage.

5.2 Experimental setup

Direct patterned ZnO NW arrays were selectively grown from the inkjet-printed ZnO NP nuclei through the hydrothermal decomposition of a zinc complex. The process is mainly composed of two simple steps as shown in **Figure 5.1**; (1) ZnO NP inkjet printing on a substrate, and (2) subsequent selective ZnO NW hydrothermal growth on the inkjet-printed ZnO NP seeds. All processes were carried out at plastic compatible low temperature (<95°C) without using any conventional photolithography or vacuum deposition processes.

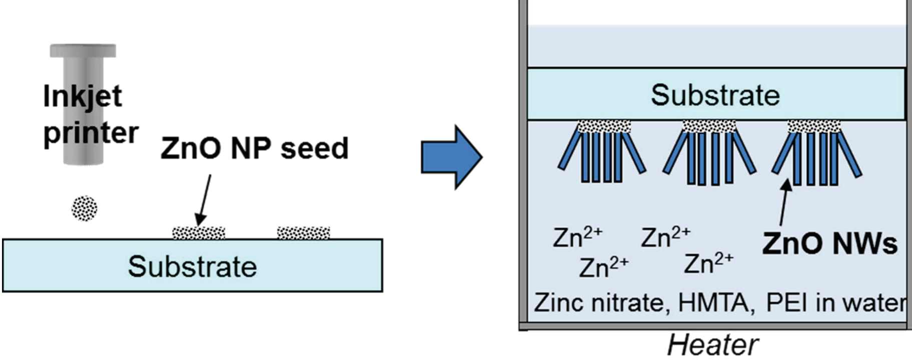

Figure 5.1 Process schematics of the direct patterned ZnO NW growth from the inkjet-printed ZnO NPs.

5.2.1 ZnO NP seed synthesis

ZnO NPs were used as seeds for the subsequent selective ZnO NW growth. ZnO NP ink was prepared by modifying the original method by Pacholski [10] as mentioned in section 2.1.

5.2.2 ZnO NP seed inkjet printing

Arbitrary digital patterns of ZnO seed NPs were drawn on a glass or polymer substrate by the generation of NP ink microdroplets using the piezoelectric DOD (drop-on-demand) printing system [32, 157] as shown in **Figure 5.2a**. The DOD jetting system was composed of a backpressure controller, a purging system and a piezoelectric jetting system. About 10 mbar vacuum was maintained in the reservoir to prevent NP ink from leaking from the nozzle of the capillary tube due to the small viscosity and low surface tension of the ethanol based NP ink. A vacuum controller and a magnetic valve were connected between the vacuum pump and the reservoir to minimize the loss of ethanol due to continuous evaporation. To purge in the case of clogging, pressure controlled nitrogen gas was used and the purging pressure was controlled at 0.4 psi.

A jet head (MJ-SF, MicroFab) with a 50 μm nozzle diameter was used to produce microdroplets and a bipolar voltage waveform with amplitude of ±13 ~ ±15 V was applied (**Figure 5.2a**, inset graph]. Briefly, the first rising voltage expands the glass capillary and a droplet is pushed outside the nozzle due to the falling voltage. The final rising voltage cancels some of the residual acoustic oscillations that remain after drop ejection and may cause satellite droplets. The optimum jetting parameters were found to be 2 / 40 / 4 / 80 / 2 μs (A, B, C, D and E in **Figure 5.2a** inset graph). The signal generator used to produce microdroplets also triggered the CCD camera, so that the CCD

captures images at the droplet generation frequency. As shown in **Figure 5.2b**, the CCD camera provided in situ "frozen" transmission images of the droplet to check for satellite droplet generation as well as to measure the droplet velocity and size. After generating stable NP ink droplets various structures were made on the substrate by moving a precision translation stage. The gap between the jetting head tip and the glass substrate was maintained at 2 mm.

The temperature of the vacuum chuck was controlled by a thermocouple and Mica heater to facilitate evaporation of the solvent from the NP ink. Proper solvent evaporation is very important for successful 2D patterning *via* inkjet printing of NPs. Vacuum (300 mbar) was applied through 0.5 mm diameter holes to assure the intimate contact between the heater and the substrate on the vacuum chuck.

Upon finishing inkjet printing, the inkjet-printed micro-patterns were composed of ZnO NPs. The NP micro-patterns were used for patterned seed layers enabling subsequent ZnO NW selective growth. Droplets of various diameters (1~200 μm) could be generated by changing nozzle diameter, jetting parameter (applied voltage waveform and amplitude), and substrate heating conditions. After inkjet printing, the substrate was dried and annealed at 95°C for 20 minutes to ensure the seed particle adhesion to the substrate.

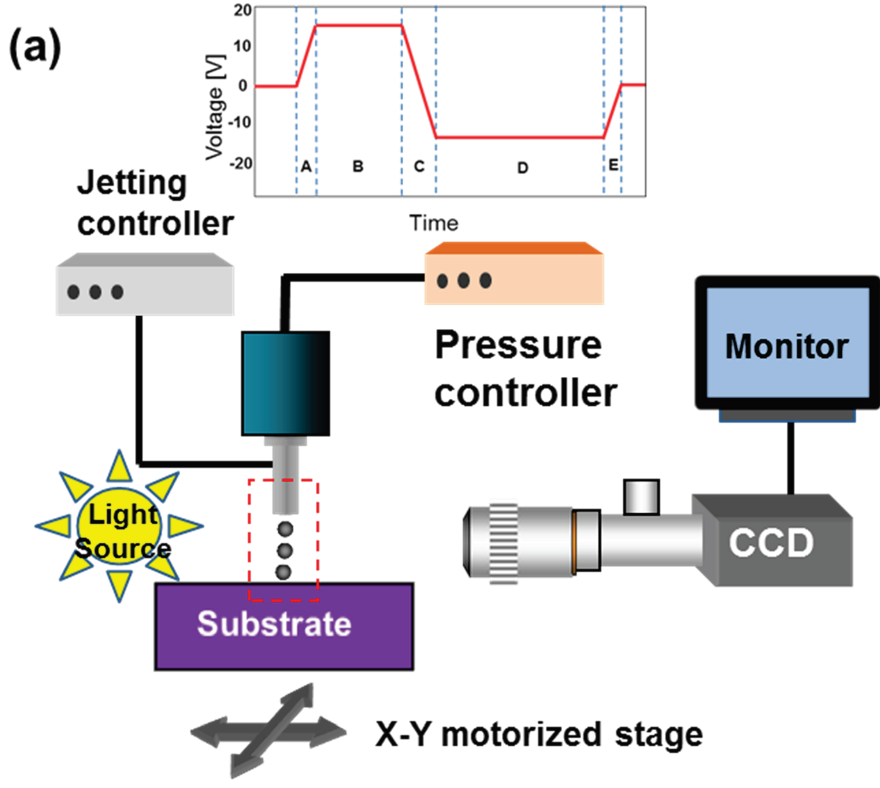

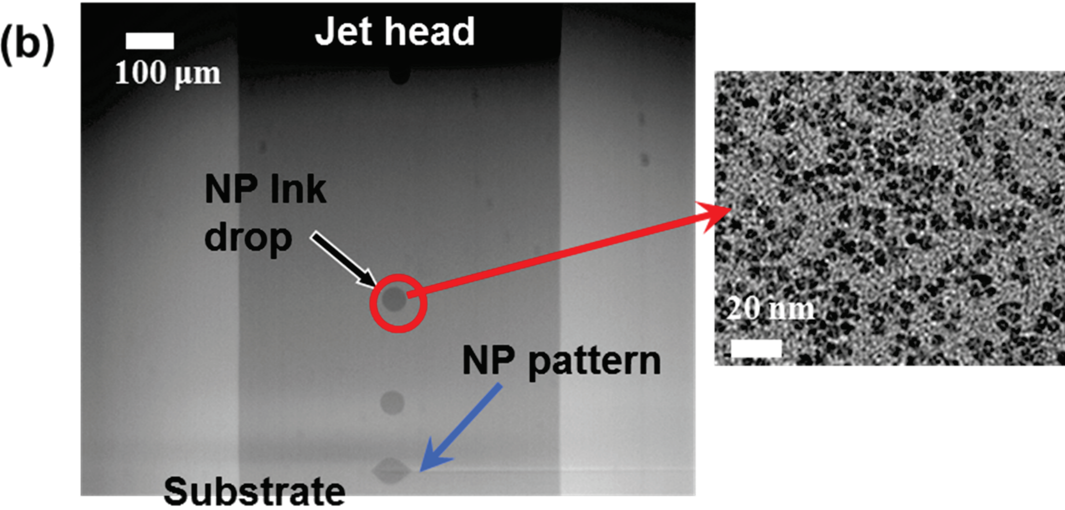

Figure 5.2 (a) Schematic diagram of the inkjet printing system setup; (b) time resolved image of the ZnO seed NP inkjet printing by piezo-electrically driven drop-on-demand inkjet printing system

5.2.3 ZnO NW selective growth with natural convection suppression

ZnO NWs were selectively grown only on the inkjet-printed ZnO NP seed by immersing seed-inkjet-printed substrates in aqueous solutions. The details of ZnO NW synthesis have been presented in section 2.4. The substrate was suspended upside-down in an open crystallizing dish filled with solutions to remove the unexpected precipitation of homogeneously grown ZnO NW on the substrate. However, the inkjet-printed ZnO NP seeds could become mobile due to strong natural convective flow and could diffuse to the unpatterned (unseeded) adjacent substrate region as shown in **Figure 5.3a**. This, in turn, can induce secondary ZnO NW growth at unwanted areas resulting in wavy random white patterns of ZnO NWs as shown in **Figures 5.3(b~d)**. To remove this secondary growth on the unseeded area, a thin cover glass was added to the substrate with 2 mm spacer to control and suppress the natural convection flow (**Figure 5.3e**). **Figures 5.3(f~h)** signify that the current approach can successfully reduce the secondary ZnO NW growth and produce highly selective ZnO NW growth on the inkjet-printed ZnO NP drop arrays.

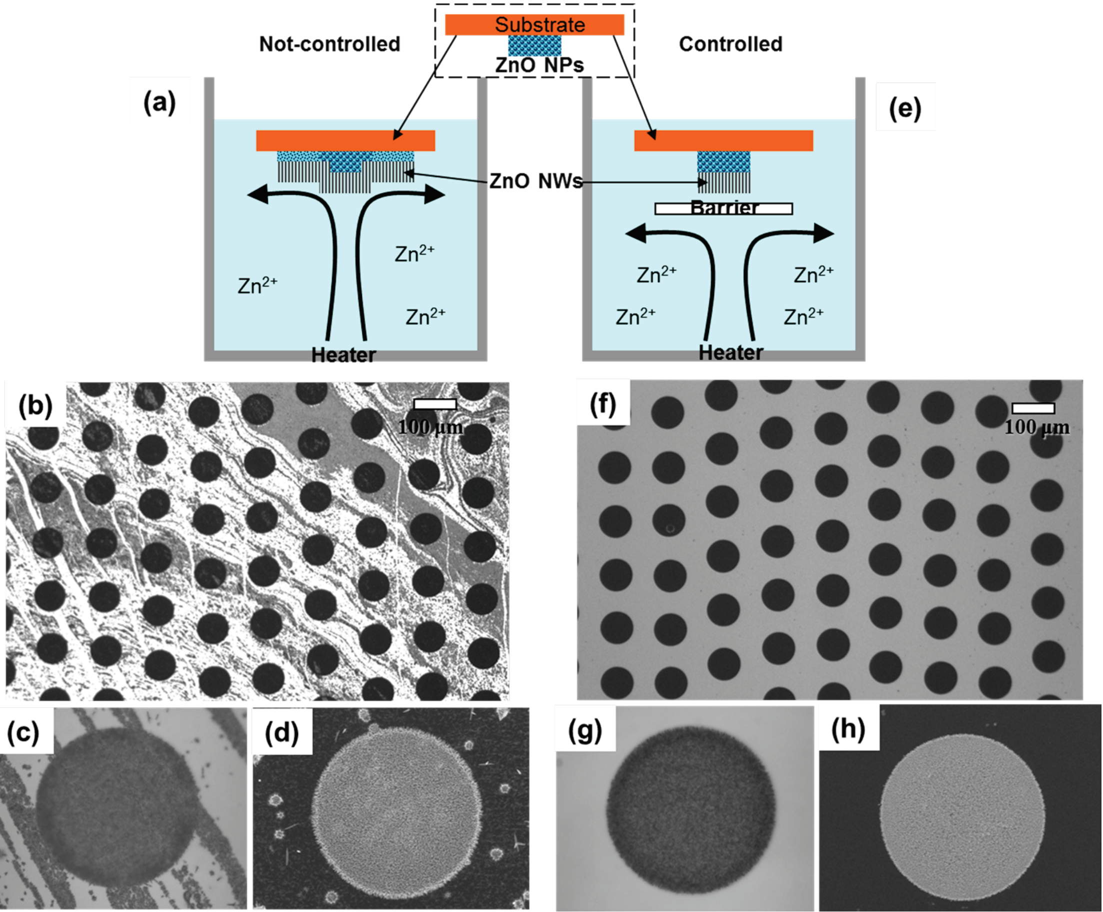

Figure 5.3 Selective ZnO NW growth (a-d) without natural convection suppression and (e-h) with natural convection control. Note the secondary growth in (a-d) and the absence of the secondary growth in (e-h).

5.3 Characterization

Figure 5.4 shows the SEM pictures of selectively grown ZnO NW array on the inkjet-printed ZnO NP seeds. **Figures 5.4a** and **5.4b** show the ZnO NW growth on the 120 μm dot arrays of inkjet-printed ZnO seed NP ink droplets. The DOD inkjet print head originally generated 50 μm diameter ZnO NP ink droplets (~100 pico-liter) that spread out and dried to various sized ZnO NP circular patterns, depending on the substrate heating condition. Smaller diameter ZnO NP seed patterns could be achieved by applying substrate heating. The usual length of the ZnO NW was around 10~12 μm with diameter in the range of 100~150 nm after one-time growth as shown in the cross section pictures (**Figures 5.4(c,d)**). Longer ZnO NW could be obtained by introducing the samples repeatedly into fresh solution baths every several hours. The arrays were then rinsed with deionized water and dried in N_2 for SEM imaging.

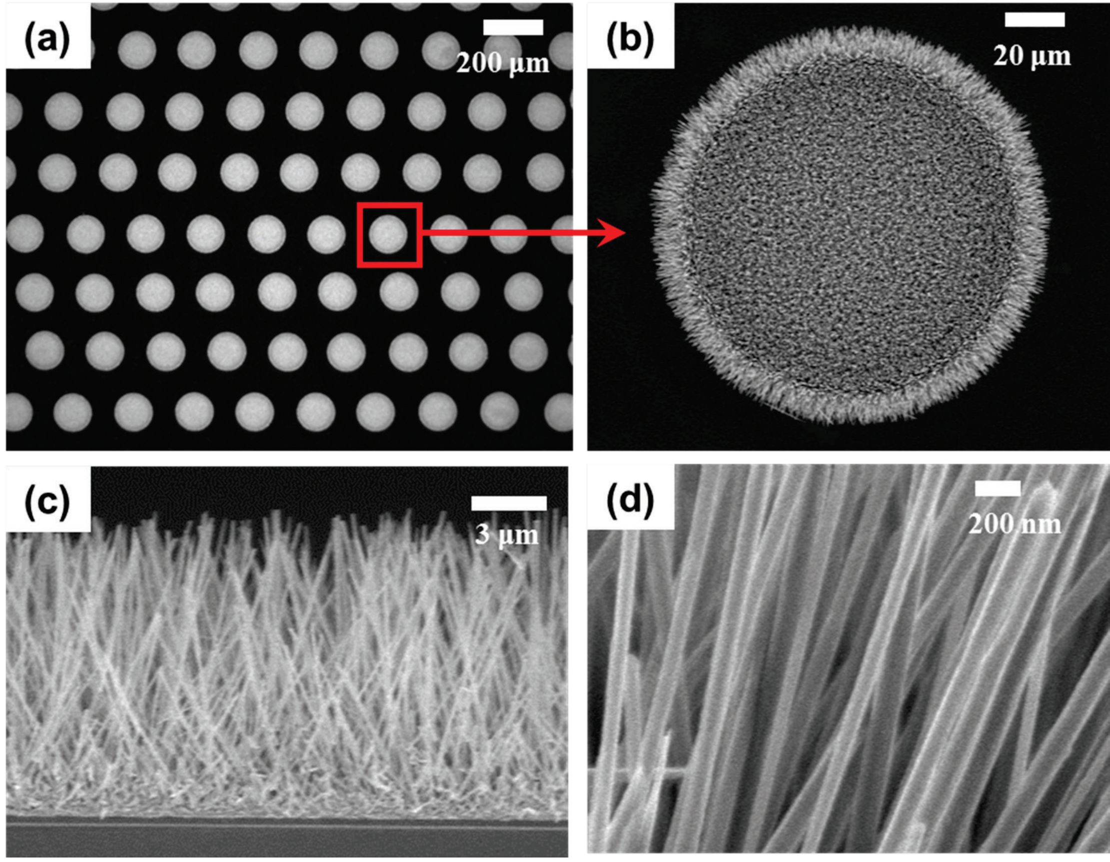

Figure 5.4 (a), (b) SEM pictures of selective ZnO NW growth on the inkjet-printed ZnO NP seeds; (c), (d) cross sectional SEM pictures of ZnO NWs.

More detailed characteristics of ZnO NW selective growth on the inkjet-printed ZnO NP seed droplet can be explained in **Figure 5.5**. **Figure 5.5a** shows a tilted SEM image and **Figure 5.5(b~d)** show cross sectional view. The ZnO NWs are grown vertically within ±10° deviation angle on the central part of a circular pattern (**Figure 5.5b**) while urchin-like ZnO NWs are grown at the edge of the circular pattern (**Figure 5.5c**). The urchin-like dense ZnO NWs show highly ordered outward radial directional growth that can be explained as follows. Firstly, urchin-like radial growth minimizes the interaction among each ZnO NWs. In the interior of the seed pattern and away from the edges, the NWs preferentially grow vertically aligned as shown in **Figure 5.5b**. However, on the edge, urchin-like radial growth mode can favorably minimize the interaction between the NWs while increasing the distance as they grow. Secondly, ZnO NWs preferentially grow toward the high concentration precursor supply. The affluent precursor supply from outside of the circular ZnO NP seed pattern redirects the NW growth to the outward direction compared with the ZnO NWs in the central part. The high density and the bigger length of ZnO NWs grow on the edge due to those effects.

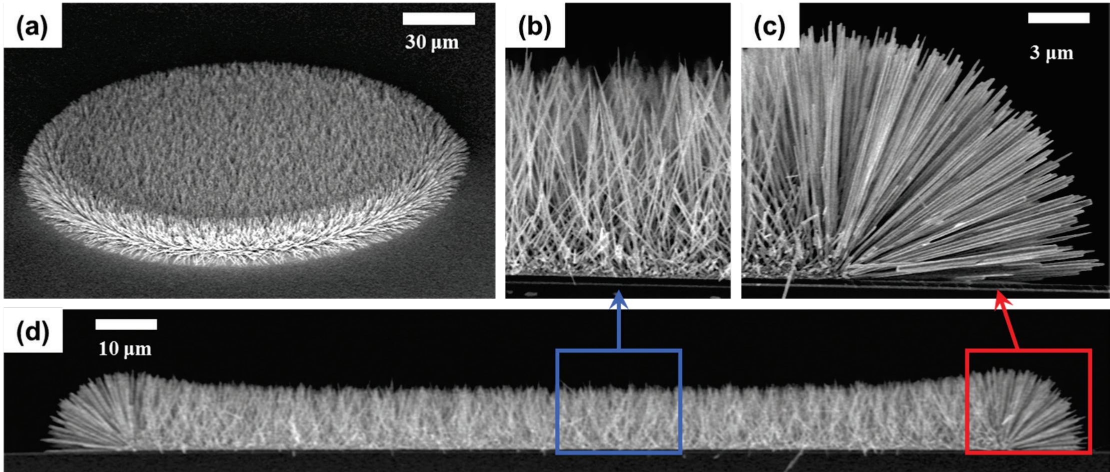

Figure 5.5 SEM pictures of the ZnO NW grown on a single drop of inkjet printed ZnO seed NPs. (a) Tilted view; (b), (c) magnified cross sectional view at the center and at the edge; (d) cross sectional view of the ZnO NW array on one inkjet droplet.

Various diameter circular patterns of ZnO NWs were successfully grown on the inkjet-printed ZnO NP seeds as shown in **Figure 5.6**. The ZnO NW array pattern (**Figure 5.6b** left picture) was slightly bigger than the original inkjet-printed ZnO NP seed (**Figure 5.6b** right picture indicated by red dotted line) because the horizontal ZnO NWs from the urchin-like radial growth at the edge of the NP seed pattern added extra length. The diameter of the initial inkjet-printed ZnO NP seed pattern determined the final configuration of ZnO NW selective growth. As shown in top view SEM images (**Figures 5.6(a,c)**), there are two length regimes; the diameter of the inkjet-printed ZnO NP seed (indicated by red dotted circles) and the length of the urchin-like ZnO NW growth at the edge of the circle (indicated by blue dotted circles.). When the diameter of the inkjet-printed ZnO NP seed (indicated by red dotted circles) is larger than 20 µm, the general configuration of the ZnO NWs grown on the inkjet-printed seed looks alike. As the diameter of the inkjet-printed ZnO NP seed decreases (**Figure 5.6c**) and especially when it becomes smaller than the length of the urchin-like ZnO NW growth, the latter growth mode becomes more dominant as shown in **Figure 5.6c(v)**. The usual length of individual ZnO NWs was around 10 µm. However, when the inkjet-printed seed NP patterns are very small, the individual ZnO NW length almost doubled (**Figure 5.6c(v)**). This may be because the Zn precursor supply was adequate for growing longer ZnO NWs, albeit of lower number density. On the other hand, the precursor consumption was not as competitive as in the densely packed ZnO NW array growth.

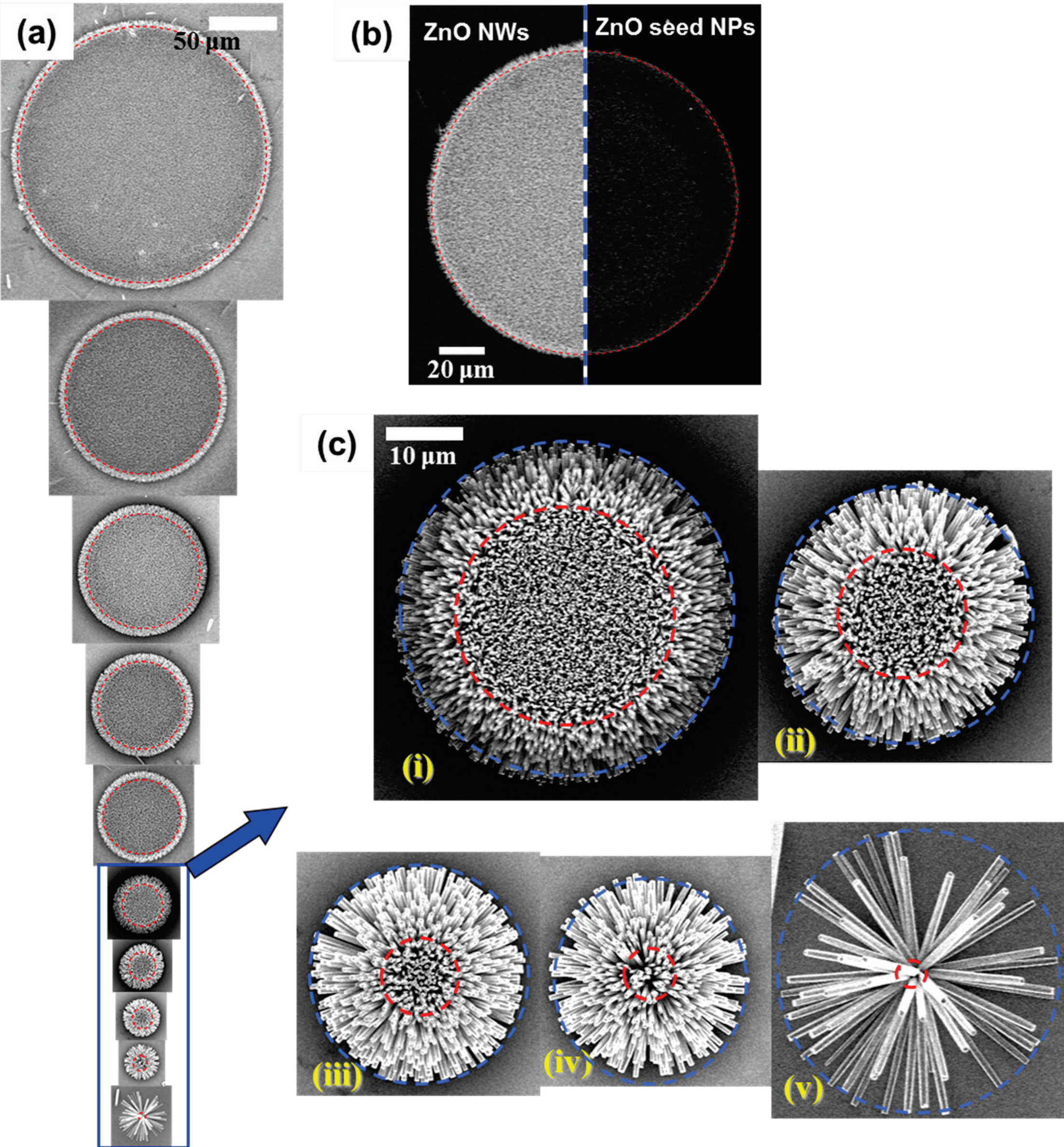

Figure 5.6 (a) SEM pictures of ZnO NW arrays with various diameters from few microns to several hundreds microns; (b) SEM pictures of the inkjet-printed ZnO seed NPs (right) and actual ZnO NW growth (left) on the seed NPs; (c) magnified SEM picture of small diameter ZnO NW arrays in blue box in Figure 5(a). Red and blue dotted circles represent original inkjet-printed seed diameter and total diameter of ZnO NW patterned growth respectively.

The growth process could be conducted multiple times to grow longer NWs by simply repeating with fresh precursor solution. **Figure 5.7a** shows the ZnO NWs grown twice from the original NWs (**Figure 5.7b**). The NW length was increased from 12 μm to 20 μm, while the diameter increased from 150 nm to 250 nm. By repeating the hydrothermal process, over 50 μm long ZnO NW arrays could be grown.

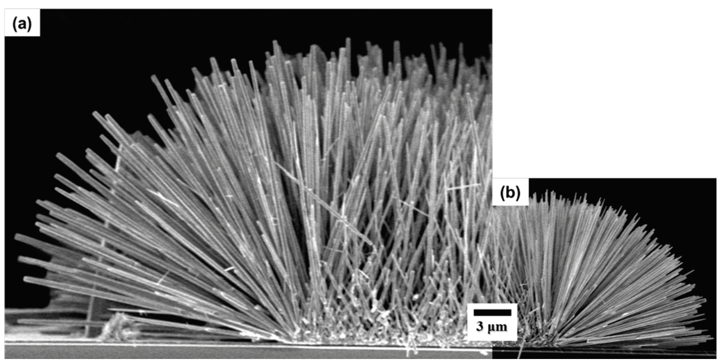

Figure 5.7 (a) Twice grown and (b) original initially grown ZnO NWs at the edge of the inkjet-printed NP seed.

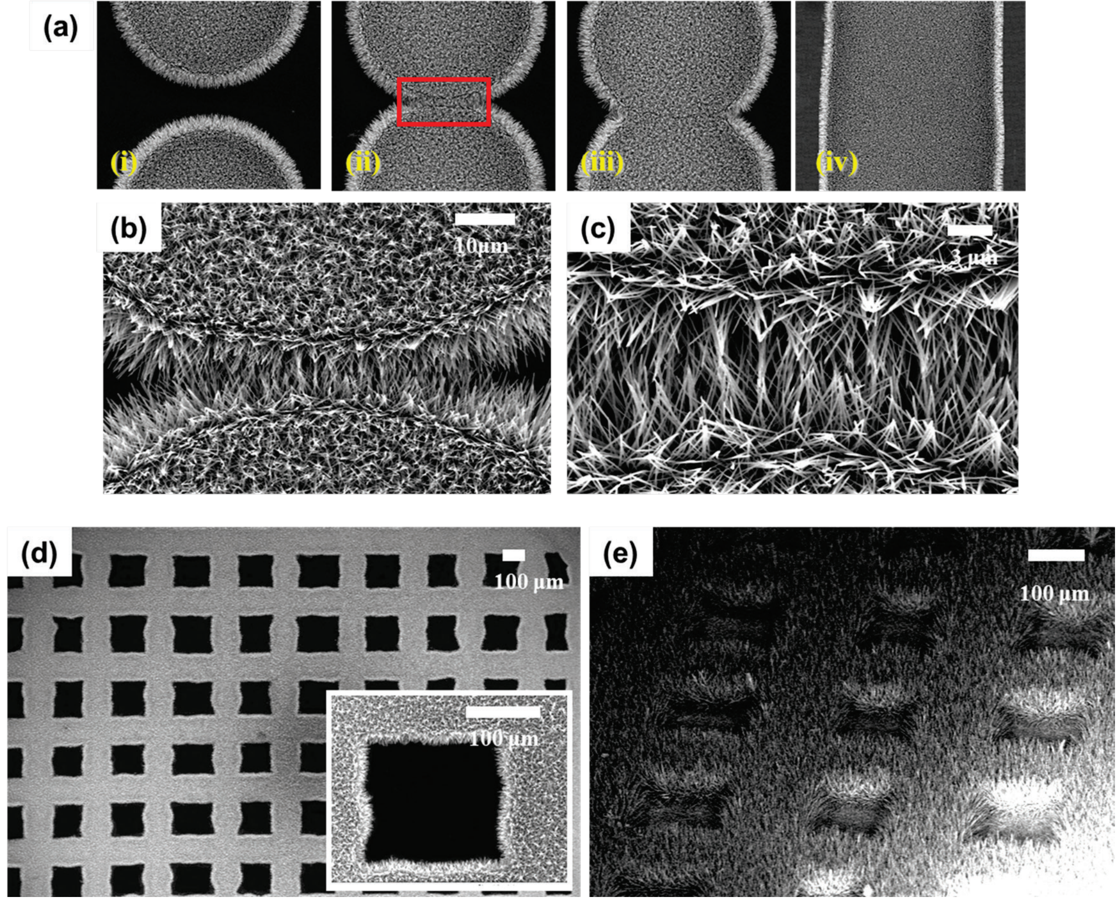

Figure 5.8 (a) SEM pictures of the ZnO NW growth at various droplet spacing; (b), (c) ZnO NW bridges between two circular ZnO NP seed droplets; (d) check shape ZnO NW growth; (e) 3 times grown check shape ZnO NW growth

Just like an office inkjet printer, ZnO seed NP inkjet printing process is a fully digital process enabling the arbitrary micro patterning from single micro-droplets with the CAD geometry data. When the overlapping between the inkjet-printed ZnO NP seed drops increases, ZnO NW array could be grown in a continuous line pattern (**Figure 5.8a**) or in a 2D checker pattern (**Figures 5.8(d,e)**). When the two droplets slightly touched, the urchin-like ZnO NWs meet to make NW bridges (**Figures 5.8(b,c)**).

All of the processes were carried out at low temperature under 95°C and no corrosive chemical etching or developing steps were applied. Therefore, the current process can be directly applied for the ZnO NW patterned growth on a polymer substrate. **Figure 5.9** shows line and dot patterned ZnO NW arrays on a polyimide substrate. This implies that current process can be applied for fabricating flexible electronics.

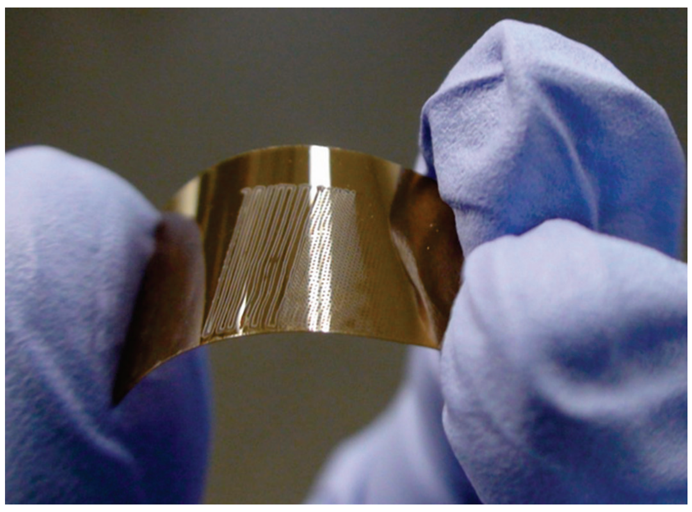

Figure 5.9 Line and dot patterned ZnO NW arrays on a plastic substrate (PI)

5.4 Conclusion

In conclusion, fully digital selective ZnO NW array growth on the inkjet-printed seed patterning was demonstrated. Through proper natural convection suppression during the hydrothermal growth, successful ZnO NW local growth could be achieved. Without any need for photolithographic process or stamp preparation, the NW growth location can be easily modified when the inkjet printing process is integrated with a CAD system to allow high degree of freedom when the design need to be changed. The herein proposed process is very fast, low cost, environmentally benign, and of low temperature. Therefore, it can be applied for flexible plastic substrate and scaled up to larger substrates for mass production or roll-to-roll process.

Chapter 6

Nanoforest composed of hydrothermally grown hierarchical ZnO NWs for a high efficiency dye-sensitized solar cell

As an application of ZnO NWs in optoelectronic devices, ZnO DSSCs with greatly enhanced surface area for higher dye loading and light harvesting were demonstrated. The selective growth of "*nanoforests*" composed of high-density, long branched tree-like multi generation hierarchical ZnO NW photoanodes by utilizing seed particles and a capping polymer increased the energy conversion efficiency significantly. A parametric study to determine optimum hierarchical ZnO NW photoanode was performed through the combination of both length-wise and branched growth processes.

6.1 Introduction

Dye sensitized solar cells (DSSCs) based on oxide semiconductors and organic dyes or metallorganic-complex dye have recently emerged as most promising candidate systems to achieve efficient solar-energy conversion since they are flexible, inexpensive, and easier to manufacture than silicon solar cells [158-160]. The DSSC is a photo-electro-chemical system that incorporates a porous-structured wide-bandgap oxide semiconductor (TiO_2 or ZnO) film as the photosensitized anode, hence offering increased surface area for dye molecule adsorption [160]. TiO_2 NPs [160, 161] or nanoporous structures [162, 163] have been most extensively studied as a DSSC photoelectrode material. The respective record high conversion efficiency (11.2%) has persisted for nearly two decades [164]. Further increase in the conversion efficiency has been limited by energy loss due to recombination between electrons and either the oxidized dye

molecules or electron-accepting species in the electrolyte during the charge transport processes [158, 165-167]. Such a recombination problem is more pronounced for TiO_2 nanocrystals due to the lack of a depletion layer on the TiO_2 nanocrystallite surface and becomes more serious when the photoelectrode film thickness increases [158].

To understand and solve this issue, ZnO based DSSC technology is considered. ZnO possesses energy band structure and physical properties similar to those of TiO_2, but its electron mobility is higher by 2~3 orders of magnitude [54]. Therefore, ZnO is expected to exhibit faster electron transport with reduced recombination loss. Although the conversion efficiencies (0.4~5.8%) obtained for ZnO are much lower than the maximum reported 11% for TiO_2, ZnO is still thought of as the most promising alternative to TiO_2 due to its ease of crystallization and anisotropic growth [158]. Functional nanostructured photoelectrodes such as 1D nanostructures (nanowires [12, 158, 159, 168] and nanotubes [158, 169], nanobelts [170], nanosheets [171, 172], nanotips [15]) have been extensively studied and could significantly improve the electron diffusion length in the photoelectrode films by providing a direct conduction pathway for the rapid collection of photogenerated electrons. Direct pathway along 1D crystalline nanostructures would diminish the possibility of charge recombination during interparticle percolation by replacing the conventional TiO_2 random polycrystalline NP network with ordered crystalline ZnO semiconductor NW. However, the insufficient surface area of simple 1D nanostructures constrains the energy conversion efficiency to relatively low levels (1.5% for ZnO NW DSSC [159]). Nanostructures combining multi-scale hierarchical configurations present increased surface area and hence higher energy conversion efficiency. Suh *et al*. [173] and Baxter *et al*. [174] have presented a dendritic ZnO NW DSSC. They grew ZnO NWs by expensive chemical vapor deposition (CVD) and showed relatively low efficiency (0.5 %) due to limited surface area. Jiang *et al*. [168] reported ZnO nanoflower photoanode and Cheng *et al.* [159] synthesized hierarchical ZnO NWs *via* a hydrothermal method. These hierarchical NWs were grown from seeds formed from $Zn(OAc)_2$ and still showed relatively low 1.5% efficiency, again due to insufficient surface area and also to the lack of uniformity of the secondary branches that were produced by the randomly distributed seed layer.

In this research, *"nanoforests"* of high density, long-branched tree-like multi generation hierarchical ZnO NW photoanodes is demonstrated. The *"nanoforests"* can significantly increase the energy conversion efficiency in its application for DSSCs. The efficiency increase is due to substantially enhanced surface area enabling higher dye loading and light harvesting, and also due to reduced charge recombination by direct conduction along the crystalline ZnO *"nanotree"* multi-generation branches. This approach mimics branched plant structures with the objective to capture more sunlight. A parametric study to improve the efficiency of hierarchical ZnO NW photoanodes by combining length-wise growth (LG) and branched growth (BG) are performed.

6.2 Synthesis of ZnO nanoforest

"*Nanoforests*" composed of hierarchical ZnO NWs are grown by a modified hydrothermal approach as illustrated in **Figure 6.1**. Depending on the growth conditions, two types of growth modes are observed; lengthwise growth (LG) and branched growth (BG). LG can yield ZnO NWs of increased length by extending the growth at the tip of the backbone ZnO NW. On the other hand, BG produces highly branched ZnO NWs by multiple generation hierarchical growth. As shown in **Figures 6.1(a,b)**, 1st generation (backbone) ZnO NWs were grown from ZnO dot seeds deposited on a substrate immersed in an aqueous precursor solution. ZnO dots (3~4 nm) were drop casted on a FTO glass substrate to form uniform seeds for ZnO NW growth. NWs were grown by immersing the seeded substrate into aqueous solutions. The synthesis details of quantum dots and 1st generation NW have been described in chapter 2. After the reaction was complete, the grown ZnO NWs were thoroughly rinsed with MilliQ water and dried in air to remove residual polymer. Longer ZnO NWs can be produced by repeating the hydrothermal growth process in a fresh aqueous precursor solution per the LG mode sketched in **Figure 6.1c**. Dramatic change in the ZnO NW structure could occur by heating the 1st generation ZnO NW at 350°C (10 mins), adding seed NPs and subsequently applying hydrothermal growth. Instead of LG, highly BG of ZnO NW on the sidewalls of the 1st generation ZnO NW could be observed (**Figure 6.1d**). It should be noted that BG differs from LG only in that it involves the presence of a heating step and a seeding step before the regular hydrothermal growth. The combination of multiple LG and BG steps can be applied for more complex hierarchical ZnO NW structuring.

While a single hydrothermal reaction LG process can produce 2~8 μm long, vertically aligned ZnO NWs (130~200 nm diameter), multiple LG growth steps can grow 40~50 μm long ZnO NWs of high aspect ratio (>100). **Figure 6.2a** displays ZnO NW after 1,2,3 LG steps. The length extension becomes smaller as the step order increases.

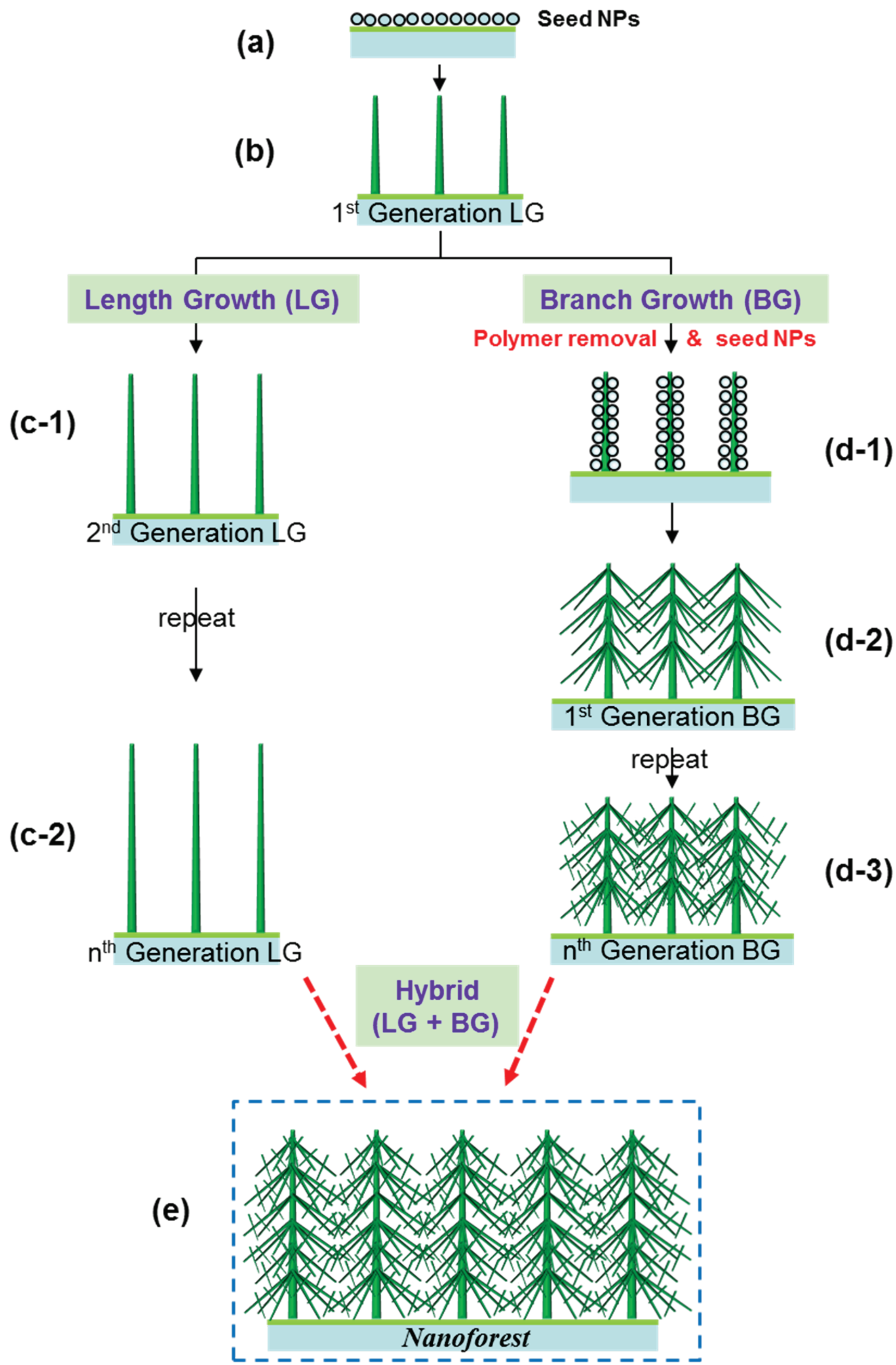

Figure 6.1 Two routes for hierarchical ZnO NW hydrothermal growth. Length growth (LG) (a-b-c), branched growth (BG) (a-b-d), and hybrid (a-b-c-d-e). Notice polymer removal and seed NPs for branched growth.

Vertically aligned, long ZnO NWs grown by multiple LG steps can be used as the backbone of the hierarchical branched ZnO NW forest. High quality hierarchical branched ZnO NW forest can be grown only after both (1) removal of polymer (HMTA, PEI) by heating the ZnO NW and (2) coating with seed NPs on the backbone ZnO NW surface. **Figures 6.2(b,c)** depict the "seed effect" and **Figures 6.2(d,e)** the "polymer removal effect".

HMTA and PEI hinder only lateral growth but allow axial growth of the ZnO NWs in the solution, thus yielding high aspect ratio NWs [12]. The polymer can be removed by heating the ZnO NWs at 350°C for 10 minutes. Branched growth (BG) that had been previously suppressed by HMTA and PEI during regular LG could be induced once the polymer was removed from the backbone NW, as shown in **Figure 6.2b**. In addition to random and sparsely branched NW growth on the side walls, the diameter of 1st generation backbone ZnO NW also increased (~1 μm) due to lateral growth after the removal of the HMTA and PEI polymer layer. After the polymer removal, seed NP coating on the 1st generation backbone NWs could induce growth of densely packed higher order generation BG while suppressing the diameter increase of the 1st generation backbone NW (**Figure 6.2c**).

Seed ZnO NP coating on the backbone ZnO NW without polymer removal could grow just sparsely branched ZnO NW (**Figure 6.2d**). In contrast, high quality hierarchical branched ZnO NW forest could be achieved by coating the backbone ZnO NW with seed ZNO NPs after the polymer removal (**Figure 6.2e**). ZnO NW growth from the seed NP on HMTA and PEI polymer may be less favorable than on the ZnO NW surface without polymer. This signifies that the polymer removal and the seed layer addition are important for realizing high-density hierarchical and branched ZnO NW forest growth.

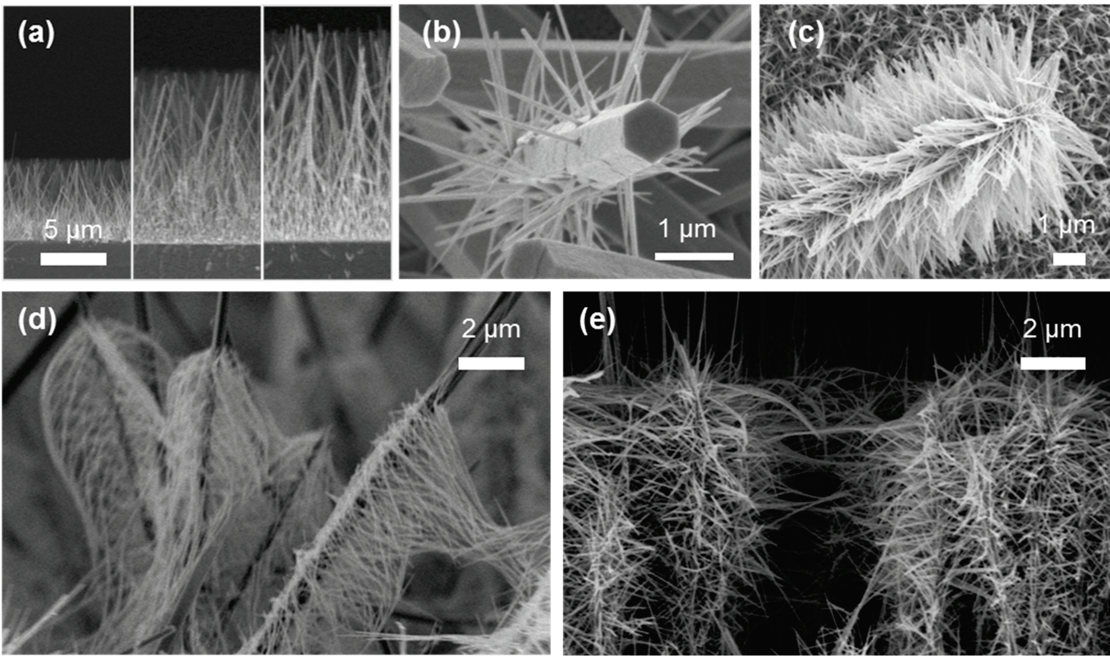

Figure 6.2 SEM pictures of ZnO NWs on FTO glass substrates. (a) Length growth (1,2,3 times growth). Seed effect: first generation branched growth (b) without seeds and (c) with seeds after polymer removal. Polymer removal effect: first generation branched growth (d) without polymer removal and (e) with polymer removal after seed NP deposition. Polymers on ZnO NW are removed after 350°C heating for 10 min.

"Nanoforest" of the hierarchical branched ZnO NW could be easily grown on a large area (**Figure 6.3a**) by a low cost, all solution processed hydrothermal method. The morphology of the ZnO NWs has been characterized by SEM. The tilted view (**Figure 6.3a**) and cross sectional images (**Figures 6.3(b,c)**) of the ZnO NWs suggest that the hierarchically branched ZnO NWs (blue dotted lines in **Figure 6.3c**) grow perpendicular to the vertically oriented 1st generation backbone ZnO NW surface (indicated by the red dotted lines in **Figure 6.3c**) . The length of branched ZnO NWs was 2~10 μm upon a single growth step and their diameter (**Figure 6.3d**) usually in the range of 30~50 nm, hence always much smaller than the diameter of 1st generation backbone ZnO NW (130~200 nm). This is attributed to the fact that branched ZnO NWs extend from the faces of the hexagonal backbone ZnO NWs. The BG NWs and the backbone ZnO NWs exhibit defined crystal orientation that is characteristic of CVD grown comb-like ZnO nanostructures [175, 176]. On the other hand, the hydrothermally grown secondary branched ZnO NW did not originate from the backbone NW but from ZnO seed NPs in the *c* axis direction of single wurtzite crystal [159].

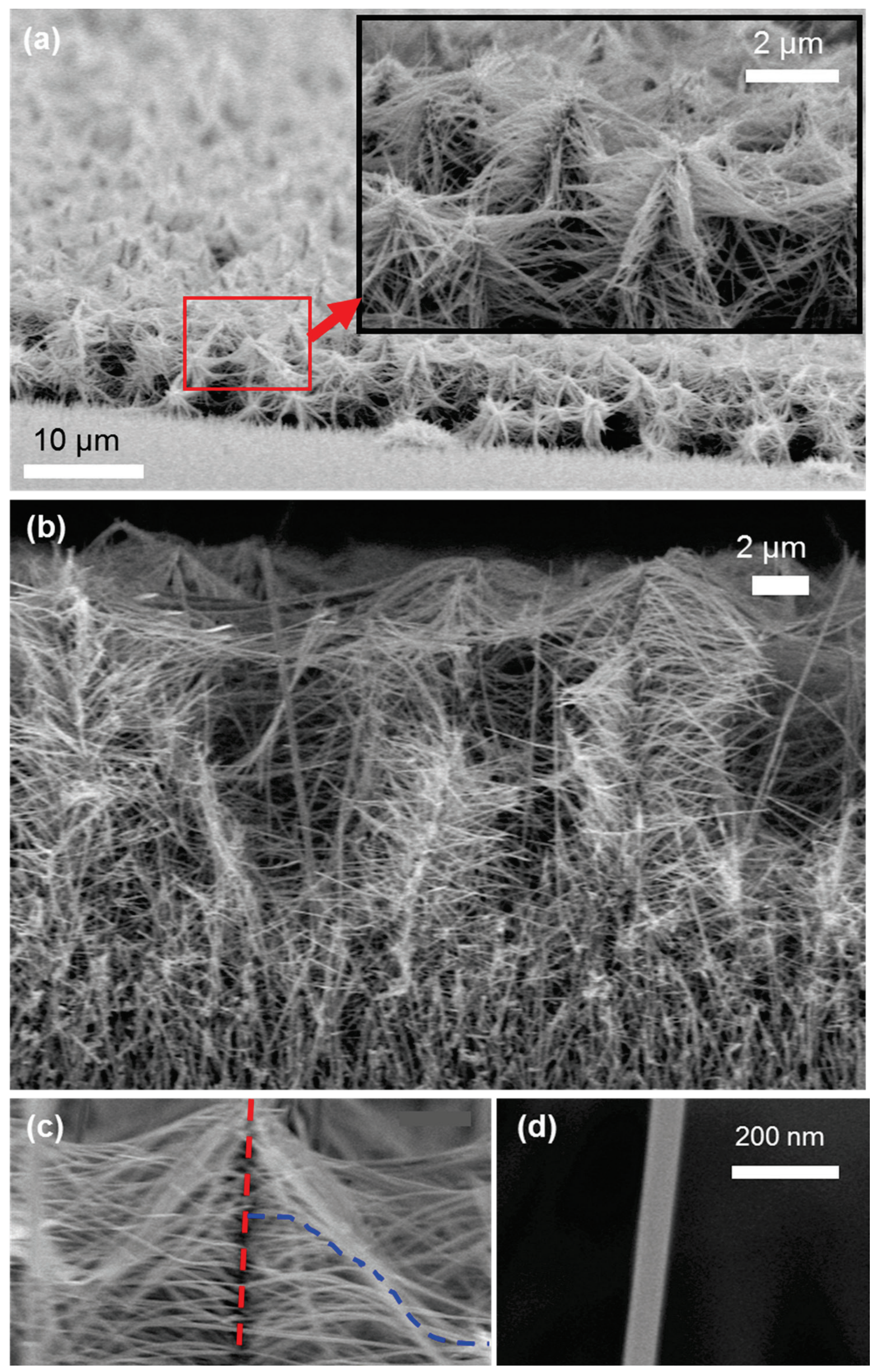

Figure 6.3 SEM pictures of ZnO NW nano-forest on a FTO glass substrate. (a) tilted view; (b) cross section view; (c) magnified view of backbone (red dotted line) and first generation branches (blue dotted line); (d) magnified view of a branch

6.3 DSSC performance

High efficiency DSSCs could be demonstrated from the densely branched ZnO NW *"nanoforest"* material on a FTO glass substrate (Hartford Inc.). **Figure 6.4a** shows the schematic picture of the DSSC and the SEM magnified picture of the ZnO NW *"nanoforest."* ZnO NWs were rinsed with DI water and baked in air at 350°C for 30 minutes to remove any residual organics and optimize solar cell performance [12]. ZnO NWs were sensitized in a solution of 0.5 mM cisbis(isothiocyanato)bis(2,2′-bipyridyl-4,4′-dicarboxylato)-ruthenium(II) bis-tetrabutylammonium (N719, Solaronix) in dry ethanol for 5 hours and then sandwiched together and bonded with platinum catalyst coated FTO counter electrodes separated by 40 μm thick hot melt foil spacer. The electrolyte solution (0.1 M LiI, 0.5 M 1,2-dimethyl-3-propylimidazolium iodide, 0.03 M I_2, and 0.5 M tert-butylpyridine in acetonitrile) [159] was introduced *via* capillary action into the gap formed by the two electrodes. The current density versus voltage (J-V) characteristic curves of the cells were measured under AM1.5G 100 $mW\cdot cm^{-2}$ illumination from a solar simulator (Newport) immediately after cell assembly.

Figure 6.4b shows the J-V characteristics for solar cells with both BG and LG ZnO nanostructures and the DSSC characteristics are summarized in **Table 6.1**. J-V curves for upstanding ZnO NW with various lengths (LG1: 7 μm, LG2: 13 μm, LG3: 16 μm) are presented in **Figure 6.4b**. The short circuit current density (J_{SC}) and the overall light conversion efficiency increased as the length of the LG ZnO NW increased (LG1: 0.45%, LG2: 0.7%, LG3: 0.85%). One-step branched growth on LG1 (7 μm) and LG2 (13 μm) yielded BG1 (from LG1) and BG2 (from LG2) and two-time branched growth produced BG3 (from LG2). By implementing additional NW generations, the short circuit current density (J_{SC}) and overall light conversion efficiency could be significantly increased for high density hierarchical branched ZnO NW *"nanoforest."* The respective enhancement was in the range of 350~500 % for the same backbone NW length (LG1: 0.45% to BG2: 2.22%, LG2: 0.71% to BG2: 2.51%). This is much higher than the reported values [159, 164] for hierarchical ZnO NW DSSCs and related to the substantial effective area increase by BG. The efficiency increase can be explained by considering a combination of several effects. First, the enhanced photon absorption associated with the augmented surface area results in increased dye loading and correspondingly to large J_{sc} increase. LG can grow only upstanding NWs by adding length to the 1st generation backbone NW. However, BG can grow multi-branched NWs from just a single 1st generation backbone NW to therefore increase dramatically surface area. The measured NW number density for upstanding LG NW (10^9 /cm^2) could be increased by 1~2 orders of magnitude ($10^{10\sim11}$ /cm^2) by BG NWs. Second, a dense network of crystalline ZnO NWs can increase the electron diffusion length and electron collection because the NW morphology provides more direct conduction paths for electron transport from the point of injection to the collection electrode. Third, randomly branched NWs promote enhanced light harvesting (light-dye interaction) without sacrificing efficient electron transport. In contrast, upstanding NWs are not favorable for light harvesting because photons could possibly travel between the vertical NWs without being absorbed by the dye [168]. Furthermore, branched NWs can increase light harvesting efficiency by

scattering enhancement and trapping [158]. The fill factor (FF) values for ZnO DSSCs are generally lower than those obtained using TiO_2 NPs (0.6-0.7). This is due to recombination between photoexcited carriers in the photoanodes and tri-iodide ions in the electrolyte. The FF may be enhanced by implementing dc or radio frequency magnetron sputtering and atomic layer deposition [159].

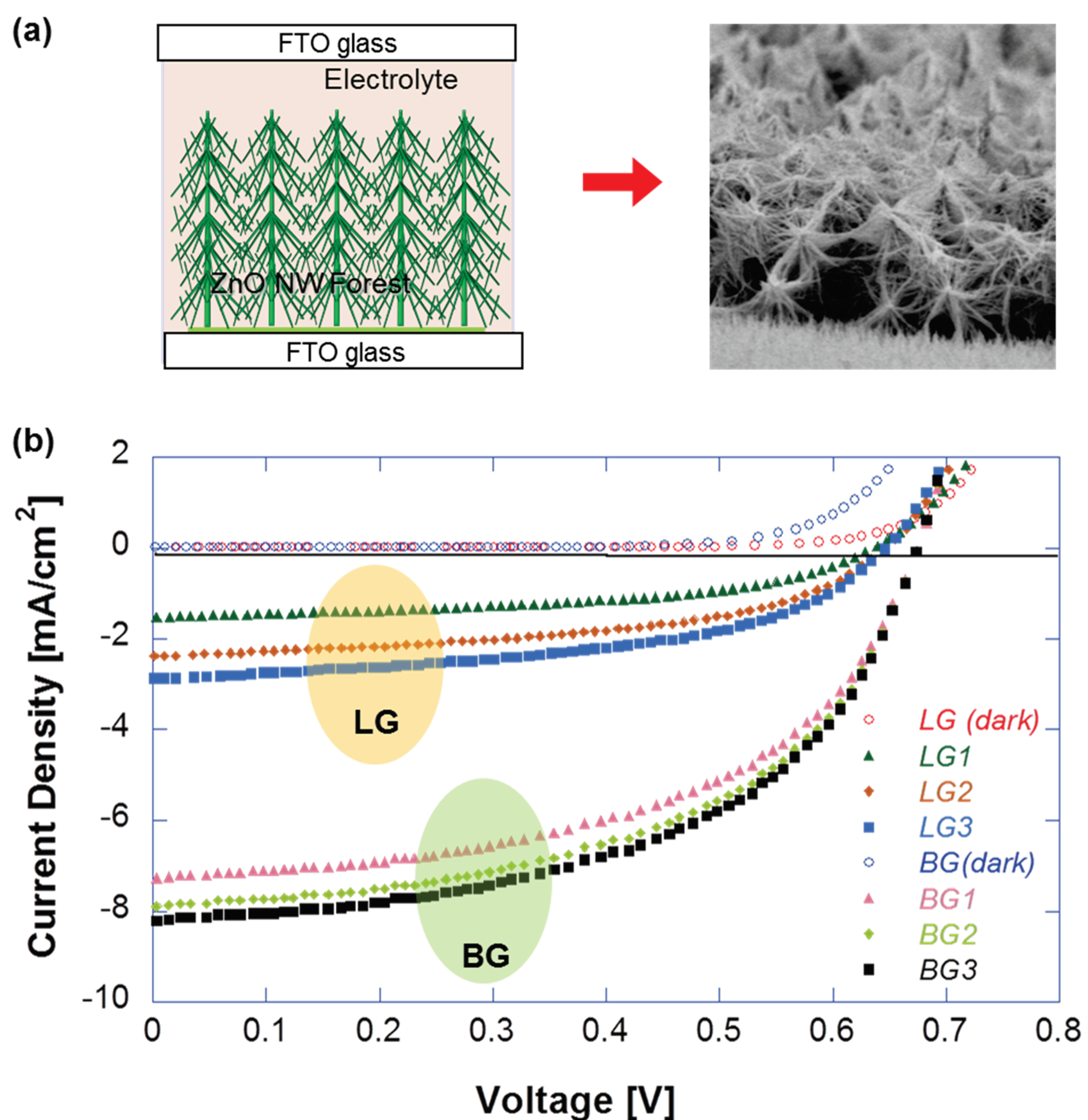

Figure 6.4 (a) Schematic structure; (b) J-V curve of dye-sensitized solar cell with "*nanoforest*" ZnO NW

Table 6.1 Characteristics of "*nanoforest*" ZnO DSSCs in **Figure 6.4b**.

	Backbone NW length	Branching times	Schematic Illustration	Efficiency [%]	J_{sc} [$mA \cdot cm^{-2}$]	V_{oc} [V]	FF
LG1	7			0.45	1.52	0.636	0.480
LG2	13	0 (only vertically grown NWs)		0.71	2.37	0.64	0.486
LG3	18			0.85	2.87	0.645	0.484
BG1	7			2.22	7.43	0.681	0.522
BG2		1		2.51	8.44	0.683	0.531
BG3	13	2		2.63	8.78	0.680	0.530

6.4 Conclusion

In summary, "*nanoforest*" of high density, long-branched tree-like multi-generation hierarchical crystalline ZnO NW photoanodes *via* a simple selective hierarchical growth sequence have been demonstrated and the structure could significantly improve the DSSC energy conversion efficiency. The short-circuit current density and overall light conversion efficiency of the branched ZnO NW DSSCs were almost 5 times higher than the efficiency of upstanding ZnO NWs. The efficiency increase is due to greatly augmented surface area enabling higher dye loading and light harvesting, as well as to reduced charge recombination through direct conduction along the crystalline ZnO multi-generation branches. A parametric study was performed to define hierarchical ZnO NW photoanodes consisting of various generation NWs through the combination of length-wise and branched growth. The new, simple and selective hierarchical growth is a low cost, all solution-processed hydrothermal method and can be used to fabricate complex hierarchical ZnO NW photoanodes by simple seed particle deposition steps and capping polymer engineering. The low temperature process nature carries substantial potential for further developing DSSCs on low-cost, large-area flexible polymer substrates.

Chapter 7

Conclusions of the present work

In the previous chapters, substantial steps have been taken towards developing ZnO NP synthesis, laser processing, deposition and patterning methods for the fabrication of both passive and active ZnO components. In a striking departure from conventional methods such as vacuum-based thin film deposition, pattern generation by mask-involved photolithographic processes and e-beam lithography mold fabrication for the nanoimprinting, solution-processible nanomaterials were successfully combined with direct writing technology in an effective way.

A very well-dispersed, transparent and concentration-tunable ZnO NPs solution was synthesized in a new process (chapter 2). ZnO NPs did not agglomerate in the 1-pentanol solution without incorporating additional chemicals for a capping layer. Highly transparent ZnO thin films were fabricated by spin coating and subsequent ultra short-pulsed UV laser annealing was performed to change the film properties (chapter 3). While as-deposited NP thin films were not electrically conductive, laser annealing imparted a substantial conductivity increase. Thus, selective annealing for conductive patterns directly on the NP thin film without a photolithographic process was achieved. With optimized laser annealing parameters, undoped ZnO thin film of 4.75×10^{-2} $\Omega\cdot$cm resistivity was attained. The resistivity is by a factor of 10^5 lower than that of the previously reported furnace-annealed ZnO NP films and is even comparable to that of vacuum-deposited, impurity-doped ZnO films within a factor of 10. The process developed in this work has been applied to the fabrication of a TFT device exhibiting enhanced performance compared with the one that fabricated with the furnace annealed ZnO film. The ZnO TFT performance test revealed that by just changing the laser annealing parameters the solution-deposited ZnO thin film properties could be tuned and rendered suitable for both transparent conductors and semiconductor active layers.

Two kinds of nanomaterial patterning methods *via* direct writing have been demonstrated. First, laser-assisted nanoimprinting of metal and semiconductor NPs has been presented as a large area one step patterning method (chapter 4). With this method, submicron structures including mesh, line, nanopillar and NW arrays were fabricated on various kinds of wafer scale substrates. Using the rapid laser-based nanolithography,

constraints of e-beam patterning could be overcome, enabling rapid mold fabrication. Therefore, the presented method opens a way to the fabrication of electronic and energy devices with high throughput and ultra low-cost. The fabrication was completely free of lift-off or RIE processes. PDMS stamp fabricated from the master mold replicated nanoscale structures down to 200 nm. The NP printing time with the PDMS stamp takes only several tens of seconds and can be further reduced with optimized process parameters. Design parameters such as depth, height, and pattern shapes can be easily changed, controlled and optimized. The low temperature and low pressure used in nanoimprinting process enable direct nanofabrication on various substrates including flexible substrates. Second, inkjet printing of ZnO seed layers for a fully digital selective ZnO NW array growth has been discussed (chapter 5). Through proper natural convection suppression during the hydrothermal growth, localized ZnO NW growth was achieved. Without any need for the photolithographic process or stamp preparation, the NW growth location can be easily modified when the inkjet printing process is integrated with CAD system to allow high degree of freedom when the design must be changed. The proposed process is very fast, low cost, environmentally benign, and performed under low temperature. Therefore it can be applied for flexible plastic substrates and scaled up for larger substrate for mass production or roll-to-roll process.

As an application of ZnO nanomaterials for high efficiency solar cells, the selective growth of *"nanoforests"* composed of high-density, long branched tree-like multi-generation hierarchical ZnO NW photoanodes has been developed for ZnO DSSCs (chapter 6). The new and selective hierarchical growth approach represents a low cost, all solution processed hydrothermal method that yields complex ZnO NW photoanodes by utilizing seed particles and a capping polymer. The overall light-conversion efficiency of the branched ZnO NW DSSCs was almost 5 times higher than the efficiency of DSSCs constructed by upstanding ZnO NWs. The efficiency increase achieved by introducing branched growth is attributed to the surface area increase that allows higher dye loading and light harvesting and also to the reduced charge recombination through direct conduction along the crystalline ZnO branches.

Chapter 8

Recommendation for future study

ZnO applications as transparent conductive electrodes are usually achieved through vacuum-based deposition method with impurity doping such as AZO and GZO. Even though several research papers regarding the synthesis of solution processible impurity doped-ZnO NP have been reported, no apparent applications have been reported so far [177, 178]. Finding an effective way to produce impurity-doped ZnO NP solution combined with successive laser annealing process would yield transparent metal oxide films with conductivity equivalent to that of ITO. Another intriguing issue in TCO materials development is the synthesis of p-type nanomaterials. For p–n junction optoelectronic device applications, such as LED, TFTs, and solar cells, p-type TCOs are indispensable. However, well-known TCOs such as ITO, FTO, AZO and GZO are all n-type semiconductors. Even though there have been many reported attempts to produce p-type TCO materials such as nitrogen-doped ZnO [179, 180], MoO3 [181], NiO [182], their use is rather limited due to either difficulty in synthesis or high temperature processes involved or a short life time. Admittedly, p-type doping of ZnO remains a great challenge due to several reasons, including the deep donor level, low solubility of the dopants and the inducing of self-compensating processes on doping. Several researchers, however, have shown the possibility of producing p-type ZnO by pulsed laser deposition with varying annealing gas conditions to force dopants such as nitrogen and phosphorous into the lattice [180, 183]. Adapting pulsed laser annealing in varying annealing environment offers a promising route towards solving the aforementioned long-standing issues to spearhead numerous applications in the field of optoelectronic devices.

Laser-assisted large area imprinting method has substantial potential for applications in solar cells. Submicron structures including mesh, line and nanopillar arrays can be applied for the surface texturing of solar cell components [184-186]. Imprinting semiconductor nanomaterials such as ZnO, ITO, TiO_2 and Si NPs can generate structured light trapping TCO layer or absorbing layer that will increase the device efficiency. Furthermore, nanoimprinting of metals such as Ag, Au, Al and Cu can be applied to realize plasmonic solar cell structures [187]. Due to the additive nature of

nanoimprinting, the process is not limited to the thickness, composition or chemical characteristics of as-deposited films and can be applied to ultra-thin films that cannot be textured by etching processes. Furthermore, it can be used to construct, texture and functionalize multi-layers composed of different materials. The resolution of the imprinted nanostructure would be enhanced by further optimization of optical and chemical components. Another possible pathway is taking advantage of nonlinear multi-photon ultrafast laser processing to fabricate a mold for nanoimprinting. Sub-100 nm scale feature resolution using femtosecond laser could be delivered *via* far field optics [144]. Recently, it has been reported that the morphology and orientation of organic thin films have been significantly altered through nanoimprinted grooves of around 100 nm spacing [188]. In organic solar cells, the electrical and optical properties of the polymer semiconducting materials are often not isotropic since these properties are directly dependent on the molecular orientations of the polymer chains [188]. By optimizing the orientation and crystalline properties of conducting polymers, significant improvement in organic solar cell performance is expected. Inorganic-organic hybrid structures are another possible applications of the NP nanoimprinting method. Inorganic-organic hybrid structures have been reported to achieve enhanced performance [189]. With the advantage of laser assisted nanoimprinting method, scaled-up devices containing various hybrid structures can be developed.

High-density, long branched tree-like multi generation hierarchical crystalline photoanodes can be implemented for structuring TiO_2 NW photoanodes. Recently, it has been reported in several research papers [190, 191] that hierarchical TiO_2 photoanodes could improve the solar cell conversion efficiency. However, real tree-like TiO2 nanostructures featuring long braches have not been successfully demonstrated and there is still plenty of room for improvement. Besides optimizing the selective hierarchical growth, directed patterning of the seed layers and the 3-D structuring of the electrodes by successive nanoimprinting will provide another possibility for attaining highly efficient photoanodes.

References

[1] Ellmer K, Klein A, Rech B. Transparent conductive zinc oxide: Springer; 2007.
[2] Jagadish C, Pearton SJ. Zinc oxide bulk, thin films and nanostructures: processing, properties and applications: Elsevier Science; 2006.
[3] Ozgur U, Alivov YI, Liu C, Teke A, Reshchikov MA, Dogan S, et al. A comprehensive review of ZnO materials and devices. Journal of Applied Physics. 2005;98.
[4] Monemar B. Fundamental energy gap of GaN from photoluminescence excitation spectra. Physical Review B. 1974;10:676.
[5] Satoh I, Kobayashi T, Katayama K, Okada T, Itoh T. Magneto-photoluminescence of novel magnetic semiconductor Zn 1-x Cr x O grown by PLD method. Applied Physics A: Materials Science & Processing. 2004;79:1445-7.
[6] Yoshino Y, Makino T, Katayama Y, Hata T. Optimization of zinc oxide thin film for surface acoustic wave filters by radio frequency sputtering. Vacuum. 2000;59:538-45.
[7] Gorla CR, Emanetoglu NW, Liang S, Mayo WE, Lu Y, Wraback M, et al. Structural, optical, and surface acoustic wave properties of epitaxial ZnO films grown on (01(1)over-bar2) sapphire by metalorganic chemical vapor deposition. Journal of Applied Physics. 1999;85:2595-602.
[8] Grate JW, Martin SJ, White RM. Acoustic wave microsensors. Analytical Chemistry. 1993;65:940-8.
[9] Hickernell FS. Zinc-oxide films for acoustoelectric device applicaitons. Ieee Transactions on Sonics and Ultrasonics. 1985;32:621-9.
[10] Pacholski C, Kornowski A, Weller H. Self-assembly of ZnO: from nanodots to nanorods. Angewandte Chemie International Edition. 2002;41:1188-91.
[11] Sun B, Sirringhaus H. Solution-processed zinc oxide field-effect transistors based on self-assembly of colloidal nanorods. Nano Letters. 2005;5:2408-13.
[12] Law M, Greene LE, Johnson JC, Saykally R, Yang P. Nanowire dye-sensitized solar cells. Nature materials. 2005;4:455-9.
[13] Vayssieres L. Growth of arrayed nanorods and nanowires of ZnO from aqueous solutions. Advanced Materials. 2003;15:464-6.
[14] Xing Y, Xi Z, Zhang X, Song J, Wang R, Xu J, et al. Nanotubular structures of zinc oxide. Solid state communications. 2004;129:671-5.
[15] Wang ZL. Zinc oxide nanostructures: growth, properties and applications. Journal of Physics: Condensed Matter. 2004;16:R829.
[16] Wang ZL. Nanostructures of zinc oxide. Materials today. 2004;7:26-33.

[17] Wang ZL. Piezoelectric nanostructures: from growth phenomena to electric nanogenerators. MRS bulletin. 2007;32:109-16.
[18] Wang X, Song J, Wang ZL. Nanowire and nanobelt arrays of zinc oxide from synthesis to properties and to novel devices. Journal of Materials Chemistry. 2007;17:711-20.
[19] Vayssieres L, Keis K, Lindquist S-E, Hagfeldt A. Purpose-built anisotropic metal oxide material: 3D highly oriented microrod array of ZnO. The Journal of Physical Chemistry B. 2001;105:3350-2.
[20] Huang MH, Mao S, Feick H, Yan HQ, Wu YY, Kind H, et al. Room-temperature ultraviolet nanowire nanolasers. Science. 2001;292:1897-9.
[21] Yang PD, Yan HQ, Mao S, Russo R, Johnson J, Saykally R, et al. Controlled growth of ZnO nanowires and their optical properties. Advanced Functional Materials. 2002;12:323-31.
[22] Wan Q, Yu K, Wang TH, Lin CL. Low-field electron emission from tetrapod-like ZnO nanostructures synthesized by rapid evaporation. Applied Physics Letters. 2003;83:2253-5.
[23] Willander M, Nur O, Zhao QX, Yang LL, Lorenz M, Cao BQ, et al. Zinc oxide nanorod based photonic devices: recent progress in growth, light emitting diodes and lasers. Nanotechnology. 2009;20.
[24] Bao J, Zimmler MA, Capasso F, Wang X, Ren ZF. Broadband ZnO single-nanowire light-emitting diode. Nano Letters. 2006;6:1719-22.
[25] Kim H, Gilmore CM, Horwitz JS, Pique A, Murata H, Kushto GP, et al. Transparent conducting aluminum-doped zinc oxide thin films for organic light-emitting devices. Applied Physics Letters. 2000;76:259-61.
[26] Konenkamp R, Word RC, Schlegel C. Vertical nanowire light-emitting diode. Applied Physics Letters. 2004;85:6004-6.
[27] Tsukazaki A, Ohtomo A, Onuma T, Ohtani M, Makino T, Sumiya M, et al. Repeated temperature modulation epitaxy for p-type doping and light-emitting diode based on ZnO. Nature Materials. 2005;4:42-6.
[28] Soares JW, Steeves DM, Ziegler D, DeCristofano BS. Surface modification of nanocrystalline zinc oxide for bio-sensing applications. Proceedings of the SPIE - The International Society for Optical Engineering. 2006;6370.
[29] Willander M, Nur O, Fakhar-e-Alam M, Sadaf JR, Israr MQ, Sultana K, et al. Applications of zinc oxide nanowires for bio-photonics and bio-electronics. Proceedings of the SPIE - The International Society for Optical Engineering. 2011;7940.
[30] Lee D, Pan H, Ko SH, Park HK, Kim E, Grigoropoulos CP. Non-vacuum, single-step conductive transparent ZnO patterning by ultra-short pulsed laser annealing of solution-deposited nanoparticles. Applied Physics A: Materials Science & Processing. 2012:1-11.
[31] Lewis JA, Gratson GM. Direct writing in three dimensions. Materials today. 2004;7:32-9.
[32] Ko SH, Pan H, Grigoropoulos CP, Luscombe CK, Fréchet JMJ, Poulikakos D. All-inkjet-printed flexible electronics fabrication on a polymer substrate by low-temperature high-resolution selective laser sintering of metal nanoparticles. Nanotechnology. 2007;18:345202.

[33] Jin AJ, Jinho L, Hongdoo K, Han-Ki K, Seok-In N. Ink-jet printed transparent electrode using nano-size indium tin oxide particles for organic photovoltaics. Solar Energy Materials and Solar Cells. 2010;94:1840-4.
[34] Ko SH, Lee D, Hotz N, Yeo J, Hong S, Nam KH, et al. "Digital" selective growth of ZnO nanowire arrays from inkjet printed nanoparticle seed on a flexible substrate. Langmuir. 2011.
[35] Pan H, Ko SH, Misra N, Grigoropoulos CP. Laser annealed composite titanium dioxide electrodes for dye-sensitized solar cells on glass and plastics. Applied physics letters. 2009;94:071117--3.
[36] Ko SH, Pan H, Lee D, Grigoropoulos CP, Park HK. Nanoparticle selective laser processing for a flexible display fabrication. Japanese Journal of Applied Physics. 2010;49.
[37] Thiel M, Fischer J, Von Freymann G, Wegener M. Direct laser writing of three-dimensional submicron structures using a continuous-wave laser at 532 nm. Applied physics letters. 2010;97:221102.
[38] Lee M-T, Lee D, Sherry A, Grigoropoulos CP. Rapid selective metal patterning on polydimethylsiloxane (PDMS) fabricated by capillarity-assisted laser direct write. Journal of Micromechanics and Microengineering. 2011;21.
[39] Pan H, Lee D, Ko SH, Grigoropoulos CP, Park HK, Hoult T. Fiber laser annealing of indium-tin-oxide nanoparticles for large area transparent conductive layers and optical film characterization. Applied Physics A: Materials Science & Processing. 2011:1-10.
[40] Bao ZN, Feng Y, Dodabalapur A, Raju VR, Lovinger AJ. High-performance plastic transistors fabricated by printing techniques. Chemistry of Materials. 1997;9:1299-&.
[41] Krebs FC, Jorgensen M, Norrman K, Hagemann O, Alstrup J, Nielsen TD, et al. A complete process for production of flexible large area polymer solar cells entirely using screen printing-First public demonstration. Solar Energy Materials and Solar Cells. 2009;93:422-41.
[42] Krebs FC. Polymer solar cell modules prepared using roll-to-roll methods: Knife-over-edge coating, slot-die coating and screen printing. Solar Energy Materials and Solar Cells. 2009;93:465-75.
[43] SIRRINGHAUS H. Solid state embossing of polymer devices. WO Patent WO/2002/029,912; 2002.
[44] Stutzmann N, Tervoort T, Bastiaansen CWM, Feldman K, Smith P. Solid-state replication of relief structures in semicrystalline polymers. Advanced Materials. 2000;12:557-62.
[45] Stutzmann N, Tervoort TA, Bastiaansen K, Smith P. Patterning of polymer-supported metal films by microcutting. Nature. 2000;407:613-6.
[46] Piner RD, Zhu J, Xu F, Hong SH, Mirkin CA. "Dip-pen" nanolithography. Science. 1999;283:661-3.
[47] Demers LM, Ginger DS, Park SJ, Li Z, Chung SW, Mirkin CA. Direct patterning of modified oligonucleotides on metals and insulators by dip-pen nanolithography. Science. 2002;296:1836-8.
[48] Ginger DS, Zhang H, Mirkin CA. The evolution of dip-pen nanolithography. Angewandte Chemie-International Edition. 2004;43:30-45.

[49] Adrian FJ, Bohandy J, Kim BF, Jette AN, Thompson P. A study of the mechanism of metal-deposition by the laser-induced forward transfer process. Journal of Vacuum Science & Technology B. 1987;5:1490-4.
[50] Bohandy J, Kim B, Adrian F, Jette A. Metal deposition at 532 nm using a laser transfer technique. Journal of Applied Physics. 1988;63:1158-62.
[51] van Kan JA, Bettiol AA, Watt F. Three-dimensional nanolithography using proton beam writing. Applied Physics Letters. 2003;83:1629-31.
[52] Tseng AA. Recent developments in nanofabrication using focused ion beams. Small. 2005;1:924-39.
[53] Hon K, Li L, Hutchings I. Direct writing technology--Advances and developments. CIRP Annals-Manufacturing Technology. 2008;57:601-20.
[54] Pan H, Misra N, Ko SH, Grigoropoulos CP, Miller N, Haller EE, et al. Melt-mediated coalescence of solution-deposited ZnO nanoparticles by excimer laser annealing for thin-film transistor fabrication. Applied Physics a-Materials Science & Processing. 2009;94:111-5.
[55] Farhoud M, Ferrera J, Lochtefeld AJ, Murphy T, Schattenburg ML, Carter J, et al. Fabrication of 200 nm period nanomagnet arrays using interference lithography and a negative resist. Journal of Vacuum Science & Technology B: Microelectronics and Nanometer Structures. 1999;17:3182-5.
[56] Lee W, Ji R, Ross CA, Gösele U, Nielsch K. Wafer-Scale Ni Imprint Stamps for Porous Alumina Membranes Based on Interference Lithography. Small. 2006;2:978-82.
[57] Ko SH, Park I, Pan H, Grigoropoulos CP, Pisano AP, Luscombe CK, et al. Direct nanoimprinting of metal nanoparticles for nanoscale electronics fabrication. Nano letters. 2007;7:1869-77.
[58] Lee D, Pan H, Sherry A, Ko SH, Lee M-T, Kim E, et al. Large area nanoimprinting on various substrates by reconfigurable maskless laser direct writing. Nanotechnology. 2012 (accepted).
[59] Le HP. Progress and trends in ink-jet printing technology. The Journal of imaging science and technology. 1998;42:49-62.
[60] Spanhel L, Anderson MA. Semiconductor clusters in the sol-gel process: quantized aggregation, gelation, and crystal growth in concentrated zinc oxide colloids. Journal of the American Chemical Society. 1991;113:2826-33.
[61] Vafaee M, Ghamsari MS. Preparation and characterization of ZnO nanoparticles by a novel sol–gel route. Materials letters. 2007;61:3265-8.
[62] Music S, Dragčević Đ, Popović S, Ivanda M. Precipitation of ZnO particles and their properties. Materials letters. 2005;59:2388-93.
[63] Mueller R, Mädler L, Pratsinis SE. Nanoparticle synthesis at high production rates by flame spray pyrolysis. Chemical engineering science. 2003;58:1969-76.
[64] Suyama Y, Takemiya S, Kato A. Synthesis of ultrafine ZnO powders by vapour phase oxidation of Zn vapour. Journal of the Ceramic Society of Japan. 1985;93:105.
[65] Hu PA, Liu YQ, Fu L, Wang XB, Zhu DB. Creation of novel ZnO nanostructures: self-assembled nanoribbon/nanoneedle junction networks and faceted nanoneedles on hexagonal microcrystals. Applied Physics A: Materials Science & Processing. 2004;78:15-9.

[66] Kumar S, Gupta V, Sreenivas K. Synthesis of photoconducting ZnO nano-needles using an unbalanced magnetron sputtered ZnO/Zn/ZnO multilayer structure. Nanotechnology. 2005;16:1167.
[67] Hirate T, Sasaki S, Li W, Miyashita H, Kimpara T, Satoh T. Effects of laser-ablated impurity on aligned ZnO nanorods grown by chemical vapor deposition. Thin Solid Films. 2005;487:35-9.
[68] Wang D, Song C. Controllable synthesis of ZnO nanorod and prism arrays in a large area. The Journal of Physical Chemistry B. 2005;109:12697-700.
[69] Greene LE, Yuhas BD, Law M, Zitoun D, Yang P. Solution-grown zinc oxide nanowires. Inorganic chemistry. 2006;45:7535-43.
[70] Kim JH, Andeen D, Lange FF. Hydrothermal growth of periodic, single-crystal ZnO microrods and microtunnels. Advanced Materials. 2006;18:2453-7.
[71] Beek WJE, Wienk MM, Janssen RAJ. Efficient hybrid solar cells from zinc oxide nanoparticles and a conjugated polymer. Advanced Materials. 2004;16:1009-13.
[72] Kim D, Jeong S, Moon J. Synthesis of silver nanoparticles using the polyol process and the influence of precursor injection. Nanotechnology. 2006;17:4019.
[73] Lee MT, Lee D, Sherry A, Grigoropoulos CP. Rapid selective metal patterning on polydimethylsiloxane (PDMS) fabricated by capillarity-assisted laser direct write. Journal of Micromechanics and Microengineering. 2011;21:095018.
[74] Lee Y, Choi J, Lee KJ, Stott NE, Kim D. Large-scale synthesis of copper nanoparticles by chemically controlled reduction for applications of inkjet-printed electronics. Nanotechnology. 2008;19:415604.
[75] Plummer JD, Deal MD, Griffin PB. Silicon VLSI technology: fundamentals, practice and modeling: Prentice Hall Upper Saddle River, NJ; 2000.
[76] Ohyama M, Kozuka H, Yoko T. Sol-gel preparation of ZnO films with extremely preferred orientation along (002) plane from zinc acetate solution. Thin Solid Films. 1997;306:78-85.
[77] Ying Z, Weibing W, Guangda H, Haitao W, Shougang C. Hydrothermal synthesis of ZnO nanorod arrays with the addition of polyethyleneimine. Mater Res Bull. 2008;43:2113-21182118.
[78] Wu W, Hu G, Cui S, Zhou Y, Wu H. Epitaxy of vertical ZnO nanorod arrays on highly (001)-oriented ZnO seed monolayer by a hydrothermal route. Crystal Growth & Design. 2008;8:4014-20.
[79] Yang W, Wan F, Chen S, Jiang C. Hydrothermal growth and application of ZnO nanowire films with ZnO and TiO2 buffer layers in dye-sensitized solar cells. Nanoscale Research Letters. 2009;4:1486-92.
[80] Greene LE, Law M, Goldberger J, Kim F, Johnson JC, Zhang Y, et al. Low-temperature wafer-scale production of ZnO nanowire arrays. Angewandte Chemie International Edition. 2003;42:3031-4.
[81] Ko SH, Lee D, Kang HW, Nam KH, Yeo JY, Hong SJ, et al. Nanoforest of hydrothermally grown hierarchical ZnO nanowires for a high efficiency dye-sensitized solar cell. Nano Letters. 2011;11:666-71.
[82] Xu S, Adiga N, Ba S, Dasgupta T, Wu CFJ, Wang ZL. Optimizing and improving the growth quality of ZnO nanowire arrays guided by statistical design of experiments. ACS Nano. 2009;3:1803-12.

[83] Ray S, Banerjee R, Basu N, Batabyal A, Barua A. Properties of tin doped indium oxide thin films prepared by magnetron sputtering. Journal of Applied Physics. 1983;54:3497-501.
[84] Tahar RBH, Ban T, Ohya Y, Takahashi Y. Tin doped indium oxide thin films: Electrical properties. Journal of Applied Physics. 1998;83:2631-45.
[85] Granqvist C, Hultaker A. Transparent and conducting ITO films: new developments and applications. Thin Solid Films. 2002;411:1-5.
[86] Minami T, Ida S, Miyata T. High rate deposition of transparent conducting oxide thin films by vacuum arc plasma evaporation. Thin Solid Films. 2002;416:92-6.
[87] Zhu BL, Zeng DW, Wu J, Song WL, Xie CS. Synthesis and gas sensitivity of In-doped ZnO nanoparticles. Journal of Materials Science-Materials in Electronics. 2003;14:521-6.
[88] Keunbin Y, Chongmu L. Dependence of the electrical and optical properties of sputter-deposited ZnO:Ga films on the annealing temperature, time, and atmosphere. Journal of Materials Science: Materials in Electronics. 2007;18:385-90.
[89] Park SH, Park JB, Song PK. Characteristics of Al-doped, Ga-doped and In-doped zinc-oxide films as transparent conducting electrodes in organic light-emitting diodes. Curr Appl Phys. 2010;10:S488-S90.
[90] Bisht H, Eun HT, Mehrtens A, Aegerter MA. Comparison of spray pyrolyzed FTO, ATO and ITO coatings for flat and bent glass substrates. Thin Solid Films. 1999;351:109-14.
[91] Fukano T, Motohiro T. Low-temperature growth of highly crystallized transparent conductive fluorine-doped tin oxide films by intermittent spray pyrolysis deposition. Solar Energy Materials and Solar Cells. 2004;82:567-75.
[92] Chang H, Wang G, Yang A, Tao X, Liu X, Shen Y, et al. A transparent, flexible, low-Temperature, and solution-processible graphene composite electrode. Advanced Functional Materials. 2010;20:2893-902.
[93] Jang S, Jang H, Lee Y, Suh D, Baik S, Hong BH, et al. Flexible, transparent single-walled carbon nanotube transistors with graphene electrodes. Nanotechnology. 2010;21.
[94] Jo JW, Jung JW, Lee JU, Jo WH. Fabrication of highly conductive and transparent thin films from single-walled carbon nanotubes using a new non-ionic surfactant via spin coating. ACS Nano. 2010;4:5382-8.
[95] Shim BS, Zhu JA, Jan E, Critchley K, Kotov NA. Transparent conductors from layer-by-layer assembled SWNT films: importance of mechanical properties and a new figure of merit. ACS Nano. 2010;4:3725-34.
[96] Kim KH, Park KC, Ma DY. Structural, electrical and optical properties of aluminum doped zinc oxide films prepared by radio frequency magnetron sputtering. Journal of Applied Physics. 1997;81:7764-72.
[97] Cebulla R, Wendt R, Ellmer K. Al-doped zinc oxide films deposited by simultaneous rf and dc excitation of a magnetron plasma: Relationships between plasma parameters and structural and electrical film properties. Journal of Applied Physics. 1998;83:1087-95.
[98] Carcia PF, McLean RS, Reilly MH, Nunes G. Transparent ZnO thin-film transistor fabricated by rf magnetron sputtering. Applied Physics Letters. 2003;82:1117-9.

[99] Matsubara K, Fons P, Iwata K, Yamada A, Sakurai K, Tampo H, et al. ZnO transparent conducting films deposited by pulsed laser deposition for solar cell applications. Thin Solid Films. 2003;431:369-72.
[100] Ozerov I, Nelson D, Bulgakov AV, Marine W, Sentis M. Synthesis and laser processing of ZnO nanocrystalline thin films. Appl Surf Sci. 2003;212:349-52.
[101] Gupta V, Mansingh A. Influence of postdeposition annealing on the structural and optical properties of sputtered zinc oxide film. Journal of Applied Physics. 1996;80:1063-73.
[102] Minami T. Present status of transparent conducting oxide ing oxide thin-film development for Indium-Tin-Oxide (ITO) substitutes. Thin Solid Films. 2008;516:5822-8.
[103] Norris BJ, Anderson J, Wager JF, Keszler DA. Spin-coated zinc oxide transparent transistors. Journal of Physics D-Applied Physics. 2003;36:L105-L7.
[104] Li CS, Li YN, Wu YL, Ong BS, Loutfy RO. Performance improvement for solution-processed high-mobility ZnO thin-film transistors. Journal of Physics D-Applied Physics. 2008;41.
[105] Hua-Chi C, Chia-Fu C, Chien-Yie T. Transparent ZnO thin film transistor fabricated by sol-gel and chemical bath deposition combination method. Applied Physics Letters. 2007;90:12113-1-3.
[106] Ong BS, Li CS, Li YN, Wu YL, Loutfy R. Stable, solution-processed, high-mobility ZnO thin-film transistors. Journal of the American Chemical Society. 2007;129:2750-+.
[107] Gwinner MC, Vaynzof Y, Banger KK, Ho PKH, Friend RH, Sirringhaus H. Solution-processed zinc oxide as high-performance air-stable electron injector in organic ambipolar light-emitting field-effect transistors. Advanced Functional Materials. 2010;20:3457-65.
[108] Meulenkamp EA. Synthesis and growth of ZnO nanoparticles. Journal of Physical Chemistry B. 1998;102:5566-72.
[109] Ristic M, Music S, Ivanda M, Popovic S. Sol-gel synthesis and characterization of nanocrystalline ZnO powders. Journal of Alloys and Compounds. 2005;397:L1-L4.
[110] Natsume Y, Sakata H. Zinc oxide films prepared by sol-gel spin-coating. Thin Solid Films. 2000;372:30-6.
[111] Berber M, Bulto V, Kliss R, Hahn H. Transparent nanocrystalline ZnO films prepared by spin coating. Scripta Materialia. 2005;53:547-51.
[112] Ismail B, Abaab M, Rezig B. Structural and electrical properties of ZnO films prepared by screen printing technique. Thin Solid Films. 2001;383:92-4.
[113] Yu-Yun C, Jin-Cherng H, Wang PW, Yao-Wei P, Chih-Yuan W, Yung-Hsin L. Dependence of resistivity on structure and composition of AZO films fabricated by ion beam co-sputtering deposition. Appl Surf Sci. 2011;257:3446-50.
[114] Ederth J, Heszler P, Hultaker A, Niklasson GA, Granqvist CG. Indium tin oxide films made from nanoparticles: models for the optical and electrical properties. Thin Solid Films. 2003;445:199-206.
[115] Na JS, Peng Q, Scarel G, Parsons GN. Role of gas doping sequence in surface reactions and dopant incorporation during atomic layer deposition of Al-doped ZnO. Chemistry of Materials. 2009;21:5585-93.

[116] Wang X, Li R, Fan D. Control growth of catalyst-free high-quality ZnO nanowire arrays on transparent quartz glass substrate by chemical vapor deposition. Appl Surf Sci. 2011;257:2960-4.
[117] Weidenkaff A, Steinfeld A, Wokaun A, Auer PO, Eichler B, Reller A. Direct solar thermal dissociation of zinc oxide: Condensation and crystallisation of zinc in the presence of oxygen. Solar Energy. 1999;65:59-69.
[118] Janotti A, Van de Walle CG. Oxygen vacancies in ZnO. Applied Physics Letters. 2005;87.
[119] Bauerle D. Laser processing and chemistry. 3rd ed. New York: Springer; 2000.
[120] Incropera FP, Bergman TL, Lavine AS, DeWitt DP. Fundamentals of heat and mass transfer: Wiley; 2011.
[121] Schift H. Nanoimprint lithography: An old story in modern times? A review. Journal of Vacuum Science & Technology B: Microelectronics and Nanometer Structures. 2008;26:458.
[122] Guo LJ. Nanoimprint lithography: methods and material requirements. Advanced Materials. 2007;19:495–513.
[123] Gates BD, Xu Q, Stewart M, Ryan D, Willson CG, Whitesides GM. New approaches to nanofabrication: molding, printing, and other techniques. Chemical reviews. 2005;105:1171-96.
[124] Guo LJ. Recent progress in nanoimprint technology and its applications. Journal of Physics D: Applied Physics. 2004;37:R123.
[125] Fischer P, Chou S. 10 nm electron beam lithography and sub 50 nm overlay using a modified scanning electron microscope. Applied physics letters. 1993;62:2989-91.
[126] Li M, Chen L, Chou SY. Direct three-dimensional patterning using nanoimprint lithography. Applied physics letters. 2001;78:3322.
[127] Hulteen JC, Van Duyne RP. Nanosphere lithography: A materials general fabrication process for periodic particle array surfaces. Journal of Vacuum Science & Technology A: Vacuum, Surfaces, and Films. 1995;13:1553-8.
[128] Haynes CL, Van Duyne RP. Nanosphere lithography: a versatile nanofabrication tool for studies of size-dependent nanoparticle optics. The Journal of Physical Chemistry B. 2001;105:5599-611.
[129] Jensen TR, Malinsky MD, Haynes CL, Van Duyne RP. Nanosphere lithography: tunable localized surface plasmon resonance spectra of silver nanoparticles. The Journal of Physical Chemistry B. 2000;104:10549-56.
[130] Solak H, He D, Li W, Singh-Gasson S, Cerrina F, Sohn B, et al. Exposure of 38 nm period grating patterns with extreme ultraviolet interferometric lithography. Applied physics letters. 1999;75:2328.
[131] Solak H, David C, Gobrecht J, Golovkina V, Cerrina F, Kim S, et al. Sub-50 nm period patterns with EUV interference lithography. Microelectronic engineering. 2003;67:56-62.
[132] Park S, Schift H, Solak HH, Gobrecht J. Stamps for nanoimprint lithography by extreme ultraviolet interference lithography. Journal of Vacuum Science & Technology B: Microelectronics and Nanometer Structures. 2004;22:3246.
[133] Ross CB, Sun L, Crooks RM. Scanning probe lithography. 1. Scanning tunneling microscope induced lithography of self-assembled n-alkanethiol monolayer resists. Langmuir. 1993;9:632-6.

[134] Rolandi M, Quate CF, Dai H. A new scanning probe lithography scheme with a novel metal resist. Applied Physics Letters. 2001;79:731.
[135] Park I, Ko SH, Pan H, Grigoropoulos CP, Pisano AP, Fréchet JMJ, et al. Nanoscale patterning and electronics on flexible substrate by direct nanoimprinting of metallic nanoparticles. Advanced Materials. 2008;20:489–96.
[136] Khosrofian JM, Garetz BA. Measurement of a Gaussian laser beam diameter through the direct inversion of knife-edge data. Applied optics. 1983;22:3406-10.
[137] Suzaki Y, Tachibana A. Measurement of the μm sized radius of Gaussian laser beam using the scanning knife-edge. Applied optics. 1975;14:2809-10.
[138] Deubel M, Von Freymann G, Wegener M, Pereira S, Busch K, Soukoulis CM. Direct laser writing of three-dimensional photonic-crystal templates for telecommunications. Nature Materials. 2004;3:444-7.
[139] Huang MH, Mao S, Feick H, Yan H, Wu Y, Kind H, et al. Room-temperature ultraviolet nanowire nanolasers. science. 2001;292:1897.
[140] Kang HW, Yeo J, Hwang JO, Hong S, Lee P, Han SY, et al. Simple ZnO Nanowires Patterned Growth by Microcontact Printing for High Performance Field Emission Device. The Journal of Physical Chemistry C.
[141] Saito N, Haneda H, Sekiguchi T, Ohashi N, Sakaguchi I, Koumoto K. Low temperature fabrication of light emitting zinc oxide micropatterns using self assembled monolayers. Advanced Materials. 2002;14:418-21.
[142] Wang X, Summers CJ, Wang ZL. Large-scale hexagonal-patterned growth of aligned ZnO nanorods for nano-optoelectronics and nanosensor arrays. Nano letters. 2004;4:423-6.
[143] Fischer J, Wegener M. Three-dimensional direct laser writing inspired by stimulated-emission-depletion microscopy [Invited]. Optical Materials Express. 2011;1:614-24.
[144] Sakellari I, Kabouraki E, Gray D, Purlys V, Fotakis C, Pikulin A, et al. Diffusion-assisted high resolution direct femtosecond laser writing. ACS Nano. 2012.
[145] Scott TF, Kowalski BA, Sullivan AC, Bowman CN, McLeod RR. Two-color single-photon photoinitiation and photoinhibition for subdiffraction photolithography. Science. 2009;324:913-7.
[146] Li L, Gattass RR, Gershgoren E, Hwang H, Fourkas JT. Achieving λ/20 resolution by one-color Initiation and deactivation of polymerization. Science. 2009;324:910-3.
[147] Cao Y, Gan Z, Jia B, Evans RA, Gu M. High-photosensitive resin for super-resolution direct-laser-writing based on photoinhibited polymerization. Optics Express. 2011;19:19486-94.
[148] Tian ZR, Voigt JA, Liu J, McKenzie B, McDermott MJ, Rodriguez MA, et al. Complex and oriented ZnO nanostructures. Nat Mater. 2003;2:821-6.
[149] Kwon SJ, Park J-H, Park J-G. Patterned growth of ZnO nanorods by micromolding of sol-gel-derived seed layer. Applied Physics Letters. 2005;87:133112.
[150] Hsu JWP, Tian ZR, Simmons NC, Matzke CM, Voigt JA, Liu J. Directed spatial organization of zinc oxide nanorods. Nano Letters. 2005;5:83-6.
[151] Cole JJ, Wang X, Knuesel RJ, Jacobs HO. Patterned growth and transfer of ZnO micro and nanocrystals with size and location control. Advanced Materials. 2008;20:1474-8.

[152] Hu X, Masuda Y, Ohji T, Kato K. Micropatterning of ZnO nanoarrays by forced hydrolysis of anhydrous zinc acetate. Langmuir. 2008;24:7614-7.
[153] Fan HJ, Werner P, Zacharias M. Semiconductor nanowires: From self-organization to patterned growth. Small. 2006;2:700-17.
[154] Sounart TL, Liu J, Voigt JA, Hsu JWP, Spoerke ED, Tian Z, et al. Sequential nucleation and growth of complex nanostructured films. Advanced Functional Materials. 2006;16:335-44.
[155] Masuda Y, Kinoshita N, Sato F, Koumoto K. Site-selective deposition and morphology control of UV- and visible-light-emitting ZnO crystals. Crystal Growth & Design. 2005;6:75-8.
[156] Kang HW, Yeo J, Hwang JO, Hong S, Lee P, Han SY, et al. Simple ZnO nanowires patterned growth by microcontact printing for high performance field emission device. The Journal of Physical Chemistry C. 2011.
[157] Ko SH, Pan H, Grigoropoulos CP, Fréchet JMJ, Luscombe CK, Poulikakos D. Lithography-free high-resolution organic transistor arrays on polymer substrate by low energy selective laser ablation of inkjet-printed nanoparticle film. Applied Physics A: Materials Science & Processing. 2008;92:579-87.
[158] Zhang Q, Dandeneau CS, Zhou X, Cao G. ZnO nanostructures for dye-sensitized solar cells. Advanced Materials. 2009;21:4087-108.
[159] Cheng H-M, Chiu W-H, Lee C-H, Tsai S-Y, Hsieh W-F. Formation of branched ZnO nanowires from solvothermal method and dye-sensitized solar cells applications. The Journal of Physical Chemistry C. 2008;112:16359-64.
[160] O'regan B, Gratzel M. A low-cost, high-efficiency solar cell based on dye-sensitized colloidal TiO2 films. Nature. 1991;353:737-40.
[161] Ma T, Akiyama M, Abe E, Imai I. High-efficiency dye-sensitized solar cell based on a nitrogen-doped nanostructured titania electrode. Nano Letters. 2005;5:2543-7.
[162] Crossland EJW, Kamperman M, Nedelcu M, Ducati C, Wiesner U, Smilgies DM, et al. A bicontinuous double gyroid hybrid solar cell. Nano Letters. 2008;9:2807-12.
[163] Guldin S, Hüttner S, Kolle M, Welland ME, Müller-Buschbaum P, Friend RH, et al. Dye-sensitized solar cell based on a three-dimensional photonic crystal. Nano Letters. 2010;10:2303-9.
[164] Yang Z, Xu T, Ito Y, Welp U, Kwok WK. Enhanced electron transport in dye-sensitized solar cells using short ZnO nanotips on a rough metal anode. The Journal of Physical Chemistry C. 2009;113:20521-6.
[165] Nissfolk J, Fredin K, Hagfeldt A, Boschloo G. Recombination and transport processes in dye-sensitized solar cells investigated under working conditions. The Journal of Physical Chemistry B. 2006;110:17715-8.
[166] Grätzel M. Solar energy conversion by dye-sensitized photovoltaic cells. Inorganic Chemistry. 2005;44:6841-51.
[167] Grätzel M. Conversion of sunlight to electric power by nanocrystalline dye-sensitized solar cells. Journal of Photochemistry and Photobiology A: Chemistry. 2004;164:3-14.
[168] Jiang C, Sun X, Lo G, Kwong D, Wang J. Improved dye-sensitized solar cells with a ZnO-nanoflower photoanode. Applied physics letters. 2007;90:263501--3.
[169] Martinson ABF, Elam JW, Hupp JT, Pellin MJ. ZnO nanotube based dye-sensitized solar cells. Nano Letters. 2007;7:2183-7.

[170] Wang X, Ding Y, Summers CJ, Wang ZL. Large-scale synthesis of six-nanometer-wide ZnO nanobelts. The Journal of Physical Chemistry B. 2004;108:8773-7.
[171] Kar S, Dev A, Chaudhuri S. Simple solvothermal route to synthesize ZnO nanosheets, nanonails, and well-Aligned nanorod arrays. The Journal of Physical Chemistry B. 2006;110:17848-53.
[172] Fu M, Zhou J, Xiao Q, Li B, Zong R, Chen W, et al. ZnO nanosheets with ordered pore periodicity via colloidal crystal template assisted electrochemical deposition. Advanced Materials. 2006;18:1001-4.
[173] Suh DI, Lee SY, Kim TH, Chun JM, Suh EK, Yang OB, et al. The fabrication and characterization of dye-sensitized solar cells with a branched structure of ZnO nanowires. Chemical physics letters. 2007;442:348-53.
[174] Baxter JB, Aydil ES. Dye-sensitized solar cells based on semiconductor morphologies with ZnO nanowires. Solar energy materials and solar cells. 2006;90:607-22.
[175] Wang ZL, Kong X, Zuo J. Induced growth of asymmetric nanocantilever arrays on polar surfaces. Physical review letters. 2003;91:185502.
[176] Yan H, He R, Johnson J, Law M, Saykally RJ, Yang P. Dendritic nanowire ultraviolet laser array. Journal of the American Chemical Society. 2003;125:4728-9.
[177] Tarasov K, Raccurt O. A wet chemical preparation of transparent conducting thin films of Al-doped ZnO nanoparticles. Journal of Nanoparticle Research. 2011:1-8.
[178] Hsu CH, Chen DH. Synthesis and conductivity enhancement of Al-doped ZnO nanorod array thin films. Nanotechnology. 2010;21:285603.
[179] Chavillon B, Cario L, Renaud A, Tessier F, Chevire F, Boujtita M, et al. P-type nitrogen doped ZnO nanoparticles stable under ambient conditions. Journal of the American Chemical Society. 2012.
[180] Joseph M, Tabata H, Kawai T. p-type electrical conduction in ZnO thin films by Ga and N codoping. Japanese Journal of Applied Physics. 1999;38:L1205-L7.
[181] Chen HY, Su HC, Chen CH, Liu KL, Tsai CM, Yen SJ, et al. Indium-doped molybdenum oxide as a new p-type transparent conductive oxide. Journal of Materials Chemistry. 2011;21:5745-52.
[182] Sato H, Minami T, Takata S, Yamada T. Transparent conducting p-type NiO thin films prepared by magnetron sputtering. Thin Solid Films. 1993;236:27-31.
[183] Allenic A, Guo W, Chen Y, Katz MB, Zhao G, Che Y, et al. Amphoteric phosphorus doping for stable p-type ZnO. Advanced Materials. 2007;19:3333-7.
[184] Inomata Y, Fukui K, Shirasawa K. Surface texturing of large area multicrystalline silicon solar cells using reactive ion etching method. Solar Energy Materials and Solar Cells. 1997;48:237-42.
[185] Zhao J, Wang A, Green MA, Ferrazza F. 19.8% efficient “honeycomb” textured multicrystalline and 24.4% monocrystalline silicon solar cells. Applied Physics Letters. 1998;73:1991.
[186] Papet P, Nichiporuk O, Kaminski A, Rozier Y, Kraiem J, Lelievre JF, et al. Pyramidal texturing of silicon solar cell with TMAH chemical anisotropic etching. Solar Energy Materials and Solar Cells. 2006;90:2319-28.
[187] Atwater HA, Polman A. Plasmonics for improved photovoltaic devices. Nature materials. 2010;9:205-13.

[188] Hlaing H, Lu X, Hofmann T, Yager KG, Black CT, Ocko BM. Nanoimprint-induced molecular orientation in semiconducting polymer nanostructures. ACS Nano. 2011.
[189] Takanezawa K, Hirota K, Wei QS, Tajima K, Hashimoto K. Efficient charge collection with ZnO nanorod array in hybrid photovoltaic devices. The Journal of Physical Chemistry C. 2007;111:7218-23.
[190] Sauvage F, Di Fonzo F, Li Bassi A, Casari C, Russo V, Divitini G, et al. Hierarchical TiO2 photoanode for dye-sensitized solar cells. Nano Letters. 2010;10:2562-7.
[191] Shao F, Sun J, Gao L, Yang S, Luo J. Forest-like TiO2 hierarchical structures for efficient dye-sensitized solar cells. Journal of Materials Chemistry. 2012;22:6824-30.